THE HONG KONG POLYTECHNIC UNIVERSITY

DEPARTMENT OF APPLIED PHYSICS

DIELECTRIC PROPERTIES OF BARIUM STRONTIUM TITANATE (BST) THIN FILMS AND PHASE SHIFTERS BASED ON BST THIN FILMS

ZHOU XIAOYUAN

A THESIS SUBMITTED IN PARTIAL FULFILLMENT

OF THE REQUIREMENTS FOR THE DEGREE OF

DOCTOR OF PHILOSOPHY

NOVEMBER 2007

Certificate of Originality

I hereby declare that this thesis is my own work and that, to the best of my knowledge and belief, it reproduces no material previously published or written nor material which has been accepted for the award of any other degree or diploma, except where due acknowledgement has been made in the text.

_____ (Signed)

_____XiaoYuan Zhou_____ (Name of student)

ABSTRACT

In recent years, barium strontium titanate (abbreviated as BST) thin films have attracted extensive interest for both basic and applied research. Having a perovskite-type crystal structure, BST is known to exhibit a largely diversifiable ferroelectric/dielectric behavior that is influenced by a number of structural factors, such as lattice tetragonality, defects, ratio of barium to strontium, grain size and etc. Mainly due to the structural complexity, many questions on the structure-property relationship in BST thin films remain unanswered and there is also large room for further improving the material's properties.

In this work several key issues regarding BST thin films have been studied.

First, a clear correlation between lattice tetragonality and ferroelectric and dielectric behaviors has been established in BST thin films. The studied material was composed of $Ba_{0.7}Sr_{0.3}TiO_3$. Grown on single crystal substrates like $(LaAlO_3)_{0.3}(Sr_2AlTaO_6)_{0.7}$, $LaAlO_3$, $MgAl_2O_4$, the thin films were found to have distorted lattices (the cubic lattice of bulk BST with the same composition was regarded as "normal" and used as a reference). This distorted lattice structure leads to the enhanced in-plane dielectric and ferroelectric properties. With increasing film thickness from 20 to 300 nm, the in-plane lattice parameter (a) of BST grown on $LaAlO_3$ increased from 0.395 to 0.402 nm while the out-of-plane lattice parameter (c) remained almost unchanged, which led to an increased a/c ratio (tetragonality) changing from 0.998 to 1.012 and consequently resulted in a shift of Curie temperature from 306 to 360 K associated with an increase of the in-plane remnant

polarization and dielectric constant of the films. Similar effects were observed in BST grown on other substrates. The formation mechanism of the lattice distortion was studied in a model system consisting of a SrTiO$_3$ (film)/SiTiO$_3$ (single crystal substrate) homostructure. Among several processing parameters, deposition pressure and the kind of atmosphere were identified to be the critical factors that determined the lattice parameters of the perovskite oxides.

Secondly, a phenomenological model was developed to interpret the strain effect on the in-plane dielectric properties of BST thin films with different thickness. The theoretical modeling involved the grouping of strain into biaxial (2-dimensional) and hydrostatic (3-dimensional) components (which were obtained by analyzing the XRD results), the use of the Landau-Ginsburg-Devonshire formalism and mathematical calculations related to the elastic Gibbs free energy. The calculations confirmed that the ferroelectric transition temperature (Curie temperature) and dielectric constant decrease with the decreasing of film thickness.

Thirdly, a physical vapor deposition (PVD) process was developed for integrating perovskite-structured thin films on Si substrates. The heterostructure, SrTiO$_3$/Si, was first prepared by laser molecular-beam epitaxy using an ultra-thin Sr layer as the buffer layer. X-ray diffraction measurements indicated that SrTiO$_3$ was well crystallized and epitaxially aligned with Si. Cross-sectional observations in a transmission electron microscope together with X-ray reflectivity measurements revealed that the SrTiO$_3$/Si interface was sharp, smooth and fully crystallized. The thickness of the Sr-template was found to be a critical factor that influenced the quality of the SrTiO$_3$ layer and the interfacial structure. BST thin films were then deposited on the Si/SiO$_2$ substrates with the similar technology.

Fourthly, we have fabricated tunable microwave phase shifters on BST/LSAT substrates. High reliability, simple configuration and large phase shift per unit area are the major requirements in the design and fabrication. By carefully optimizing the processing, prototype devices with following specifications were obtained: work frequency = 9 GHz, phase shift up to 70°, figure-of-merit = 60°/dB, insertion loss (S_{21}) = -1.3 dB and return loss (S_{11}) = -14.3 dB.

LIST OF PUBLICATIONS

1. **_X. Y. Zhou_**, J. Miao, J. Y. Dai, G. H. K. Pang, H. L. W. Chan, C. L. Choy and Y. Wang, "Epitaxial growth of strontium titanate thin films on silicon by laser molecular beam epitaxy", *Applied Physics Letters*, 90, pp. 012902-2904, 2007.

2. **_X. Y. Zhou_**, D. Y. Wang, R. K. Zheng, H. Y. Tian, J. Q. Qi, H. L. W. Chan, C. L. Choy, and Y. Wang, "Thickness dependence of in-plane dielectric and ferroelectric properties of $Ba_{0.7}Sr_{0.3}TiO_3$ thin films epitaxially grown on $LaAlO_3$", *Applied Physics Letters*, 90, pp. 132902-2904, 2007.

3. **_X. Y. Zhou,_** T. Heindl, G. Pang, R. K. Zheng, H. L. W Chan, C. L. Choy and Y. Wang, "Microstructure and in-plane dielectric and ferroelectric properties of barium strontium titanate thin films on $MgAl_2O_4$ single crystal substrate", *Applied Physics Letters*, 89, pp232906-2908, 2006.

4. J. Miao, H. Y. Tian, **_X. Y. Zhou_**, K. H. Pang, and Y. Wang, "Microstructure and dielectric relaxor properties for $Ba_{0.5}Sr_{0.5}TiO_3/La_{0.67}Sr_{0.33}MnO_3$ heterostructure", *Journal of Applied Physics*, 101, pp.084101-4106, 2007.

5. **_X. Y. Zhou_**, D.Y. Wang, L. X. He, Y. Li, Y. Wang, H. L. W. Chan, and C. L. Choy, "Influence of temperature on the in-plane dielectric properties of barium strontium titanate thin film", *Integrated Ferroelectrics*, 77, pp. 157-164, 2006.

6. **X. Y. Zhou**, J. Hong, R. K. Zheng, H. L. W. Chan, C. L. Choy and Y. Wang, "Structure and dielectric properties of barium strontium titanate thin films grown on LAST substrates", *Ferroelectrics*, 357, pp.160-65, 2007.

7. J. Miao, Y. Wang, H. Y. Tian, **X. Y. Zhou**, H. L. W. Chan, C. L. Choy, L. X. Cao and B.R. Zhao, "A quantitative analysis on the interfacial effect in the $Ba_{0.5}Sr_{0.5}TiO_3/La_{0.67}Sr_{0.33}MnO_3$ heterostructure", *Journal of Physics D: Applied Physics,* 39, pp.2565–2570, 2006.

8. **X. Y. Zhou**, J. Miao, X. B. Lu, J. Y. Dai, Y. Wang, H. L. W. Chan and C. L. Choy, "Influence of processing conditions on the structure of strontium titanate thin films grown on Si by laser MBE", *Integrated Ferroelectric*, 86, pp.109-116, 2006.

9. Z. Ying, **X. Y. Zhou**, P. Yun, Y. Wang, H. L. W. Chan and C. L. Choy, "Comparison of structures and properties of BST thin films grown on LAO and MAO substrates", *Integrated Ferroelectrics*, 86, pp.103-108 2006.

10. D. Y. Wang, Y. Wang, **X. Y. Zhou**, H. L. W. Chan and C. L. Choy, "Enhanced in-plane ferroelectricity in $Ba_{0.7}Sr_{0.3}TiO_3$ thin films grown on MgO (001) single-crystal substrate", *Applied Physics Letters,* 86, pp. 1607-1611, 2005.

ACKNOWLEDGEMENTS

I would like to deeply thank my supervisors, Dr. Y. Wang and Prof. C. L Choy for their excellent supervision and invaluable advice throughout the whole study period. I would also like to thank Prof. H. L. W. Chan, Prof. F. G. Shin, Dr. J. Y. Dai, Dr. K. H. Wong and Dr. G. H. K. Pang for their assistance on my research and coursework studies.

I would like to thank Mr. M. N. Yeung of the Materials Research Centre for his assistance in the structure characterization.

I would like to give my thanks to colleagues and friends in AP for their help and assistance. They include Dr. D. Y. Wang, Ms. Y. L. Cheng, Dr. H. Y. Tian, Dr. J. Miao, Dr. R. K. Zheng, Dr. X. B. Lu, Dr. P. F. Lee, Mr. T. Heindl, Miss. P. Yun, Miss K. C. Chan, Mr. H. Ji, Miss X. J. Chen, Dr. G. Y. Wang, Mr. Y. M. Hu, Mr. W. Y. Li.

I gratefully acknowledge the Hong Kong Polytechnic University for affording me this opportunity to pursue PhD degree at the Department of Applied Physics.

Most of all, I would like to thank my parents, my brother and my sister for their love, understanding and support throughout the period of my undergraduate and postgraduate studies. I admire my parents greatly for their utmost effort towards achieving their level of success in both career and family.
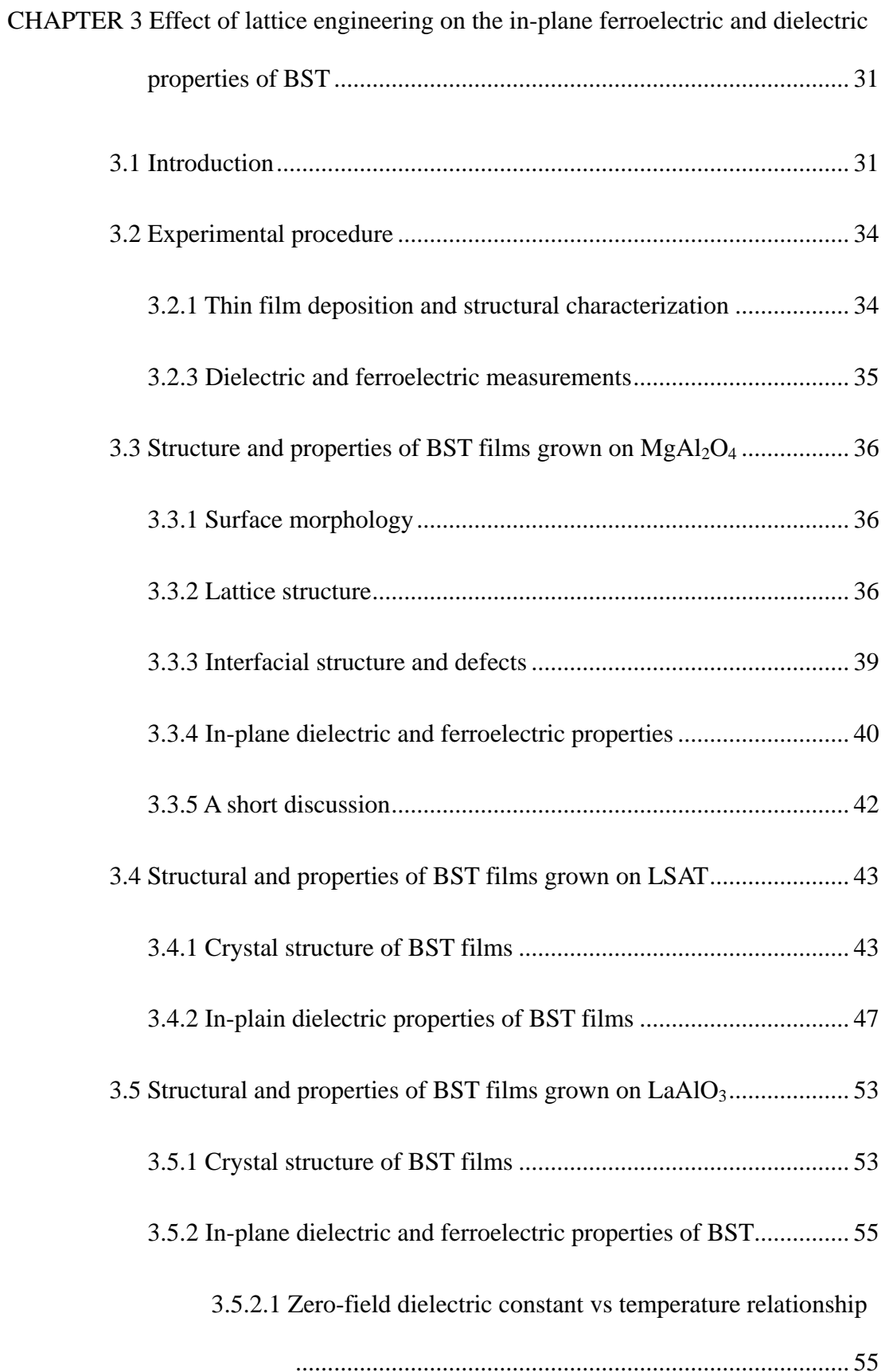
TABLE OF CONTENTS

LIST OF FIGURE CAPTIONS

LIST OF TABLE CAPTIONS

1.1 Introduction to ferroelectric materials

Ferroelectric materials are featured with spontaneous polarization that can be switched by external electric field. First observed in the Rechelle salt, ferroelectricity has been found to exist in over three thousand kinds of natural and man-made compounds. Many of the ferroelectric materials have found applications in the electrical and electronic industries. The study of ferroelectricity has been one of the most active areas in solid state physics and materials science in the last decades.

1.1.1 Origin of ferroelectricity

Ferroelectricity arises from asymmetry of lattice structure in crystals. Ferroelectric materials are a class of ionic, insulating materials whose low crystal symmetry permits them to have a stable net electric dipole in a certain direction. Ferroelectrics contain one or more polar axes along which the spontaneous polarization can be developed. Eleven of 32 possible crystal classes are centrosymmetric, which have no unique polar axis and can not exhibit ferroelectricity [J. F. Nye, 1957]. The remaining 21 crystal classes show a pyroelectric effect and exhibit a finite and permanent value of polarization (spontaneous polarization) in the absence of an applied electric field or stress. The ferroelectrics are those the direction of spontaneous polarization can be changed by an applied electric field.

The ability of ferroelectrics to change their atomic structure under the application of an electric field gives rise to extremely high values of permittivity, and hence dielectric constant. This is one reason ferroelectric materials have attracted much interest in their promising potential for a series of technological application [D. Roy, 1993]. For example, the high dielectric constant of perovskite materials in the paraelectric phase can be used to make high dielectric dynamic Random Access Memory (DRAM) cell. Many ferroelectric materials also possess good piezoelectric or pyroelectric properties. Based on their properties, ferroelectric materials find applications in many different areas as seen in Table 1.1. The pyroelectric effect in these materials can be used for uncooled infrared radiation detection. Primarily, the properties of switchable non-zero spontaneous polarization find application in Ferroelectric Random Access Memories (FeRAMs). The two stable states in the hysteresis loop correspond to the two binary states "0" and "1".

Table 1.1   Properties and applications of ferroelectric materials.

Properties	Applications
High permittivity	DRAM storage, capacitors, Frequency and phase agile microwave circuits
Piezoelectricity	Actuators and sensors
Polarizability	Non-volatile ferroelectric memory
Pyroelectricity	Infrared sensors
Electro-optical property	Thermal infrared switch

1.1.2 Perovskite-structured ferroelectric oxides

Ferroelectric perovskite oxides are a special family of functional materials. The composition of such oxides is generally written as ABO_3, where both A and B are metallic elements. Typical materials of this family include $BaTiO_3$, $PbTiO_3$, $Pb(Mg_{1/3}Nb_{2/3})O_3$ and etc. Many of such materials in this family have excellent dielectric, piezoelectric and optical-electric properties and thus are used in a large variety of electronic devices. In addition, with minor compositional or structural changes, the perovskite oxides may exhibit very different behaviors, making them very attractive for the basic research.

The most important common feature of ferroelectric perovskite oxides is that they possess a metal-oxygen octahedron in the unit cell which is believed to be the origin of the ferroelectricity in these materials. Figure 1.1 shows the unit cells of $BaTiO_3$ in paraelectric and ferroelectric states. Below Curie temperature, a relative displacement of cations with respect to anions occurs [R. E. Cohen, 1992]. As a result, a net-dipole moment in a unit cell forms due to the offset between the mass center of cations and that of anions. "Freezing" of the soft-mode induced by the long range Coulomb forces has been recognized as the microscopic mechanism for the occurrence of the ferroelectricity [R. Blinc, 1974].

(a)   (b)
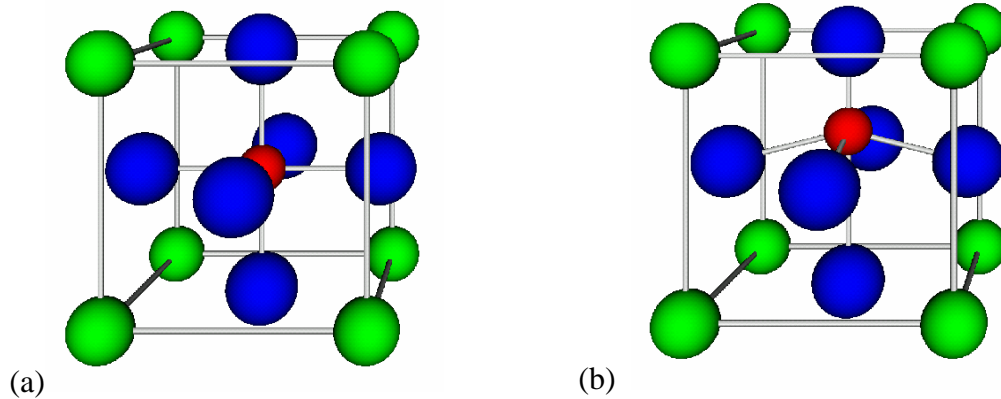
Fig. 1.1   Schematic unit cell of BaTiO$_3$ in (a) paraelectric and (b) ferroelectric

states.

In a simplified physical picture, ferroelectricity in perovskite oxides is directly

correlated with the tetragonality of the crystal lattice [R. E. Cohen and H. Krakauer,

1990]. The tetragonality is defined as the ratio of the lattice parameter along the

direction of applied electric field over the lattice parameter along the direction

perpendicular to the applied electric field. Doping and composition adjustment are

effective ways to change the tetragonality of bulk perovskite oxides [N. Sai, 2000; N.

W. Schubring, 1992]. For thin films, however, substrate effect and size effect also

have significant influence on the tetragonality. [V. Nagarajan, 2000; J. H. Chen, 2002;

Woo Young Park, 2003].

1.1.3 Size effect in ferroelectric oxides

In general, properties of solids vary with size and dimensionality because the

relative contribution to the total energy from the surface with respect to that from the

volume is a function of size and dimensionality [K. Binder, 1987; K. Ishikawa, 1995;

F. S. Yen, 1995]. This is especially true for ferroelectrics since ferroelectricity is a

collective phenomenon associated with a spontaneous macroscopic polarization

resulting from the alignment of localized dipoles within a correlation volume [R. Kretschmer, 1979; J. C. Slater, 1950]. In this picture, the long-range Coulomb force between dipoles plays an important role in the ferroelectric instability [J. C. Slater, 1950]. The long-range collective nature of the interaction yields an energy item inversely proportional to the spatial size ($1/\gamma$), leaving that the summation of the energy over volume itself is scale-dependent, i.e. diverging with respect to the volume. Size effect in ferroelectrics therefore refers to the relationship between the size as well as dimensionality of the samples and its physical properties, such as paraelectric-ferroelectric phase transition temperature (Tc), spontaneous polarization (Ps), and dielectric constant (ε) [I. P. Batra, 1973; D. R. Tilley, 1984]. Understanding size effect from a fundamental perspective is of particular importance for the research on nanoscale ferroelectrics, because the properties change drastically as the size of the ferroelectrics approaches the nanometer level and would limit the minimum useful thickness of these materials.

It is noted that size effect arises from both intrinsic and extrinsic mechanism. An intrinsic mechanism accounts for the variations of the properties of homogenous single-domain ferroelectrics [S. Chattopadhyay, 1995; C. A. Randall, 1998], while an extrinsic mechanism arises from a few other size-related factors, involving the contributions from domain-walls, the variation in the internal elastic field and, the defect configurations [A. Handi,1984; R. Backnn, 1988; S. L. Delprat, 2007].

In general, the intrinsic effect of small size depresses the ferroelectricity. The characteristics include shifting the phase transition to lower temperature, reducing the spontaneous polarization, increasing the coercive field, broadening the dielectric anomaly around the phase transition, and reducing the dielectric permittivity. There

exists a specific size below which no paraelectric-ferroelectric phase transition occurs. A depolarization mechanism is responsible for the size-dependent properties of ferroelectrics. As we know, spontaneous polarization generates an electric field antiparallel to the spontaneous polarization inside the crystal. This field is called a depolarization field by which the spontaneous polarization is counteracted. The depolarization field is compensated by the formation of domains, surface charge, or a polarization gradient in the crystals in order to reduce the electrical energy. It seems that a polarization "depletion" layer occurs in the region close to the surface of the crystal. The polarization "depletion" layer could greatly suppress the ferroelectricity as the crystal is sufficiently small.

Another important nanoscale phenomenon that has recently attracted extensive attention is related to the influence of extrinsic factors on the ferroelectric behaviors and dielectric properties of the nano-scale perovskite oxides. To be specific, the extrinsic factors in an ultra-thin film grown on a substrate mainly include state of the interface between the film and the substrate, grain size, dopant and orientation of the film. Mainly because of the very large specific area of the nano-grains and very small domain size (if domains still exist), the perovskite oxide-based ultra-thin films may exhibit significantly different properties if the above mentioned factors are changed. For example, epitaxial strontium titanate film was observed to show room-temperature ferroelectricity which was induced by a manipulated interface state. Some other interesting results regarding the modification of nanoscale perovskite oxides (lead zirconate titanate, barium titanate, etc) have also been recently reported in literature. [K. J. Choi, 2004; J.H. Haeni, 2004; M. W. Chu, 2004; B. Riehl, 2003] These results suggest the structure-property relationship in these

nanoscale materials could be, to some extent, different from the structure-property relationship that has been well established in bulk ferroelectric materials.

However, a complete picture is not yet available mainly due to the lack of systematic work on the fabrication and characterization of nanoscale perovskite oxide.

1.2 Barium Strontium Titanate

Barium strontium titanate ($Ba_{1-x}Sr_xTiO_3$, abbreviated as BST) is a solid solution of barium titanate ($BaTiO_3$ or BTO) and strontium titanate ($SrTiO_3$ or STO) and it can be formed over the entire range of concentration x. While $BaTiO_3$ and $SrTiO_3$ are two simple-perovskite oxides, BST is usually called a complex perovskite oxide because both Ba^{2+} and Sr^{2+} occupy the A-site in the ABO_3-crystal structure [H. Landolt, 1981]. The lattice constant of these perovskites is always close to 4 Å due to the rigidity of the oxygen octahedral network and the well defined oxygen ionic radius of 1.35Å.

1.2.1 Structure-property relationship in bulk BST

The structure-property relationship in bulk BST has been well established in the literature. The ferroelectric transition temperature is approximately a linear function of Ba to Sr ratio, as shown in Figure 1.2. Upon adding Sr into BTO, the paraelectric to ferroelectric transition temperature Tc keep decreasing linearly and about 30% of STO, the ferroelectric transition takes place near room temperature.
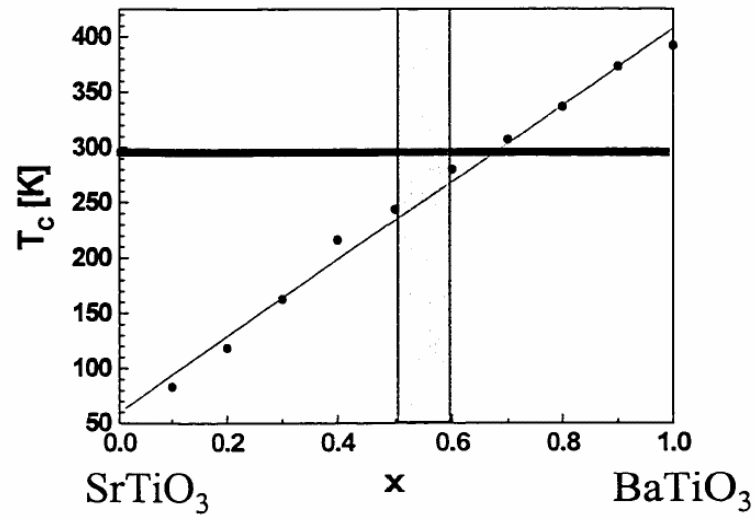
Fig. 1.2   Ferroelectric transition temperature as a function of Ba/Sr ratio in bulk

BST [[H. Landolt, 1981].

The crystal structure of BST as a function of Ba/Sr ratio is shown in Figure 1.3. At the Ba-rich end, the material has a tetragonal unit cell and at the Sr-rich end, the material has a cubic unit cell. The boundary between tetragonal and cubic symmetry is around x = 0.30, which is consistent with the dielectric test results.
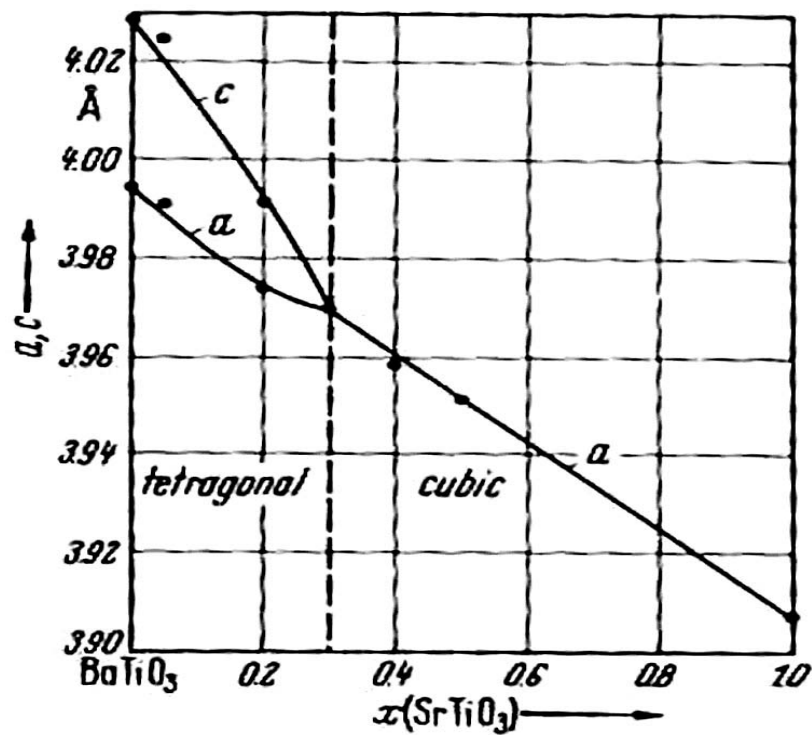
Fig. 1.3　Crystal structure of BST ceramics as a function of Ba/Sr ratio [H. Landolt, 1981].

　　A more detailed temperature dependence of dielectric constant of BST is given in Figure 1.4. The temperature for maximum dielectric constant (Curie temperature) changes with x. The dielectric constant of BST ceramics is generally large. For BST with x = 0.60, for example, the maximum dielectric constant is ~15,000. The very large dielectric constant makes BST a very useful material for ceramic capacitors.
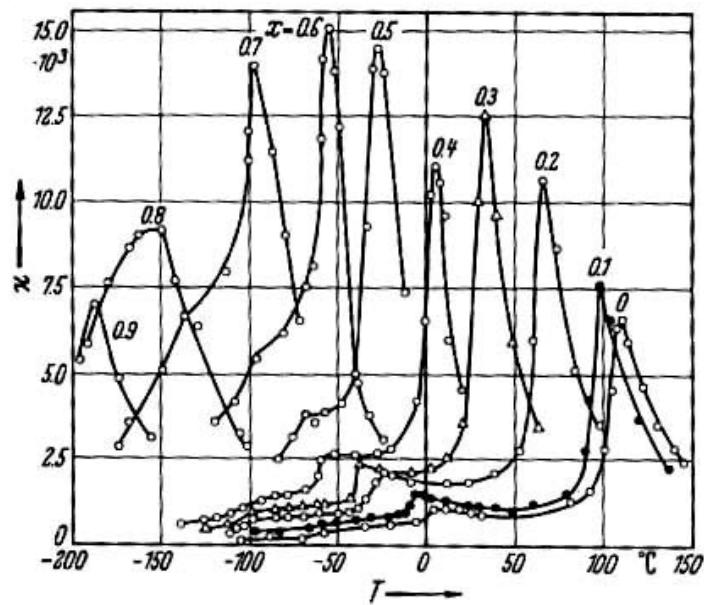
Fig. 1.4   Temperature dependence of dielectric constant for BST ceramics with

different Ba/Sr ratio [H. Landolt, 1981].

1.2.2 Study of BST thin films

The study of BST thin films is mainly motivated by the potential applications

for producing a number of microelectronic components and devices, including

infrared sensors and thermal imagers, dynamic random access memory and tunable

microwave devices [C. Buchal, 1998; M. F. Hsu, 2006; J. Kim, 2006]. Different

properties are required in these devices. For use in infrared sensors and thermal

images, the BST thin film is required to exhibit a good pyroelectric property.

Therefore it must work in ferroelectric state. For use in dynamic access memory, the

BST thin film is required to possess a large dielectric constant. For use in tunable

microwave devices, the BST thin film is required to exhibit a tunable dielectric

constant and small loss tangent; thus it usually works in paraelectric state. Quite

obviously, tailorable ferroelectric and dielectric properties of BST is the key reason

that makes BST useful for so many different applications. Some of the literature results are summarized as below.

1.2.2.1 Deposition of BST thin films

Several thin film deposition techniques have been adopted in the fabrication of $Ba_{1-x}Sr_xTiO_3$ thin films and the properties of the films are strongly dependent on the processing techniques as given in the literature [T. Y. Tseng, 1999]. Typical techniques include the sol-gel method, radio frequency magnetron sputtering, pulsed laser ablation deposition (PLD), chemical vapor deposition (CVD) etc. In the literature, the PLD method is the most popular method for basic research due to its high deposition rate and good control of material composition.

1.2.2.2 Overview of structure-property relationship in BST thin films

Compared with that in bulk BST, the structure-property relationship in thin films is much more complicated. Based on the literature, we may roughly outline it as followings:

(1) The ratio of Ba/Sr is still a dominant factor that controls the ferroelectric transitions in BST thin films. Both the ceramics and thin films share a same trend; i.e., the higher the ratio of Ba/Sr, the higher the transition temperature. However, the dependence of transition temperature on Ba/Sr ratio is quantitatively inconsistent for BST ceramics and thin films. As shown in Figure 1.5, the lattice constants of BST thin films are not the same as the ones of BST ceramics with the same compositions. As shown in Figure 1.6, the ferroelectric transition temperatures of BST thin films with large Ba contents are higher than that of BST ceramics with the same

compositions.
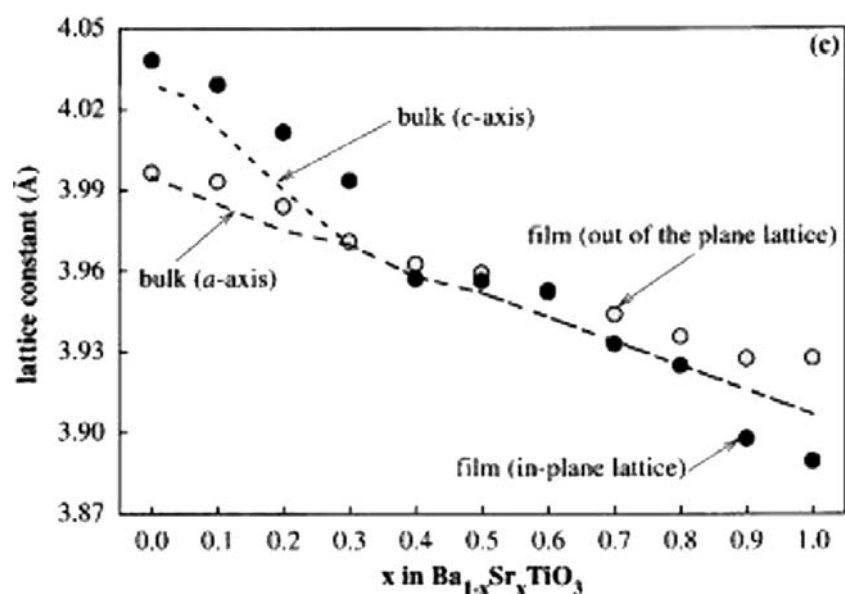
Fig. 1.5   A comparison of the lattice constant vs Ba/Sr ratio relationship in bulk

and thin film of BST [H. Landolt, 1981; H. J. Gao, 1999].
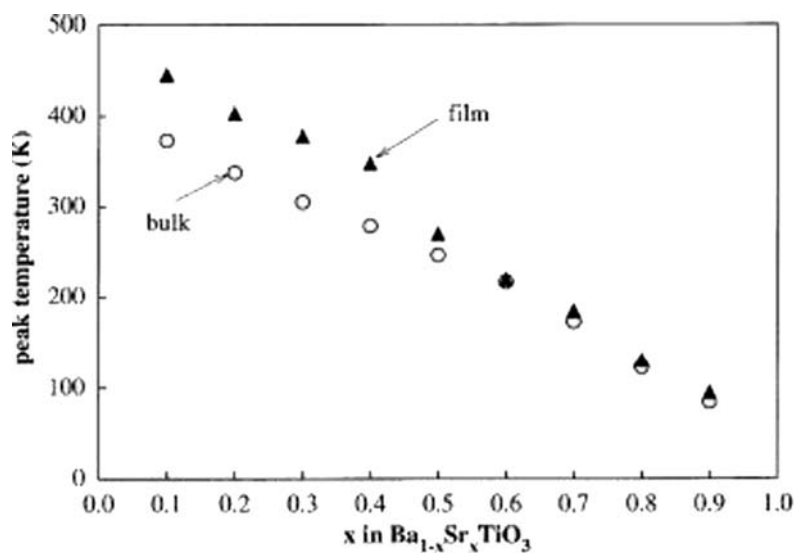
Fig. 1.6   A comparison of ferroelectric transition temperature vs Ba/Sr ratio

relationship in bulk and thin film of BST [H. Landolt, 1981; H. J. Gao,

1999].

(2) Substrate has significant influence on structure and properties of BST thin films. Grown on the surface of the substrate, the crystal structure and microstructure of BST thin film is influenced by the crystal structure and surface morphology of the substrate. Moreover, in the electrical test, the thin film is mechanically clamped by the substrate and thus cannot respond freely to external stimulations.

(3) Defects have important influences on the properties of BST thin films. In most cases, BST thin films are grown in an oxygen-deficient environment. Consequently the as-deposited BST thin films usually contain a large concentration of oxygen vacancies. Post-annealing can reduce the concentration but cannot fully remove them. Other defects, such as dislocations and grain boundaries have also important influences on thin film properties.

1.2.3 BST thin films for tunable microwave devices

1.2.3.1 Dielectric tunability and tunable microwave devices

Ferroelectric materials are characterized with a nonlinear dielectric response. Figure 1.7 shows a typical dependence of dielectric constant (ε) on electric field. Note that dielectric test is often conducted by using an ac signal and the electrical field in the figure actually refers to the field of a DC bias that is applied across the sample under test. It is found that, for a ferroelectric oxide tested or working in its paraelectric state, the ε-E relationship follows the Johnson Equation [C. Zhou, 1997]]:

$$\varepsilon_r(T,E) = \frac{\varepsilon_r(T,0)}{\{1 + [\varepsilon_0\varepsilon_r(T,0)]^3 B(T)E^2\}^{\frac{1}{3}}} \quad (1.1)$$

where ε_r(T, E) and ε_r(T, 0) are the dielectric constant under the electrical field E and zero field, respectively, and B(T) is a phenomenological constant, which provides information on the degree of enharmonic contributions of the polarization to the Helmhotz free energy [K. M. Johnson, 1962].

(a)   (b)
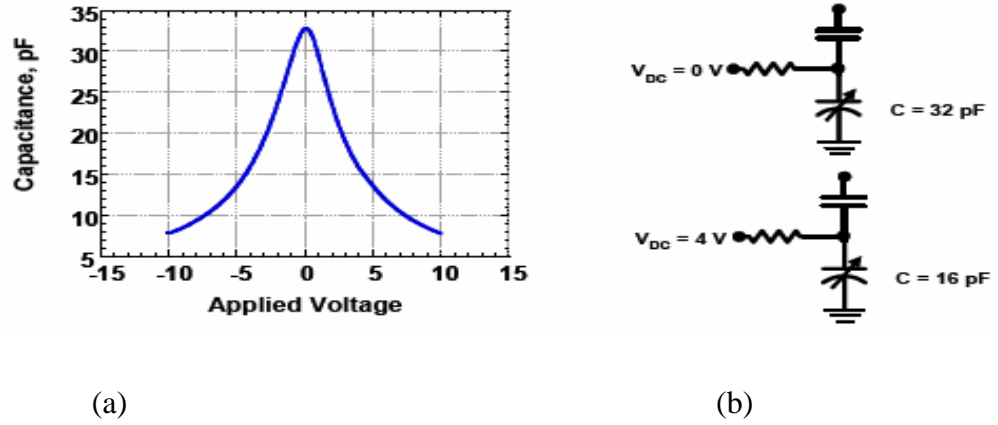
Fig. 1.7   Schematic diagram showing (a) Tunable dielectric behavior of ferroelectric material. (b) Capacitance of a ferroelectric oxide-based capacitor changes as external electric field changes.

The feature of tunable dielectric constant of ferroelectric materials is useful for producing tunable microwave devices. In general, the ferroelectric materials are used as dielectric layers in capacitors. The capacitance of the capacitor is proportional to the dielectric constant of the dielectric material; therefore it can be conveniently changed by changing the voltage applied on the capacitor. Once the capacitance is changed, the impedance and phase of the circuit involving the capacitor is also changed.

The field dependence of the dielectric constant in ferroelectrics was discovered in the 1950's. Since the 1960's, there has been effort to develop tunable components using the nonlinear dielectric behavior of ferroelectric materials. BST is a good candidate for such applications mainly because: (1). Dielectric and ferroelectric properties of BST can be easily modified by adjusting the ratio of Ba/Sr; and (2). BST is relatively "soft", especially when it works around the ferroelectric transition temperature. The mechanism for the dielectric behaviors has been investigated. The presence of the soft mode is not only the underlying mechanism for the ferroelectric phase transition itself, but also the cause of the large non-linear dielectric response of BST [F. Jona, 1962; M. E. Lines, 1977]. As the mode soften, it becomes easier and easier for a small electric field to separate the Ti and O sublattices, leading to a divergence of the small signal dielectric constant. Furthermore, applying a larger DC electric field changes the dynamics of the soft mode or stiffens its frequency, and thereby decreases the dielectric constant by changing the shape of the potential well in which the soft mode vibrates. In general, the effects of the applied field are to decrease the overall $\varepsilon/\varepsilon_0$ and to cause the temperature of maximum $\varepsilon/\varepsilon_0$ to slightly increase. This picture is helpful for understanding the tunable dielectric behavior in BST. Nevertheless, the use of BST ceramics in tunable components was rather limited mainly because very large DC voltage is required in order to drive the ceramics to exhibit a good tunability.

1.2.3.2 BST thin film-based microwave devices

For applications in tunable devices, BST thin films are more attractive than bulk materials due to the lower operation voltage, smaller size and higher level of

integration [W. Chang, 1999; T. J. Zhang, 2007]. In the last decade, there has been extensive research on the development of BST thin film-based microwave devices, including phase shifters, voltage control oscillators (VCO), tunable filters, reconfigurable antennas, and RF MEMS switches [H. Yoon,, 2004; S. S. Gevorgian, 1996; R. Igreji; K. B. Kim, 2007]. Among these devices, microwave phase shifter is most typical and widely studied.

Microwave phase shifter is one of the essential components for microwave communication systems. Typical applications of phase shifters include the phased array antenna, global positioning system (GPS), car collision avoidance radar and so on. Figure 1.8 schematically shows how a phase shifter works in a smart antenna. Phased array antennas have many advantages over traditional rotating reflector antennas because they are electronically steerable and thus are faster, more accurate, more reliable, and able to track multiple targets at one time. It is generally planar in shape and made up of thousands of closely spaced, individual radiators whose composite beam can be shaped and specially directed in microseconds. This is accomplished electronically by radio frequency (RF) phase shifters associated with each individual radiating element. Each phase shifter produces a certain amount of phase shift comparable to its neighboring radiators, thus the wave front of each radiated beam changes continuously through a series of neighboring phase shifters. Therefore, the composite RF beam can be directed by controlling the phase shifter of each individual radiator.
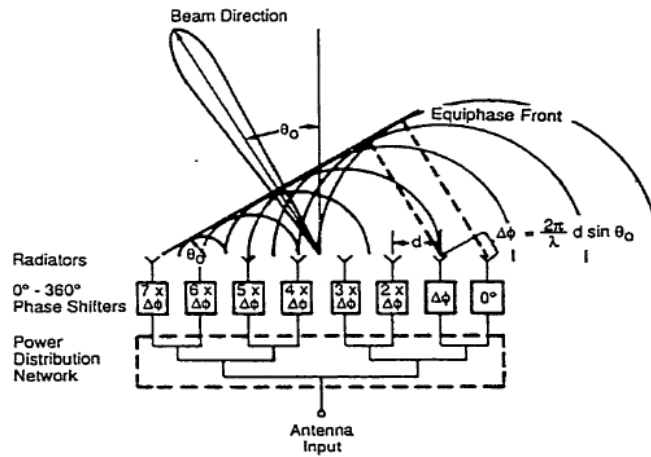
Fig. 1.8   Schematic of the RF beam-steering by using an array of phase shifter [S. S. Gevorgian, 1996].

Development of electrically tunable phase shifters being deployed today employ is either ferrite or PIN diode [C. T. Black, 1999; K. Natori, 1998].   Ferrite phase shifters can handle high power, typically hundreds of kilowatts to megawatts region, and have very low losses. However, they are usually large and heavy, also their operational speed is relatively low, and most importantly they are complex and very costly. On the contrary, PIN diodes are much cheaper and faster, but with a high insertion loss and very low power handling capacity, its use has also been limited. In order to make these devices practical for many other military and commercial uses, such as airport traffic control and automobile auto-drive systems, better materials for phase shifters may provide a cost breakthrough for the phased array antenna designer while maintaining low insertion losses, low drive power and high power handling capacity [G. Subramanyam, 2005; C. H. Mueller, 2000; L. Sengupta, 1999]. Ferroelectric components are simple in nature and allow cost effective integration in complex microwave systems. Among several possible candidate ferroelectric materials, BST has emerged as the most promising one because it is easy to control

and fabricate and do not have toxic component together with the large electric field dependent permittivity, low loss tangent, high dielectric constant, high power handling capability [R. Romanofsky, 2000; Y. I. Yuzyuk, 2007], negligible DC power consumption, potential low cost, high integration capability, requiring low tuning voltage and high speed. Additionally, BST thin-films can withstand high operating voltages as it has a high breakdown field (>2MV/cm).

1.2.3.3 Key parameters for tunable microwave devices

Tunability and loss tangent are the most important basic parameters characterizing ferroelectrics for applications in tunable microwave devices. The tunability of a particular material means how much the dielectric constant changes upon a certain applied field. It is conventionally defined as $[\varDelta\varepsilon/\varepsilon = (\varepsilon_{max}-\varepsilon_{min})/\varepsilon_{max}]$. The degree of phase shift is directly related to the tunability, therefore higher tunability is desired. The intrinsic loss tangent serves to dissipate or absorb the incident microwave energy and therefore is desired to be in the range of 0.01 or less. A low loss tangent decreases the phase shifter insertion loss and hence increases the phase shifting per decibel of loss (Figure-of-Merit). Also, the insertion loss is inversely related to the tunability so that the larger the tunability, the smaller the insertion loss. To achieve optimum electronic properties, the tunability should range from at least 10% to as high as 50%, depending upon the dielectric constant and the loss tangent. Precise control of composition and microstructure is critical for the production of BST thin films with large field dependence permittivity, low losses, and high electrical breakdown fields that are required for successful integration of BST into tunable high frequency microwave devices.

1.3 Scope of the present study

As discussed above, BST has been extensively investigated but there are still a number of questions that remain unanswered. The primary objective for this dissertation is to study the influence of interface between thin film and substrate and, stress and strain on the ferroelectric behaviors and microwave dielectric properties of nanoscale barium strontium titanate (BST) films grown on single crystal substrates; Identify the ideal structures of BST that give the best microwave properties and optimize the processing conditions for making such structures; integrate perovskite oxide (STO) on Si substrates; make BST film-based prototype microwave devices.

Following the introduction given in this Chapter, the thesis involves the next five chapters:

Chapter 2 gives a short introduction to three key techniques that have been employed in the study, including laser molecular beam epitaxy (for thin film deposition), x-ray diffraction (for determination of crystal structure of BST) and microwave measurements.

Chapter 3 focuses on the influence of lattice tetragonality on the in-plane dielectric and ferroelectric properties of epitaxial $Ba_{0.7}Sr_{0.3}TiO_3$ (BST 70/30) thin films grown on single crystal substrates. BST grown on three types of substrates - $MgAl_2O_4$, LSAT, $LaAlO_3$ were characterized and compared. The influence of processing factors in the thin film deposition on the lattice tetragonality of BST was also investigated.

Chapter 4 is related to theoretical work that aims to give a semi-quantitative explanation to the phenomenon reported in Chapter 3.

Chapter 5 focuses on the integration of perovskite thin films (STO) on Si wafer through laser molecular beam epitaxy. Such STO/Si heterostructure is useful for microelectronic devices including microwave phase shifters.

Chapter 6 describes our experimental work on microwave characterization of BST thin films and the development of BST-based microwave phase shifter.

Conclusions and suggestion for future work are given in Chapter 7.

1.4 Statement of original contribution

To the best of my knowledge, the present work has made the following original contributions:

Strain effect was investigated by exploring the correlation between lattice distortion and in-plane ferroelectric polarization, dielectric constant and tunability.

A phenomenological thermodynamic theory using a modified Devonshire form of elastic Gibbs free energy was employed to investigate the strain effect on the in-plane electrical properties of BST thin films. The simulated results are consistent with our experimental observation.

Perovskite STO thin films which are well crystallized and epitaxially aligned on Si substrates were successfully grown by laser MBE. This processing technique has been transferred to grow BST on SiO_2/Si substrates.

Ferroelectric phase shifter based on low pass filters has been designed. The evaluation of device's performance was conducted theoretically and experimentally. The figure-of-merit was found to be around 60°/dB at 9 GHz.

CHAPTER 2

Techniques for deposition and characterization

of barium strontium titanate thin films

2.1 Introduction

The study of barium strontium titanate thin films involves a number of advanced techniques and facilities for the deposition and characterization of thin films. They include:

(1) Thin film deposition and electrode patterning: pulsed laser deposition (PLD), laser molecular beam epitaxy (laser-MBE), magnetron sputtering, spin coating and photolithography (for electrode patterning).

(2) Structural characterization of thin films: x-ray diffraction (XRD), x-ray reflectivity (XRR), atomic force microscopy (AFM), scanning electron microscopy (SEM), transmission electron microscopy (TEM).

(3) Electrical characterization: dielectric tests by impedance analyzer (frequency f < 100 MHz) and network analyzer (f > 100 MHz), ferroelectric tester and leakage current measurement.

In this chapter, a short introduction is given to three typical techniques and equipment that were particularly useful in our research. They are: PLD, XRD and network analyzer.

2.2 Deposition of BST Thin Films

In the literature, different techniques have been employed in the deposition of BST thin films. They include physical vapor deposition method (PVD), such as magnetron sputtering [Park, 2003] and pulsed laser deposition (PLD) technique [Chen, 2001], and soft chemical method, such as sol-gel [Adikary, 2003] and metalorganic vapor deposition (MOCVD) method. Among these techniques, PLD is extensively used.

In this study, BST thin films are required to be chemically stoichiometric and epitaxially aligned on substrates. In order to achieve good control of thin film composition and quality, we chose pulsed laser deposition and laser molecular beam epitaxy (laser MBE) as the major techniques for the deposition of thin films. Basically they are similar in terms of growth mechanism of thin films and process control; therefore we only give a short introduction to the PLD method in this chapter.

2.2.1 Pulsed laser deposition technique

Pulsed laser deposition (PLD) is a physical vapor deposition technique for producing thin films and nanostructures by utilizing a physical process called laser ablation. It is applicable to most materials, in particular to compounds that are difficult or impossible to produce in thin-film form by other techniques. A PLD system consists three parts: vacuum system, chamber and laser system.

The principle of PLD is based on the interaction of laser and materials. In the deposition, a high power pulsed laser beam is focused inside a vacuum chamber to

strike a target of the desired composition. Material is then vaporized from the target and deposited as a thin film on a substrate. The physical phenomena are indeed quite complex – When the laser pulse is absorbed by the target, energy is first converted to electronic excitation and then into thermal, chemical and mechanical energy resulting in evaporation, ablation, plasma formation and even exfoliation. The ejected species expand into the surrounding vacuum in the form of a plume containing many energetic species including atoms, molecules, electrons, ions, clusters, particulates and molten globules, before depositing on the typically hot substrate. This process can occur in ultra high vacuum or in the presence of a background gas, such as oxygen which is commonly used when depositing oxides to fully oxygenate the deposited films. Figure 2.1 shows a schematic setup and process of PLD.
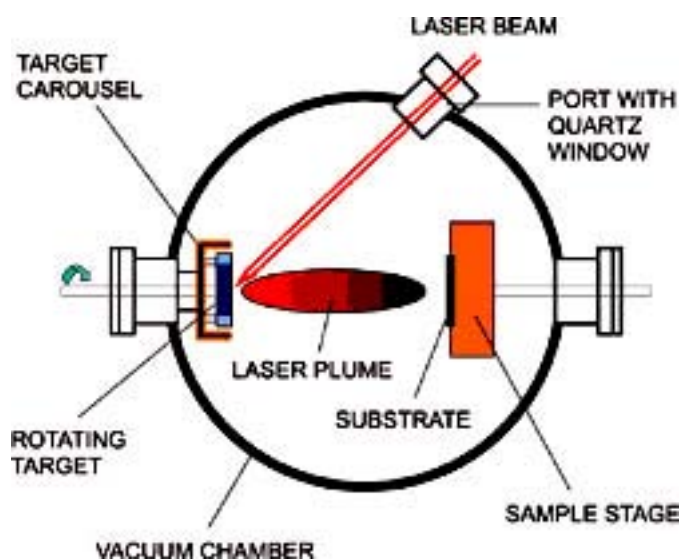
Fig. 2.1   Schematic setup (vacuum chamber) of pulsed laser ablation.

The PLD method is widely used in the study of thin films. The advantages of this method include: simplicity of use, relatively high deposition rate and high precision of composition control. The last point is based on the fact that, during the interaction of the laser and target, the heating rate of the target surface is so high (up

to 10^8 K/s) that it can lead to the congruent evaporation of the target irrespective of the evaporation point of the constituent elements or compounds of the target. Therefore the stoichiometry of the target can be retained in the deposited films. This feature is very useful when the composition of the material under investigation is very complex. Some shortcomings have also been identified. They include the splashing or the particulates deposition on the films and a poor uniformity of thin film over a large area. The latter problem limits the usefulness of PLD in producing large area uniform thin films, thus PLD has not been fully deployed in industry. Inserting a shadow mask between the substrate and the target can effectively block off the large particulates. Simultaneous rotation of the target and substrate can help to improve the uniformity.

2.2.2 PLD system and typical processing conditions

The pulsed laser deposition system in our laboratory consists of three parts: (1) A vacuum chamber which houses a target holder and a substrate stage, (2) Laser generator (Lambda Physik COMPex 205) and optical focusing system, and (3) Vacuum system which consists of a mechanical pump and a turbo molecular pump.

In our research, the deposition of BST thin films was usually conducted in our PLD system. Ceramic targets with desired compositions were prepared by conventional ceramic processing and the quality of the targets was examined by XRD, SEM and dielectric tests (the Curie temperature of BST ceramics is dependent on the ratio of Ba/Sr). The single crystal substrates were supplied by Heifei Kejing Materials Technology Co., Ltd. The typical processing conditions are summarized in Table 2.1.

Table 2.1 Typical processing conditions in the PLD deposition of BST thin films

Target-substrate distance	50 mm
Laser	A KrF excimer laser wavelength = 248 nm pulse duration = 25 ns energy = 250 mJ (energy density on the target surface = 2 - 3 J/cm^2)
Repetition rate of pulsed laser	5-10 Hz
Base vacuum	10^{-4} Pa
Ambient gas and pressure	Oxygen, 27 Pa
Substrate temperature ($^{\circ}$C)	750

In the research, laser MBE technique was also used for producing thin films. The principle of laser MBE is quite similar to that of PLD. Details of the processing conditions will be given in corresponding chapters.

2.3 X-ray Diffraction (XRD)

In our study, the technique of X-ray diffraction (XRD) was employed to characterize the crystalline structure of the BST thin films. In particular, the lattice parameters of BST thin films were determined by means of XRD.

2.3.1 Principle of XRD and measurement techniques

The application of x-ray diffraction in the measurement of material's crystal structure is based on Bragg's law. Figure 2.2 shows the basic geometry of XRD. A

beam of parallel X-rays impinges on the crystal surface at an angle θ and diffracted at an angle θ. The condition for constructive interference is that the path difference between the two rays is equal to an integral number n of wavelengths. That is:

$$n\lambda = 2\, d_{hkl} \sin\theta \qquad\qquad (2.1)$$

where d_{hkl} is the distance between the lattice planes ($h\, k\, l$) and λ is the wavelength of x-ray beam.
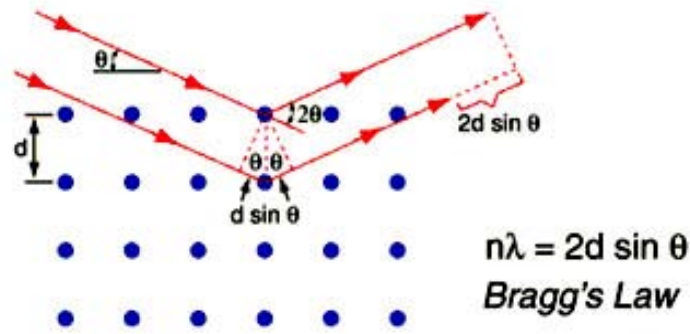
Fig. 2.2   Principle of x-ray diffraction for crystal structure characterization.

2.3.2 Characterization of BST thin films

2.3.2.1 X-ray diffractometer

The X-ray diffraction measurements on the BST thin films were carried out on a Bruker AXS D8 Discover X-ray diffractometer. The four-circle X-ray diffractometer is with a horizontal, high-resolution Ω-2θ goniometer. An open Eulerian cradle provides two additional axes of rotation ($-90° < \psi < 90°$, and $-360° < \phi < +360°$). The X-ray source is a long-fine-focus, ceramic X-ray tube with Cu anode. Normal operating power is 40 kV and 40 mA and Cu Kα_1 radiation with a wavelength $\lambda =$ 0.15406 nm is used. The sample stage supports monolithic specimens of a wide
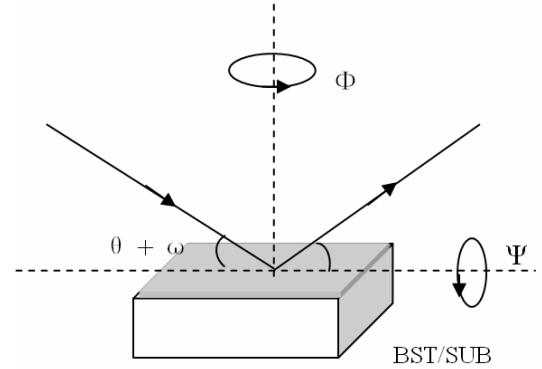
<div align="center">(a)   (b)</div>

variety of shapes and sizes.

Fig. 2.3   (a) Four-circle X-ray diffractometer (Bruker AXS D8 Advance).

(b) Geometrical relationship of the sample and x-ray.

2.3.2.2 Structural characterization

It is important to note that a full characterization of BST structure cannot be obtained by a single experiment. Instead, a series of measurements, including θ-2θ scan, rocking curve, ϕ-scan and ψ-scan, are needed.

As to be demonstrated later, BST thin films epitaxially grown on single crystal substrates often possess a tetragonal structure. To measure the lattice parameters of BST was an important task in the research. The out-of-plane lattice parameter (c) can be easily obtained by conducting conventional θ-2θ scan to measure the planar distances d_{00l} (typically d_{002}). To measure the in-plane lattice parameter (a), the sample must be tilted such that the θ-2θ scan can be conducted with respect to the (101) plane of BST. From the XRD patterns, the lattice spacing d_{202} can be obtained. Then the out-of-plane lattice parameter c ($=2d_{002}$) and the in-plane lattice parameter a

$(=2/\sqrt{d_{202}^{-2}-d_{002}^{-2}}\,)$ are obtained because, in a tetragonal lattice, the lattice parameters

and planar spacing satisfy the following equation:

$$d_{hkl} = \frac{a}{\sqrt{h^2+k^2}} + \frac{c}{\sqrt{l^2}} \tag{2.2}$$

where d_{hkl} is the distance between the lattice planes ($h\,k\,l$).

2.4 Microwave measurement

Microwave testing of the device was performed by a network analyzer 8720ES (Agilent, USA) with a standard probe station Microtech RF-1 (Cascade, USA) and a pair of air coplanar ground-signal-ground (GSG) microprobes (Cascade, USA). For adding DC bias to the microwave measurement, an external DC power supply Agilent 6629A was used. The photographs of the GSG microprobe and experimental setup are shown in Figure 2.4. The tips of the microprobe are made of beryllium copper (BeCu). This type of tips is suitable for the use with gold pad as the contact substrate.
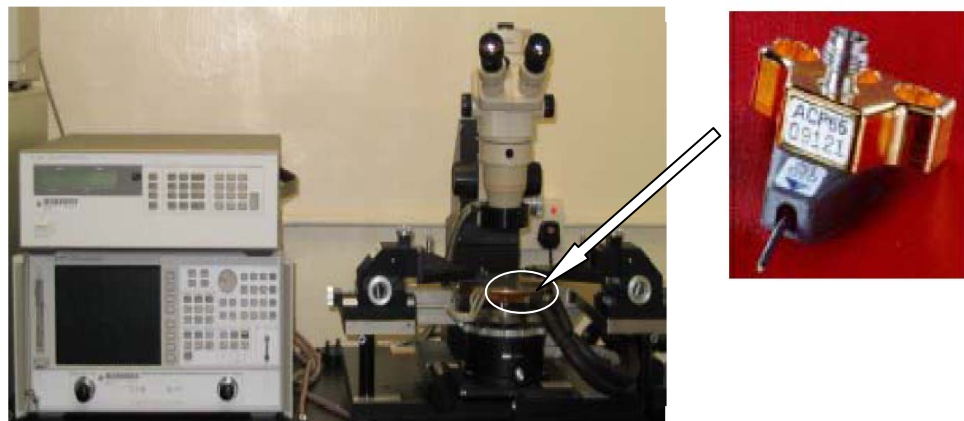
Fig. 2.4   The photograph of the GSG probe and experimental setup of network

analyzer and probe station.

The performance measurement was usually carried out at room temperature. The network analyzer and probe station were first calibrated. This step aimed to remove the parasitics of the probes and connection wires. For the two-port network analyzer. The calibration kit (calkit) of "open", "short", "load" and "thru" impedance standard substrates (ISS) was provided by the probe manufacturer and its information must be strictly followed. For example, "open" has negative capacitance and "short" and "load" have inductance. In the calibration, the automatic Cascade Microtech calibration software "WinCal" was used. A bias voltage was applied through the bias tee of the VNA and the phase shifter was probed using standard ground signal ground (GSG) probes.

The working principle of the network analyzer is based on the idea of electrical matching resonators with their corresponding oscillator circuits. The characteristic admittance (Y) or impedance (Z) and scattering parameters (S_{11}, S_{21}, S_{12} and S_{22}) can be measured over a set of discrete frequency data points. These parameters can also be expressed in different formats, such as rectangular or polar coordinate systems and in Smith chart.

The scattering parameters (S-parameters) are the important parameters in the microwave measurements, since they can well describe the performance of a device over a range of frequency. Also, it is convenient to convert them into different parameters, such as impedance and power dissipations. The S-parameters are the ratio of reflection and transmission coefficients between the incident and reflected waves, and can be characterized by a magnitude in decibel (dB) and expressed as S_{ij}, where $i, j = 1$ or 2. Figure 2.5 shows the details of S-parameters. In characterizing a tunable microwave phase shifter, S_{21} and S_{11} were plotted as a function of frequency.
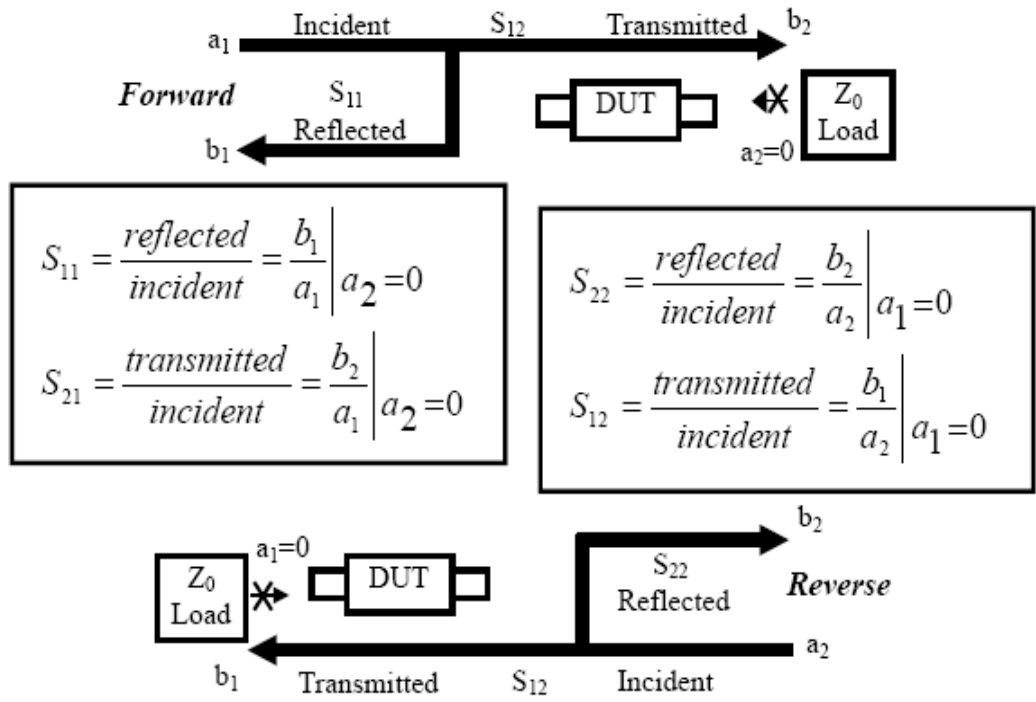
Fig. 2. 5　Detailed information of *S*-parameters.

2.5 Summary

A number of advanced techniques were used in the fabrication and characterization of BST thin films. In this chapter, we have only demonstrated three typical techniques. In the following chapters, more discussions on the fabrication and characterization techniques may be given whenever necessary.

Effect of lattice engineering on the in-plane ferroelectric and dielectric properties of BST

3.1 Introduction

The term "lattice engineering" in the study of ferroelectric oxide thin film refers to the technical method by which the ferroelectric and dielectric properties of the oxide are modified through the adjustment of lattice tetragonality by choosing appropriate substrates [R. E. Cohen and H. Krakauer, 1990; V. Nagarajan, 2000; J. H. Chen, 2002; Woo Young Park, 2003]. The heterostructure barium titanate on $GaMnO_3$ single crystal is a good example showing the effect of lattice engineering. A small lattice mismatch between the thin film and the substrate generated an epitaxial strain introduced to the thin film, which consequently led to an increase in Curie temperature (T_c) of $BaTiO_3$ by nearly 500 °C and produces a remnant polarization of at least 250% higher than bulk $BaTiO_3$ single crystals [K. J. Choi, 2004]. Similar enhancement of ferroelectricity has also been realized in the thin films of strontium titanate ($SrTiO_3$) and lead strontium titanate ($Pb_xSr_{1-x}TiO_3$) [J. H. Haeni, 2005; D. Y. Wang, 2005; Y. Lin, 2005; S. W. Liu, J. Weaver, 2005].

For BST thin films, there is also some work reported in literature to investigate the effect of substrates on the BST structure and properties. As we have noticed, however, most of the work is not systematic and some of results in the literature are even contradict each other. More importantly, the samples studied in the literature

often have a configuration of parallel-plate capacitor (i.e., electrode/BST/electrode/substrate), which is different from the typical configuration of microwave phase shifters (they often have a configuration of coplanar electrode capacitor; i.e., electrode/BST/substrate). Additionally, coplanar electrode capacitors have been obtained considerable attention due to better films quality and orientation control. Furthermore, coplanar electrode offers us a favorable tool to study the influence of lattice mismatch. Interdigital capacitors (IDC) are one of the most promising figures in microwave applications. They are widely used as lumped elements in monolithic microwave integrated circuits (MMICs) [Y. Hargsoon , 1996], slow wave devices, integrated optical (IO) modulators, deflectors, thin-film acoustic electronic transducers [S. Spartak,1999], tunable devices, and dielectric studies on thin films [R. Lgreii, 2004]. Therefore, in our study, the electrical properties of BST films were carried out along the in-plane direction with IDC electrode.

Based on the literature review, we have conducted experiments on integration of BST thin films on single crystal substrates (without bottom electrode) and characterization of the in-plane dielectric and ferroelectric properties. The BST that we chose to investigate has a composition of $Ba_{0.70}Sr_{0.30}TiO_3$. Bulk ceramic of $Ba_{0.70}Sr_{0.30}TiO_3$ is known to have a perovskite structure with a lattice constant $a_{BST} = b_{BST} = c_{BST} = 0.397$ nm at room temperature. In this study, three types of substrates were used:

1) $MgAl_2O_4$ single crystal. It has a spinel-type structure with a lattice constant of $a_{MgAl2O4} = 0.808$ nm, about two times of a_{BST}. The small lattice mismatch ($|2a_{BST} - a_{MgAl2O4}| / a_{MgAl2O4} \approx 1.7$ %) makes it possible for BST to grow epitaxially on $MgAl_2O_4$. Because of the small dielectric constant, loss tangent

and high irradiation-resistance of $MgAl_2O_4$, the heterostructure $BST/MgAl_2O_4$ may provide an ideal model structure for tunable microwave devices (the typical heterostructures under current investigation for microwave applications include $BST/LaAlO_3$, BST/MgO etc). Little research has been conducted regarding this heterostructure although the thin films of a few other perovskite oxides (e.g., superconductors) have been integrated on $MgAl_2O_4$ or $MgAl_2O_4$-buffered silicon [R. Ramesh, 1991; Matsubara, 1989; M. Suzuki, 1996]. This is another reason why $MgAl_2O_4$ was chosen in our study.

2) $(LaAlO_3)_{0.3}(Sr_2AlTaO_6)_{0.7}$ (LSAT) single crystal. Given that It has perovskite structure with a lattice constant of $a_{LSAT} = 0.386$ nm and a comparatively small dielectric constant (≈ 25) and a low dielectric loss($<10^{-4}$), LAST is widely used as a suitable substrate for tunable microwave devices. Structure and dielectric properties at low and microwave frequency are investigated in our work.

3) $LaAlO_3$ single crystal. $LaAlO_3$ also has a small dielectric constant, loss tangent and good lattice match with BST (lattice constant of $LaAlO_3$ ~3.80 nm). It has been widely used as substrates in the study of BST thin films. In our research, the focus will not be put on the integration of BST on $LaAlO_3$. Instead, a systematic change of BST thickness will be realized aiming to examine how the substrate effect changes with film thickness.

In the study of the substrate effect, we have discovered that the lattice structure of the thin film may not be always directly correlated with the lattice structure of the substrate. Thus we have also conducted experiments to fabricate the homostructure of $SrTiO_3/SrTiO_3$ aiming to examine the influence of processing parameters on the lattice structure of the deposited thin films. The reason we did not choose to fabricate

homostructure of BST/BST is simply because there is no BST single crystal substrates available. Quite obviously this part of work is still relevant to the study of the lattice engineering effect in BST.

3.2 Experimental procedure

3.2.1 Thin film deposition and structural characterization

In this study, a 200 nm thick $Ba_{0.7}Sr_{0.3}TiO_3$ thin film was deposited on a single-crystal substrate through pulsed laser deposition, using a 248 nm krypton fluoride (KrF) excimer laser (Lambda Physik COMPex 205). The energy level and repetition rate of the laser were 250 mJ and 10 Hz, respectively. The distance between the target ($Ba_{0.7}Sr_{0.3}TiO_3$ ceramic) and the substrate was fixed at 5 cm. During the deposition, the substrate temperature was maintained at 750 °C and the oxygen partial pressure was kept at 27 Pa. After deposition, the thin film was annealed in air at 1000 °C for 3 h to improve its crystallinity and to reduce oxygen vacancies.

The crystallographic characterization was performed on a Bruker AXS D8 Discover x-ray diffractometer. The surface morphology of the BST thin films was observed using an atomic force microscope (AFM, Digital Instrument Nanoscope IV) in tapping mode. Transmission electron microscopy (TEM) studies were carried out on a JEOL JEM-2011 microscope operated at 200 kV to observe the crystal structure and interfaces at the atomic level.

3.2.3 Dielectric and ferroelectric measurements

The dielectric and ferroelectric properties were determined along the in-plane [100] direction of the thin films. The dielectric measurements were carried out on an impedance analyzer (HP4194A, Hewlett Packard). The ferroelectric tests were carried out on a ferroelectric analyzer (TF-2000, AixACCT Systems GmbH, Germany) equipped with a high-voltage module. A temperature controller (Cambridge, UK) was employed in the measurements to control the measurement temperature.

The samples for the measurements have a co-planar capacitor-type configuration, as shown in Figure 3.1 Gold electrodes were prepared by magnetron sputtering followed by standard photolithography and wet chemical etching methods.
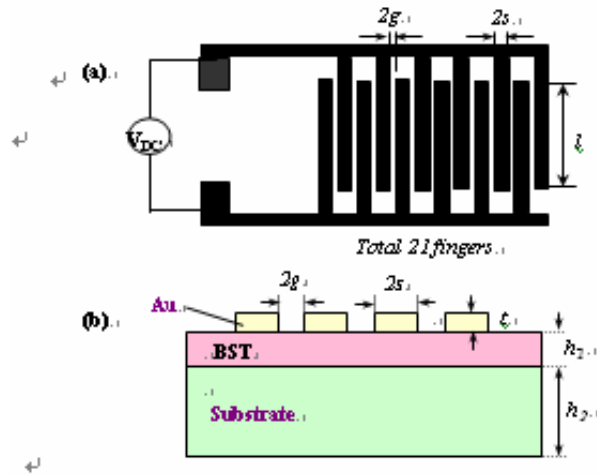
Fig. 3.1   (a) Geometries of the interdigital electrodes: l = 925 µm, 2s = 5 µm and 2g = 3 µm. (b) Side-view of the samples: t = 200 nm, h1 = 20 to 300 nm and h2 = 500 µm.

3.3 Structure and properties of BST films grown on MgAl$_2$O$_4$

3.3.1 Surface morphology

The surface morphology of the freshly deposited BST thin film was observed under an atomic force microscope (AFM, Digital Instrument Nanoscope IV) in tapping mode. Figure 3.2 shows a typical AFM image of the thin film. The grains are found to be uniform in size with an average diameter of about 50 nm. The root-mean-square (rms) roughness of the film is about 2.3 nm over a 1×1 μm^2 scanning area, implying a flat film surface.
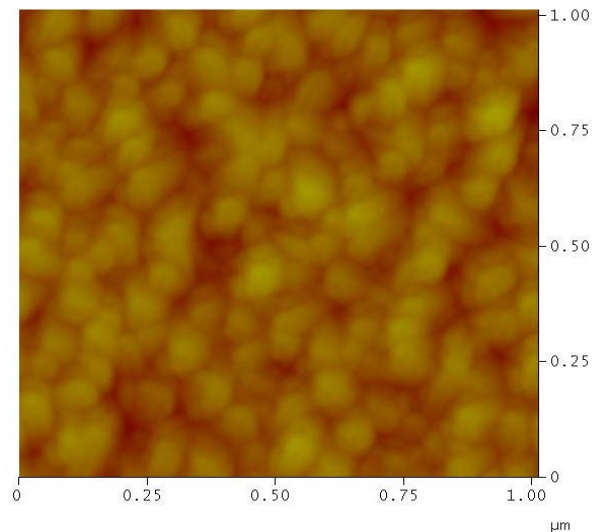
Fig. 3.2   Surface morphology of BST thin film grown on MgAl$_2$O$_4$ single crystal substrate.

3.3.2 Lattice structure

Figure 3.3 shows the x-ray diffraction (XRD) results. The $\theta/2\theta$ scan indicates that the BST thin film has a pure perovskite phase with lattices highly oriented along the (00l) direction. The rocking curve taken around the BST (002) reflection has a

full width at half maximum (FWHM) of ~0.1°, indicating the good crystallinity of the film. The off-axis ϕ scans of the BST (202) and $MgAl_2O_4$ (404) reflections reveal a "cube-on-cube" epitaxial growth mode of BST on the spinal. The epitaxial relationship can be written as: $[100]_{BST}$ // $[100]_{MAO}$ and $(100)_{BST}$ // $(100)_{MAO}$, which is schematically shown in Figure 3.4. Note that the lattice constant of BST is about half of that of spinel, therefore the volume of a BST unit cell is about 1/8 of the volume of a spinel unit cell.
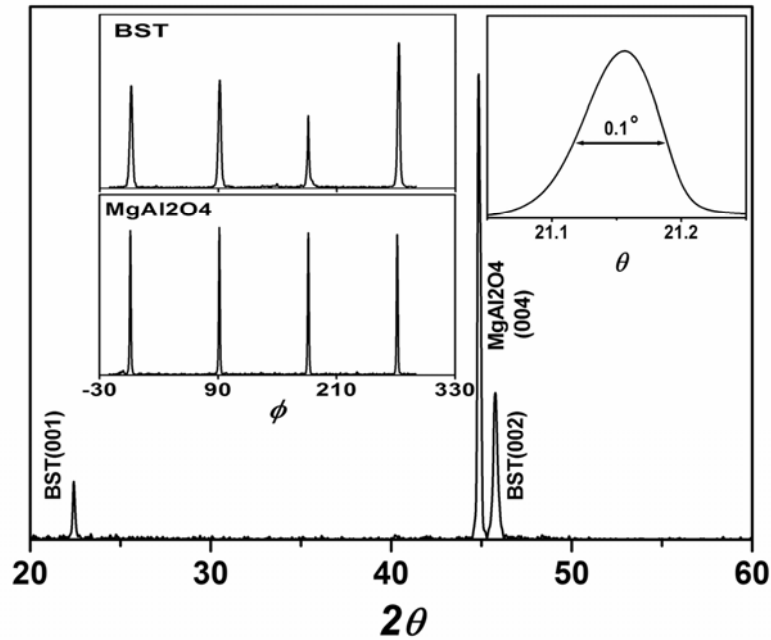
Fig. 3.3   XRD patterns of $\theta/2\theta$ scan of the heterostructure $Ba_{0.7}Sr_{0.3}TiO_3$ /$MgAl_2O_4$. The insets show the rocking curve of the (200) peak (right) and ϕ-scan of (202) reflections of the $Ba_{0.7}Sr_{0.3}TiO_3$ thin film and $MgAl_2O_4$ substrate (left).

From the XRD patterns, the lattice spacing d_{002} and d_{202} were calculated by using Bragg's equation, and then the out-of-plane lattice parameter c $(=2d_{002})$ and the in-plane lattice parameter a $(=2/\sqrt{d_{202}^{-2} - d_{002}^{-2}}\,)$ were obtained [E. D. Specht, 1998]. It

was found that, unlike $Ba_{0.7}Sr_{0.3}TiO_3$ ceramic which has a cubic lattice structure with $a = c = 0.397$ nm, the thin film had a tetragonal lattice with $a = 0.3989$ nm, $c = 0.3943$ nm and thus a tetragonality $a / c = 1.012$. The expansion of the lattice along the in-plane direction was caused by the lattice mismatch between BST and the substrate. Since $MgAl_2O_4$ has a spinel-type face-centered cubic structure with lattice parameters $a = c = 0.808$ nm, the lattice parameter of the oxygen sublattice is about 0.404 nm which is ~1.7% larger than BST. The lattice distortion of BST thin film on $MgAl_2O_4$ is similar to the case of BST on MgO (cubic, $a = c = 0.420$ nm). Other factors such as anisotropic thermal contraction and oxygen deficiency may also influence the lattice distortion of BST [J. H. Chen, 2002; N. Navi, 2003].
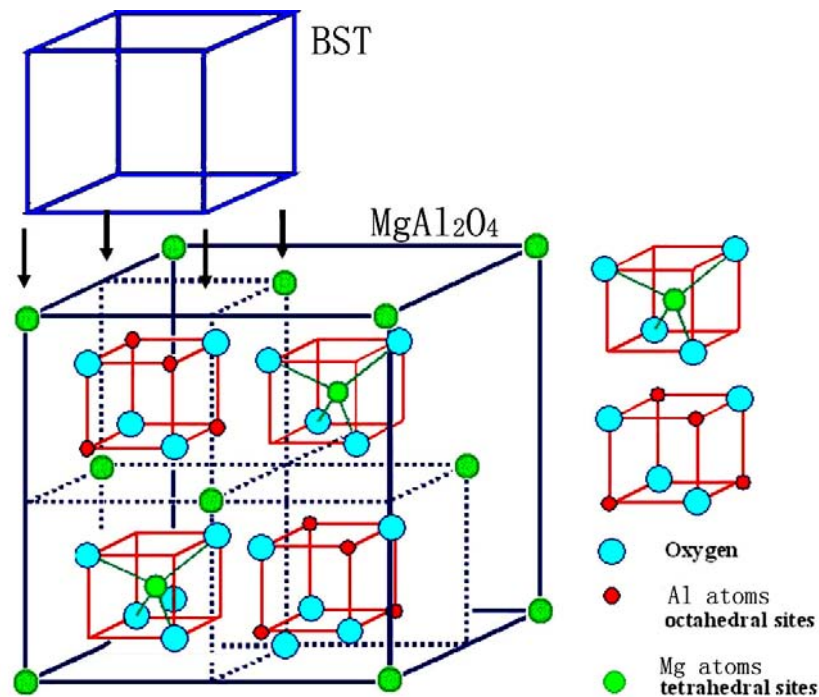
Fig. 3.4   Schematic diagram showing the epitaxial relationship of the BST perovskite lattice and $MgAl_2O_4$ spinel lattice. The schematic structure of spinel is after http://www.tf.uni-kiel.de/matwis/amat/def_en/ kap_2/illustr/spinel.gif.

3.3.3 Interfacial structure and defects

The cross-sectional TEM image taken along [001] zone axis of $MgAl_2O_4$ in Figure 3.5 shows that the BST film has grown columnar and is about 200 nm thick. The density of dislocations is very high near the interface and is reduced as the film becomes thicker. The inset (a) shows the selected area diffraction pattern (SAD) taken in an area including both the substrate and film. Indexes are first made for the substrate followed by the film (using italic numbers) when the spots arise simultaneously from the substrate and the film. It should be noted that $MgAl_2O_4$ belongs to the spinel structure which has a diamond-type structure belonging to FCC unit cell. The (200) diffraction from $MgAl_2O_4$ is due to multiple scattering even though it is kinematical forbidden. The diffraction pattern demonstrates an epitaxial relationship of (100) BST // (100) $MgAl_2O_4$ and [010] BST // [010] $MgAl_2O_4$ between the substrate and the film. However, the film also contains a noticeable amount of misoriented grains which shows a slight contrast in Figure 3.5. Most of these misoriented grains nucleated at the middle of the film which could be caused by the defects generated during the grain growth. The results of the nano-beam electron diffraction (NBED) studies show that the angles of misalignment are various and often exceed 10 degrees. The NBED diffraction pattern in inset (b) was taken from the grain marked as G1 which shows a tilting of nearly ten degrees away from the [001] zone axis. Inset (c) is a high resolution image taken at the interface between a well aligned grain and the substrate. It should be noted that the noise of the image has been suppressed by applying a circular mask on the power spectrum of the image. The high resolution image shows the grain has grown epitaxially on the substrate.
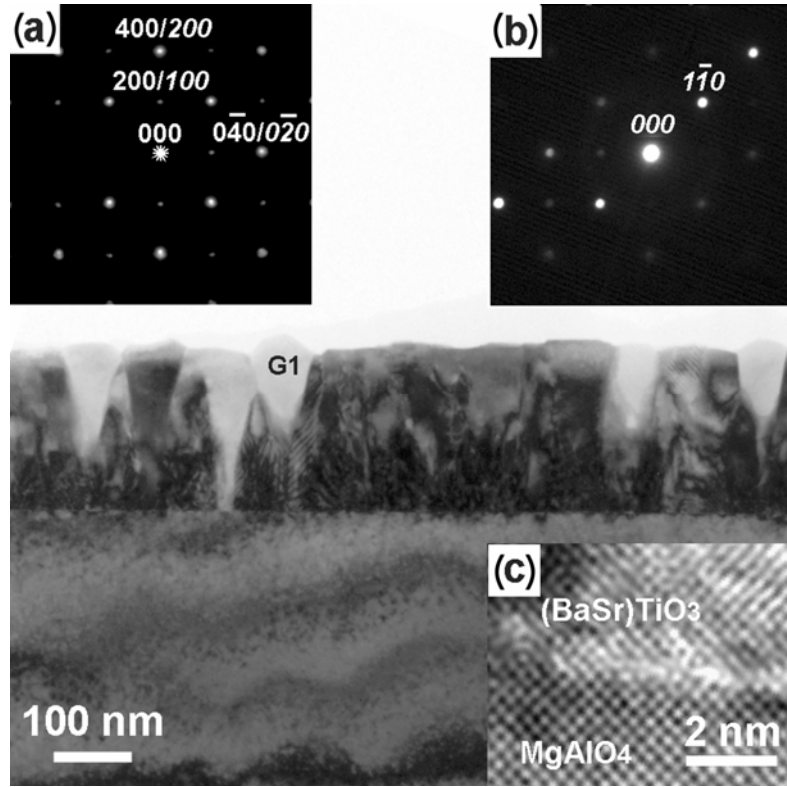
Fig. 3.5   Cross-sectional structure of BST/spinel under transmission electron microscope. The insets a): selected area diffraction pattern taken from an interface; b) nano-beam electron diffraction pattern taken at G1; c) a high resolution 600k interface image taken at the interface between a well aligned grain and the substrate.

3.3.4 In-plane dielectric and ferroelectric properties

The in-plane dielectric properties of BST have been determined. Figure 3.6 shows the temperature dependence of the dielectric constant of BST thin film. The Curie temperature of the BST film is found to be at ~ 78 °C, which is about 45 °C higher than that of the $Ba_{0.7}Sr_{0.3}TiO_3$ ceramic ($T_c = 33$°C, also shown in Figure 3.6) [H. Landolt, 2002]. The normalized dielectric constant ε_N [= (ε under bias) / (ε under zero bias)] vs. DC bias field E of the BST film is shown in the inset of Figure 3.6.

Butter-fly shaped ε–E curves were observed. The BST has displayed a good in-plane dielectric tunability, which is up to 30% under a DC field of 13.3 V/μm. The dielectric loss of the interdigital capacitor was also measured (data not shown). The value of tan δ was found to be dependent on the temperature and DC bias and change from ~0.2% to 4%.
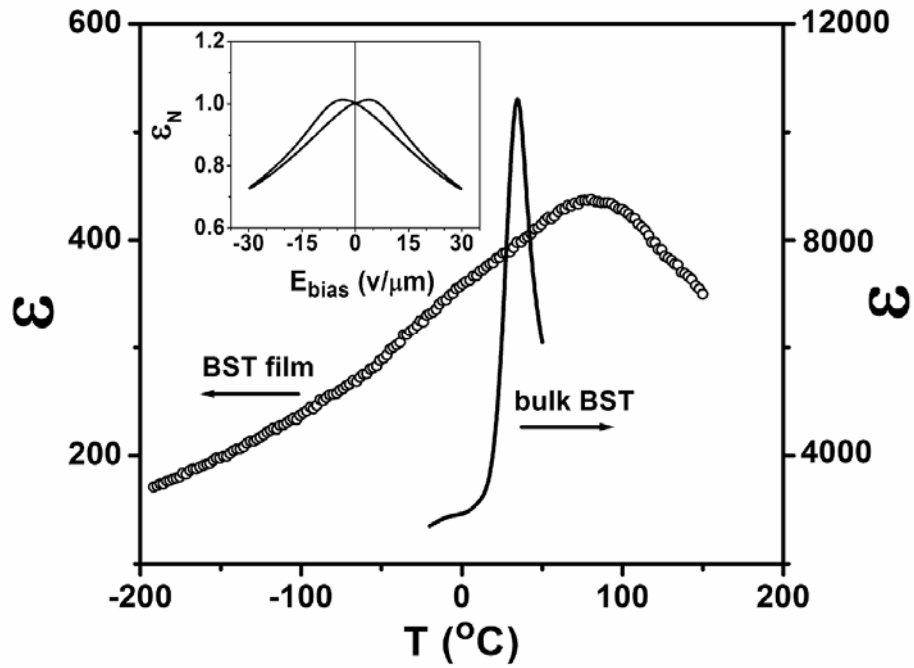
Fig. 3.6   Temperature dependence of the dielectric constant of $Ba_{0.7}Sr_{0.3}TiO_3$ thin film (in-plane) grown on $MgAl_2O_4$ and $Ba_{0.7}Sr_{0.3}TiO_3$ ceramic. The data for the ceramic were after Ref. [H. Landolt, 2002]. The inset shows the dependence of the normalized dielectric constant on dc bias of the $Ba_{0.7}Sr_{0.3}TiO_3$ thin film.

The in-plane ferroelectric properties of the BST thin film were also determined. Well-defined ferroelectric hysteresis loops were obtained and a typical sample is shown in Figure 3.7. Under an external electrical field up to 20 V/μm, the remnant polarization P_r and coercive field E_c of BST were found to be 7.1 μC/cm^2 and 1.2

V/μm, respectively. In comparison with $Ba_{0.7}Sr_{0.3}TiO_3$ ceramic which has a linear

P-E relationship at room temperature (i.e., $P_r \approx 0$) [S. M. Rhim, 2000], the tested

BST thin film possesses a significantly enhanced ferroelectricity along the in-plane

direction. This result is consistent with the T_c shift observed in the dielectric tests.
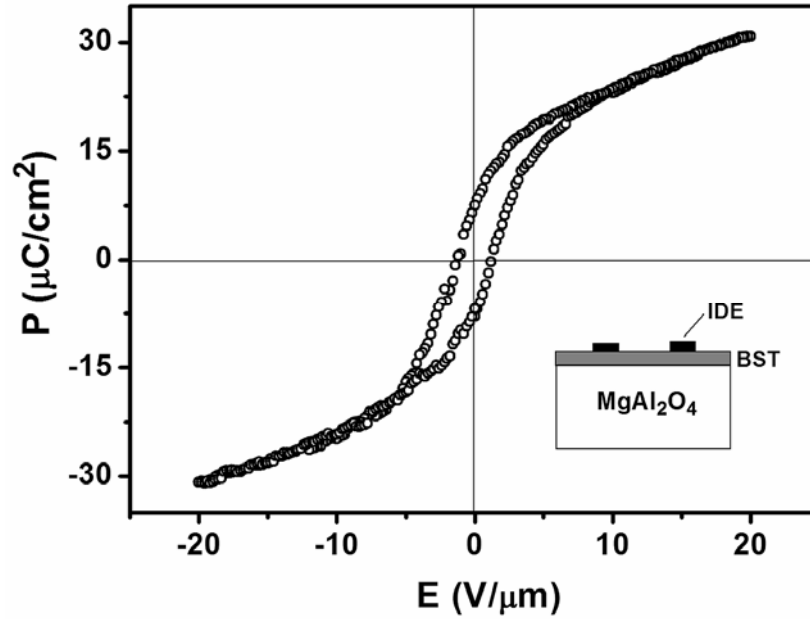
Fig. 3.7   In-plane ferroelectric hysteresis loop of $Ba_{0.7}Sr_{0.3}TiO_3$ thin film grown on

MgAl$_2$O$_4$.

3.3.5 A short discussion

We owe the above-mentioned T_c-shift and ferroelectric enhancement to the

lattice distortion of BST, which is schematically shown in Figure 3.8. The elongation

of lattice along an in-plane direction (Figure 3.8(b)) in BST thin film has caused

enhancement in the ferroelectric behavior. The mechanism is the same as that for the

ferroelectric enhancement in barium titanate and strontium titanate thin films [K. J.

Choi, 2004; J. H. Haeni, 2005]. Quantitative explanation based on a

phenomenological model will be given later in Chapter 4.
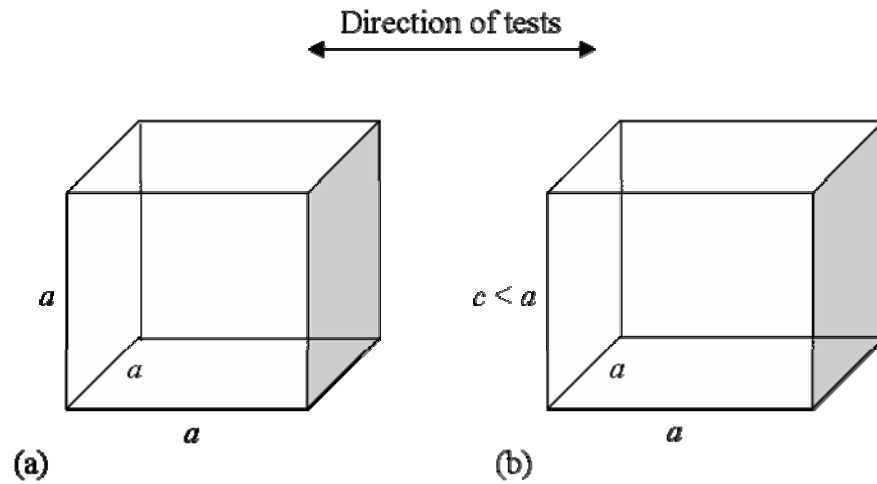
Fig. 3.8   Schematic lattice structures for (a) bulk BST and (b) BST grown on MgAl$_2$O$_4$. The elongation of lattice along in-plane direction is responsible for enhanced ferroelectric polarization along the same direction.

3.4 Structural and properties of BST films grown on LSAT

3.4.1 Crystal structure of BST films

The structure of the BST 70/30 thin film was investigated by means of AFM and XRD. AFM observation indicates that the film has a smooth and dense surface, as shown in Figure 3.9. The average grain size was estimated to be ~ 60 nm in diameter. The root-mean-square (r.m.s.) roughness is about 1.7 nm over a 1×1 μm^2 area of the film.
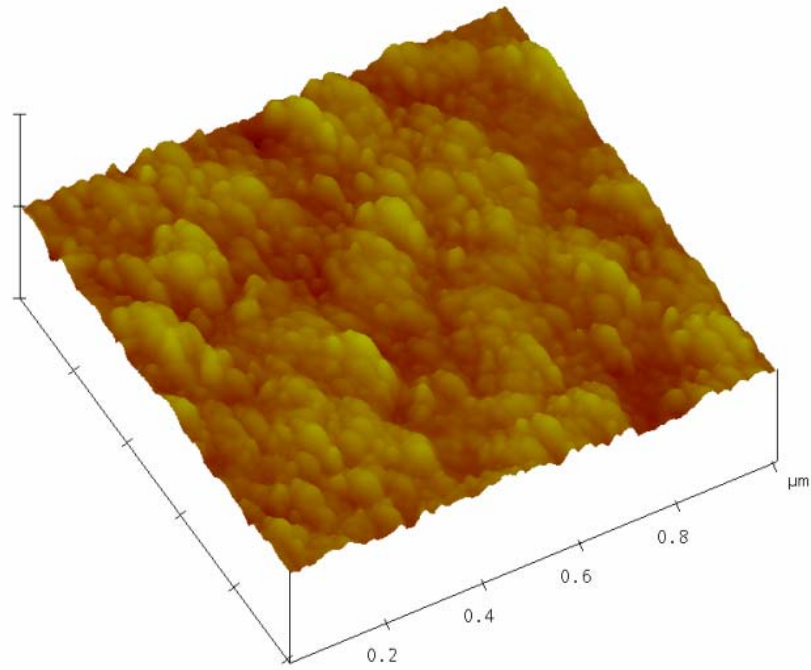
Fig. 3.9   Atomic force image of the BST 70/30 thin film on LSAT.

Figure 3.10 shows the typical θ-2θ X-ray diffraction patterns of the sample. Only BST (00l) peaks appear together with the corresponding reflection from LSAT substrates, indicating the as-grown BST films were perovskite phase and highly c-axis oriented nature. A rocking curve with respect to the (002) direction of the BST film was obtained, as shown in the inset of Figure 3.10. The full-width-half-maximum (FWHM) was found to be ~ 0.063°. The sharpness and high intensity of these peaks implies that the film has good crystallinity. The in-plane alignment of the BST thin film with respect to the major axes of the (001)LSAT substrate was also confirmed by the XRD off-axis Φ scan of the BST (202) and LSAT (202) reflections(not shown here), indicating a good heteroepitaxial growth of the BST thin film. The lattice parameters of the BST 70/30 thin film have been obtained based on the X-ray diffraction data. The

in-plane lattice parameter, a, and out-of-plane lattice parameter, c, were found to be 0.3997 and 0.3971 nm, respectively. As compared with the cubic structure ($a = c = 0.3965$ nm) of BST 70/30 ceramics, the thin film has a slightly distorted lattice structure, i.e, an elongation along the in-plane direction. Such distortion is believed to be the result of the cooperation of lattice mismatch between BST and LSAT (for LSAT, $a = c = 0.3868$ nm) and oxygen deficiency.
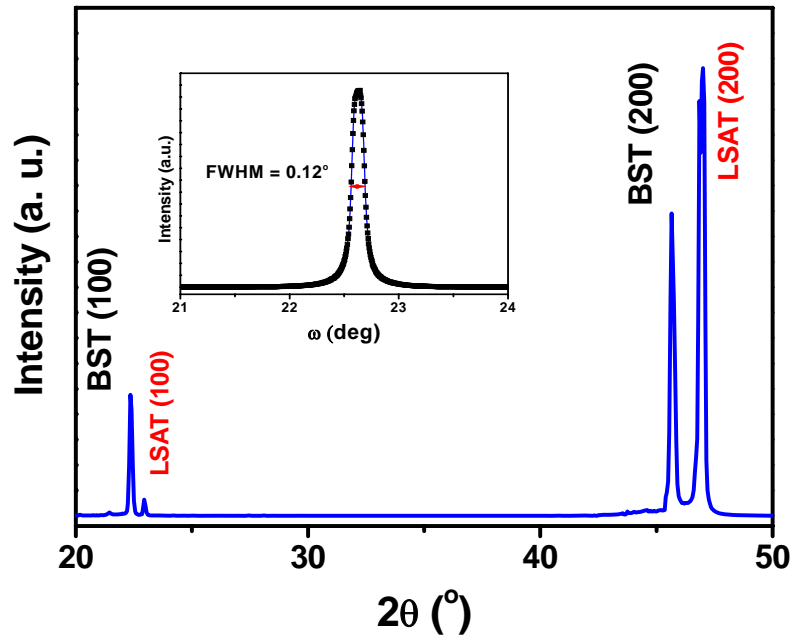
Fig. 3.10   X-ray diffraction pattern of BST 70/30 thin film grown on LSAT (001) substrate. The inset shows the rocking curve of BST.

High resolution X-ray reciprocal space mapping was employed to further investigate the epitaxial quality. Reciprocal space maps (RSMs) are obtained by running ω scans for different values of 2θ and plotting the recorded intensities in a 2D frame. Figure 3.11 is the schematic of reciprocal space for the diffraction nods, and the dash-dotted boxes roughly indicate the areas of

data. Figure 3.12 shows the RSM around the symmetric reflections of BST (200) and LSAT (200). The vertical axis is the ω-2θ scans with the origin at the peak of substrate and the horizontal axis is the ω scans, which measure the relative angles between the atomic planes of the substrates and films. Each ring in the pattern consists of equi-intensity spots. The BST (200) spots, which indicate the existence of c-axis orientation, were observed. The difference in ω axis, $\Delta\omega$, between the highest points of BST (200) and LSAT (200) is nearly zero, suggesting that the (001) plane of BST is parallel to the (200) plane of the substrate and has no detectable tilt, which is consist with the small FWHM (0.063°) of BST (200) reflection. The $\Delta\theta$ between the film and the substrate is -0.69°, indicating the larger lattice constant of the film compared to that of the substrate.
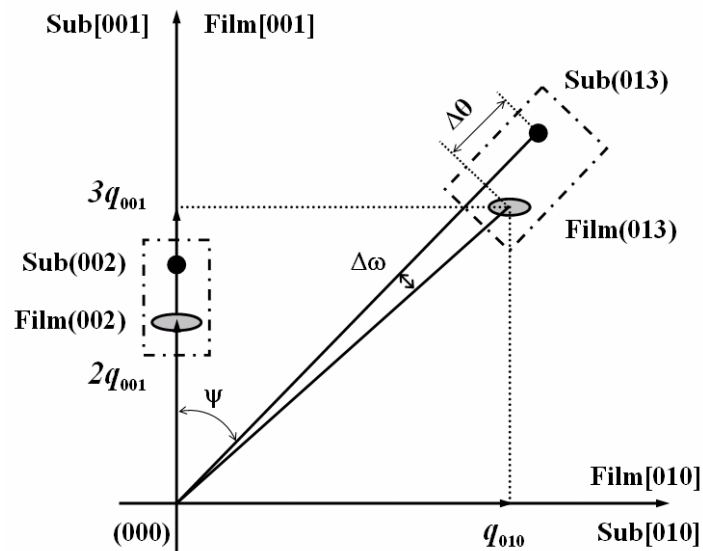
Fig.3.11   Schematic   of   reciprocal   space   for   diffraction   nods   of film(002),Sub(002) ,Film(013),and Sub(013).
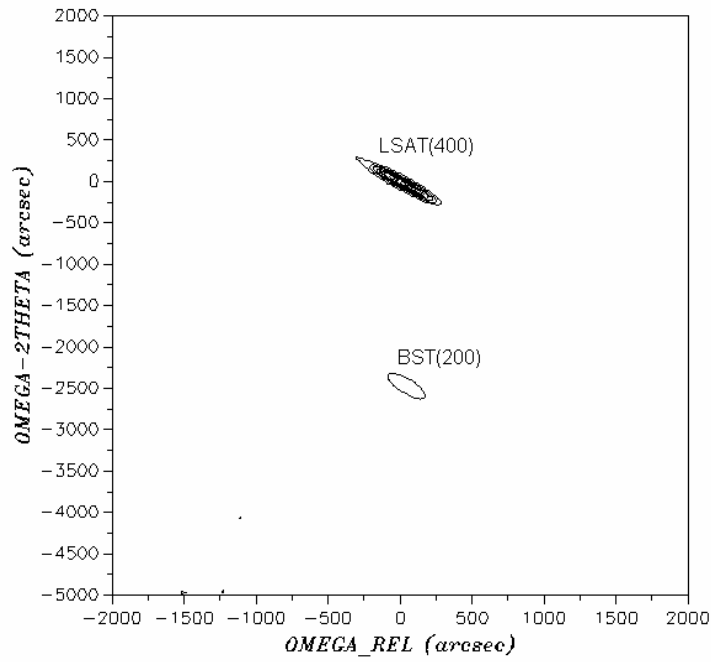
Fig. 3.12. Reciprocal space maps around BST (200) and LSAT (200) reflections

3.4.2 In-plain dielectric properties of BST films

The slight distortion makes the lattice of the BST 70/30 thin film has a tetragonal symmetry (tetragonality a/c = 1.007), suggesting that the film may be in a ferroelectric state at room temperature. This assumption has been confirmed by our dielectric measurement. Figure 3.13 shows the temperature dependence of the in-plane dielectric constant (measured at 100 MHz) of the film. The Curie temperature of the film was found to be 73°C, which is ~ 40°C higher than the Curie temperature of BST 70/30 ceramic. The dielectric constant at Curie temperature of the film, ε_{max}, is 1050, which is only about 10% of that of the ceramic (~11000). Several structural factors give rise to such a small ε_{max} value, among which the very small grain size (thus the proportion of the low-ε grain boundary is relatively high in the film) and clamping effect coming from the film/substrate interface are believed to

be the most influential ones.
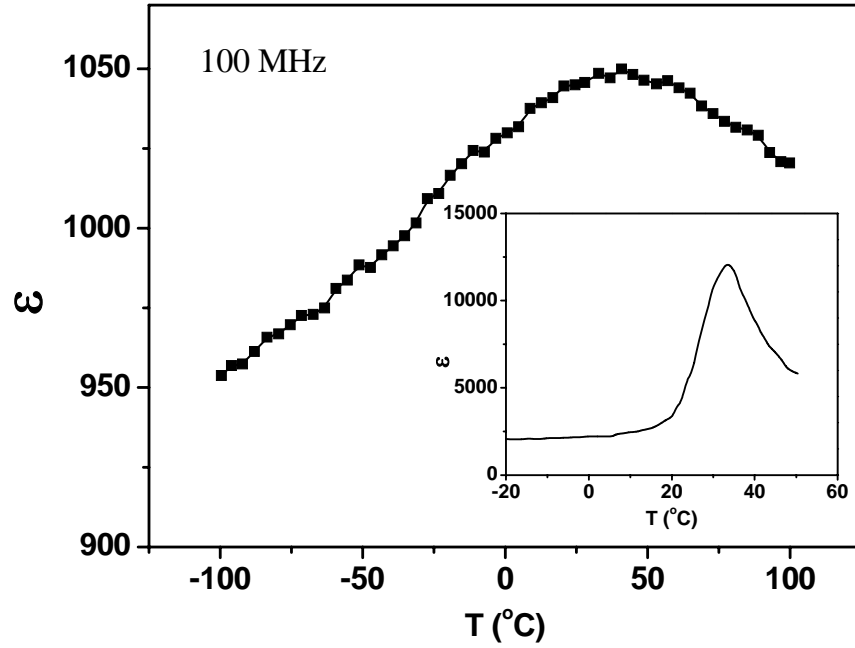
Fig. 3.13　In-plane dielectric constant as a function of temperature for BST 70/30 thin film grown on LSAT (001) substrate. The inset shows the ε-T relationship in BST 70/30 ceramics.

The in-plane *C-V* characteristics of the BST film were investigated over a wide frequency range from 100 Hz to 50 MHz using HP 4292A impedance analyzer and a strong dependence of ε on the DC bias field was observed. As shown in Figure 3.14, the film exhibits a butterfly-shaped ε-*E* and tanδ-*E* dependence which evidenced the enhancement in the in-plane ferroelectric property of the BST film. The tunability is a description of the dielectric constant as a function of DC bias, which is defined as $\Delta\varepsilon / \varepsilon = (\varepsilon_{E=0} - \varepsilon_E) / \varepsilon_{E=0}$, where ε_E and $\varepsilon_{E=0}$ are the dielectric constant measured under a DC bias with field strength E and under no DC bias, respectively. The maximum in-plane dielectric tunability is calculated to be 72% at 1 MHz under a moderate DC

bias field of 13.3 V/µm. In comparison to the parallel-plate capacitors, coplanar designs generally require higher driving voltage and offer lower tunability, but our results are comparable with some of the reported data on BST films based on parallel plate capacitors.
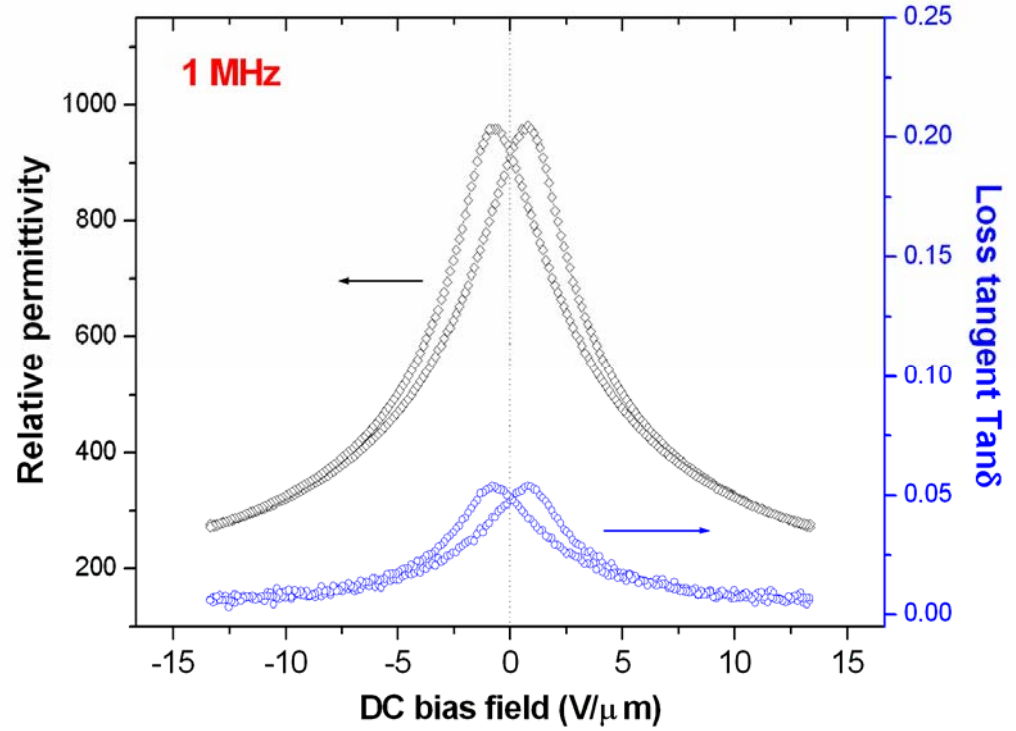
Fig. 3.14   In-plane dielectric tunability as a function of electric field for BST 70/30
thin film grown on LSAT (001) substrate.

Dut to the influence of structure factors, including the interface between the thin film and the substrate, the film thickness and crystallographic orientation in addition to the Ba/Sr ratio, the grain size and dopants, the dielectric properties dependence of films is comparatively more complicated and less clear and complete.

Further characterization has revealed that the dielectric tunability also shows the temperature dependence (measured at 1 GHz). Figure 3.15 shows the $\Delta\varepsilon/\varepsilon$ - E

relationship at four different temperatures - 25, 50, 75 and 100 °C, respectively. The field strength E in this work is defined as the ratio of the DC bias voltage over the gap of two adjacent electrode "fingers" of the IDE. While the shapes of the four curves look similar, the values of the tunability vary with temperature. The best tunability is obtained at 75°C, around the Curie temperature. To raise and lower the temperature both reduces the value of the tunability; however, it seems that the tunability drops faster when the temperature is higher than the Curie temperature. For example, when the temperature increases from 75 °C to 100 °C, the maximum tunability (tested under $E = 20$ MV/m) changes from 35% to 25%, whilst the temperature change from 75 °C to 50 °C can only drop the tunability from 35% to 31%. Such difference is more clearly demonstrated in Figure 3.16, where more data points are given.
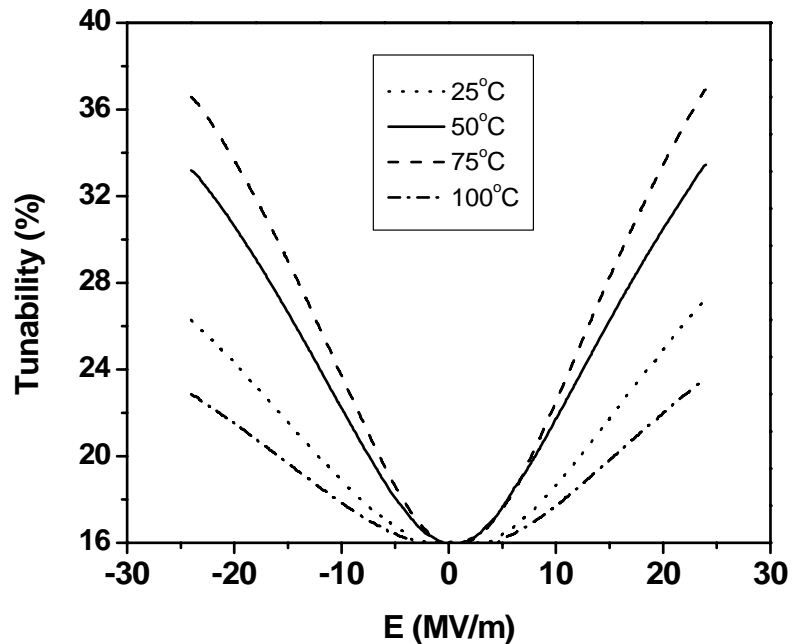
Fig. 3.15   Dielectric tunability as a funcation of electric field in BST thin film grown on LSAT (001) substrate.
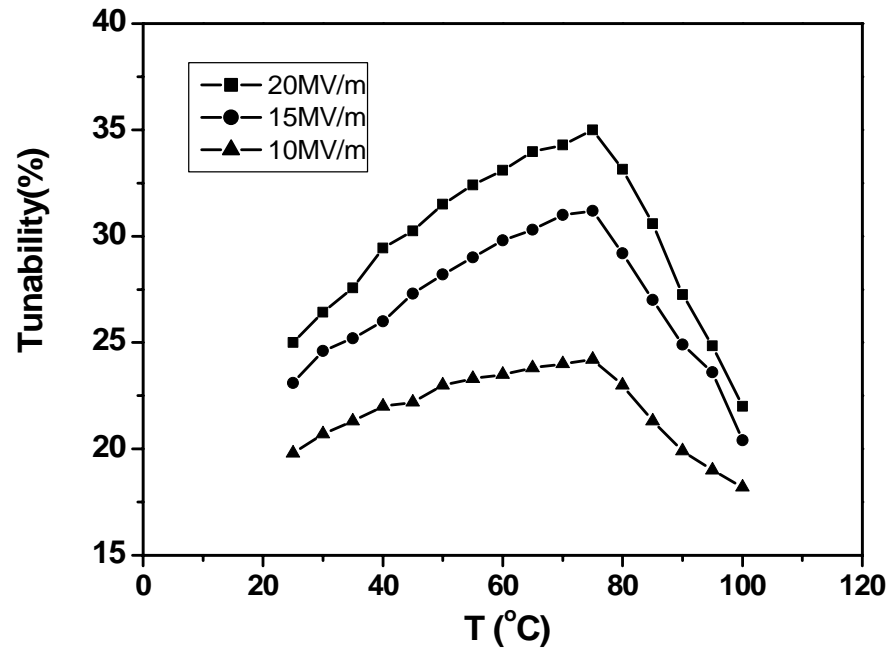
Fig. 3.16   Dielectric tunability as a funcation of temperature in BST thin film grown on LSAT (001) substrate.

By comparing Figure 3.14 and Figure 3.16, it can be observed that the maximum tunability occurs at the Curie temperature of the thin film, regardless of the DC bias field strength. To lower or raise the temperature will reduce the tunability; however, it seems that the tunability decreases faster when the material is in its paraelectric state (the tunability vs. temperature curve above the Curie temperature is more "steep").

The above results, particular the Curie temperature shift and the temperature dependence of the tunability are very useful information for the development of BST-based microwave materials and devices. When choosing appropriate BST composition, it is better to adjust the Ba/Sr ratio to such a number that the thin film's Curie temperature is 10 to 20 °C lower than the working temperature, according to the above results. It is important to note that the thin film's Curie temperature may

not be consistent with that of the ceramics due to the interface effect and oxygen deficiency. In general, if there is a tensile stress along the interface between the film and the substrate, then the Curie temperature of the BST thin film is likely to shift towards the high temperature direction. Reversely a compressive stress may cause the lowering of the Curie temperature of the thin film. These effects, however, are influenced by the state of oxygen deficiency in the thin film. The overall effect is dependent on the processing conditions.

As shown in above, the dielectric tunability is largely dependent on temperature. It was also found that the in-plane dielectric tunability of the BST thin film shows a high frequency dependence. Figure 3.17 shows the $\Delta\varepsilon/\varepsilon$ - E relationship at four different frequence 0.05, 2, 5 and 10 GHz, respectively. As shown in Figure 3.17, it is expected that the dielectric constant at zero bias decreases from 1072 to 645 as the measurement frequencies increase from 50 MHz to 10 GHz. While the shapes of the four curves look similar, the values of the tunability vary with frequency. The tunability under the bias field 13.3 V/μm is amount to 33% at 50 MHz and decreases quickly to about 22% at about 2 GHz. whilst the frequency changes from 2 GHz to 10 GHz, the tunability decreases slowly to about 20%. The dielectric loss was also measured and determined to be close to 0.1 at 10 GHz at room temperature, which indicates that the BST films grown on LSAT are good candidates for practical microwave frequency applications.
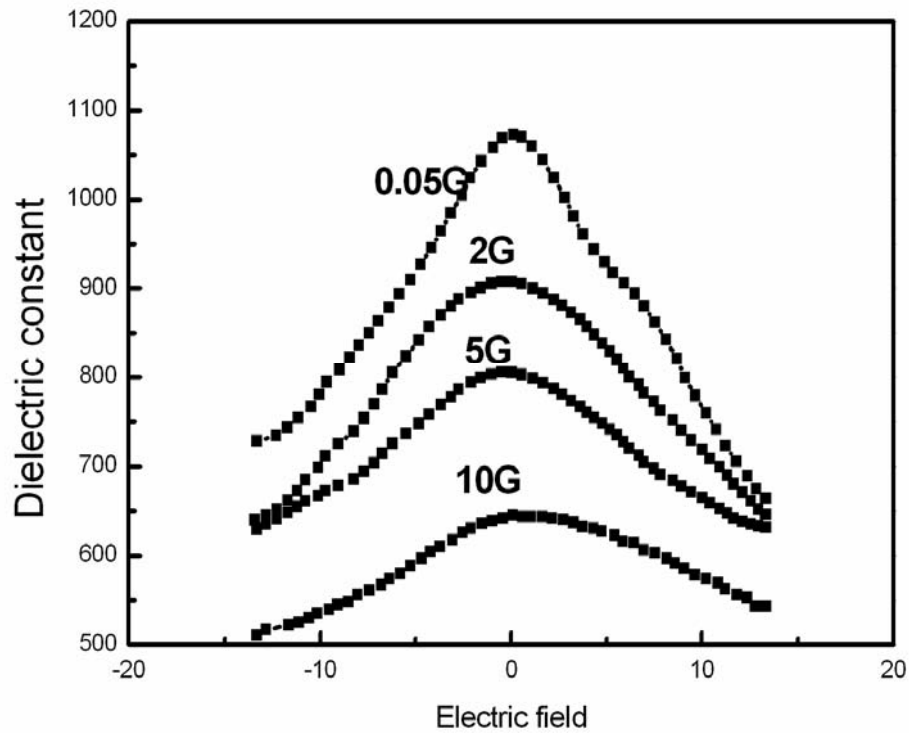
Fig. 3.17   In-plane dielectric constant as a function of electric field for BST 70/30

thin film grown on LSAT (001) substrate at different frequency.

3.5 Structural and properties of BST films grown on LaAlO$_3$

3.5.1 Crystal structure of BST films

The crystal structure of the BST thin films were characterized by x-ray diffraction. The XRD θ-2θ scans revealed that, regardless of film thickness, all BST films were well crystallized and had a pure perovskite phase. The off-axis ϕ scan of the (202) reflection revealed that the films all grew with a "cube-on-cube" epitaxy on the (001) LAO substrate. The out-of-plane lattice parameter (c) and in-plane lattice parameter (a) of BST were determined using the conventional and off-axis θ-2θ scan data (the latter were obtained by tilting the samples at an angle of 45°, followed by

the calculation using the equation: $a = 2/\sqrt{d_{202}^{-2} - d_{002}^{-2}}$, where d_{202} and d_{002} are the lattice spacing of (202) and (002) planes, respectively [E. D. Specht, 1998]. Figure 3.9 shows the thickness dependence of the lattice parameters. The in-plane lattice parameter a (= b) shows a trend of increase with the increasing thickness while the out-of-plane lattice parameter c is almost independent of t. From the figure it seems that t = 150 nm is a critical value: (1) BST with t = 150 nm has a cubic lattice with a = c = 0.3966 nm, which is the same as that of the $Ba_{0.7}Sr_{0.3}TiO_3$ ceramics ($a = c$ = 0.397 nm) [H. Landolt, 2002]. A very slight lattice distortion exists in BST with t < 150 nm. (2) BST films with t > 150 nm have a tetragonal symmetry with $a > c$. When t = 300 nm, for example, a = 0.402 and c = 0.397 nm. The ratio of a / c (defined as tetragonality in this study) increases with increasing thickness [Note that in order to better compare the property vs. lattice relationship in the thin film and ceramic, we have defined the tetragonality as the ratio of the lattice parameter along the direction of the electrical field for the dielectric/ferroelectric tests over the lattice parameter along the direction perpendicular to the electric field]. Therefore the tetragonality of the thin film equals to a/c, while conventionally the tetragonality (for ceramics) is defined as ratio of c/a. This observation of lattice distortion is consistent with results reported by Chen *et al.* [J. H. Chen, 2002]. In a $Ba_{0.50}Sr_{0.50}TiO_3$ (900 nm)/LAO (001) heterostructure, Chen *et al.* observed a lateral lattice expansion (a = 0.401, c = 0.395 nm) in the $Ba_{0.50}Sr_{0.50}TiO_3$ film and he attributed the distortion mainly to the anisotropic thermal contraction during cooling [J. H. Chen, 2002]. We believe the mechanism is also applicable for our BST films with relatively large thickness. For those BST with smaller thickness (t < 150 nm), other factors including lattice mismatch and defects may become influential, which compensates with the lattice

expansion and makes the lattices less distorted [H. J. Gao, 1999; N. Navi, 2003; W. J. Kim, 2000; W. Chang, 1999; N. Yanase, 1999]. A more detailed discussion will be given in later chapters.
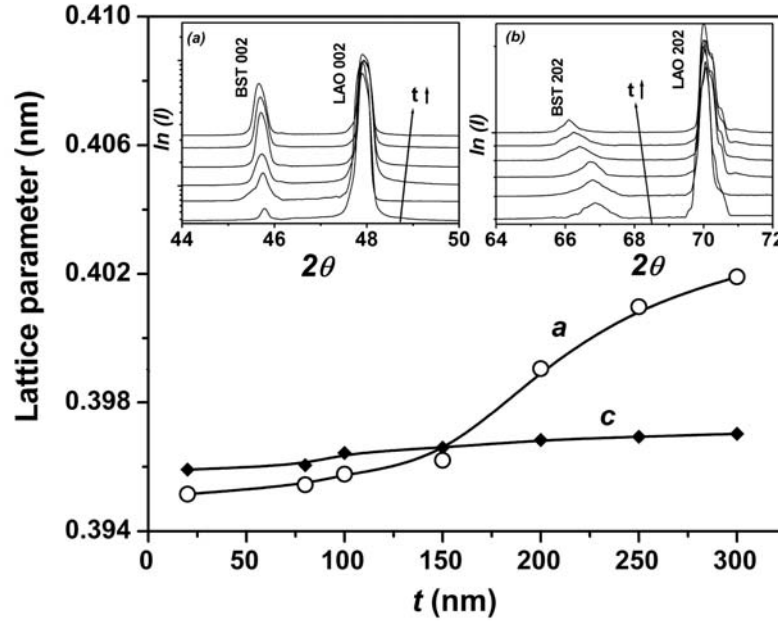
Fig. 3.18   In-plane (*a*) and out-of-plane (*c*) lattice parameters of $Ba_{0.7}Sr_{0.3}TiO_3$ thin films grown on $LaAlO_3$. The inset shows the x-ray diffraction patters of (a) the conventional $\theta/2\theta$ scan and (b) off-axis $\theta/2\theta$ scan.

3.5.2 In-plane dielectric and ferroelectric properties of BST

3.5.2.1 Zero-field dielectric constant vs temperature relationship

Temperature dependence of the in-plane dielectric constant of BST thin films was determined. In the dielectric tests, there was no DC bias applied on the samples. Figure 3.10 demonstrates typical ε - T curves for BST films (with a thickness of 20, 150 and 300 nm, respectively). The dielectric properties of BST ceramics [H.

Landolt, 2002] were also plotted in the figure for comparison. It was found that:

1.   All the BST films exhibit a broad ferroelectric-to-paraelectric phase transition which can be explained as the result of nano-scaled grain sizes of the films.

2.   The Curie temperature (T_c) of BST films shifts to higher temperatures as the film thickness increases. For example, when with t = 20 nm, $T_c \approx 296K$; when t = 150 nm, $T_c \approx 309$ K; and when t = 300 nm, $T_c \approx 350$ K.

3.   The value of dielectric constant of the films increases with increasing film thickness but is always much smaller than that of the ceramics.
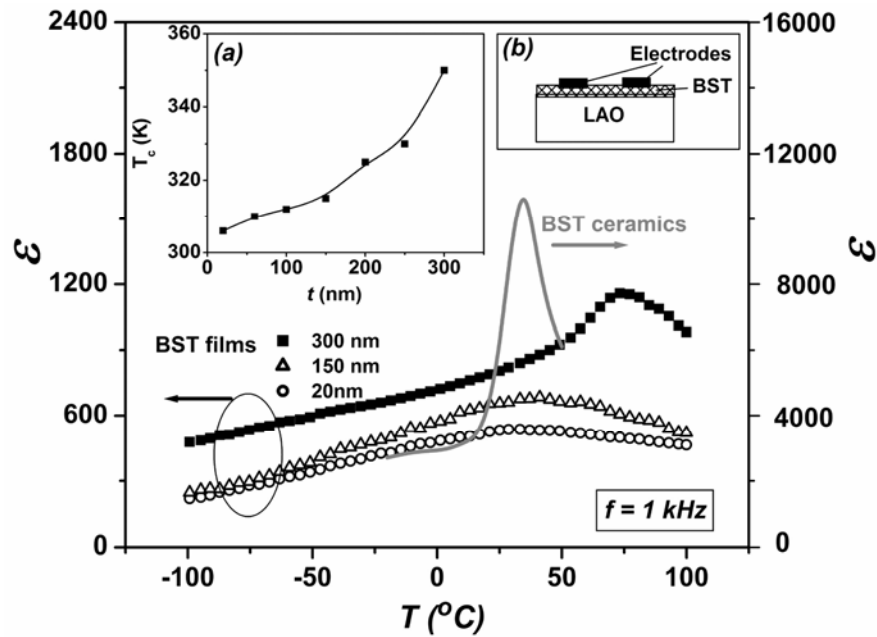
Fig. 3.19   Temperature dependence of in-plane dielectric constant of $Ba_{0.7}Sr_{0.3}TiO_3$ films on $LaAlO_3$ and dielectric constant of $Ba_{0.7}Sr_{0.3}TiO_3$ ceramics. The inset (a) shows the relationship of the Curie temperature of BST films vs. film thickness.

3.5.2.2 Ferroelectric hysteresis loop vs thickness relationship

The dielectric tests imply a trend of enhancement in the in-plane ferroelectric property of the films with larger thickness. This has been confirmed by the ferroelectric test results. Figure 3.11 shows hysteresis loops for the films with thickness = 20, 150 and 300 nm, respectively. Due to different T_c, the three films are in different states (ferroelectric or paraelectric) at room temperature. The 300-nm thick film is in a ferroelectric state because its T_c is far above room temperature; correspondingly the hysteresis loop of the film is a well-defined (although not fully saturated) ferroelectric loop with a remnant polarization (Pr) of 8.4 $\mu C/cm^2$ and coercive field (E_c) of 2.2 V/μm. The hysteresis loop of the film with t = 150 nm is poorly defined (but still indicative of ferroelectric). For the film with t = 20 nm, the polarization-electric field curve can not be regarded as a typical ferroelectric one.
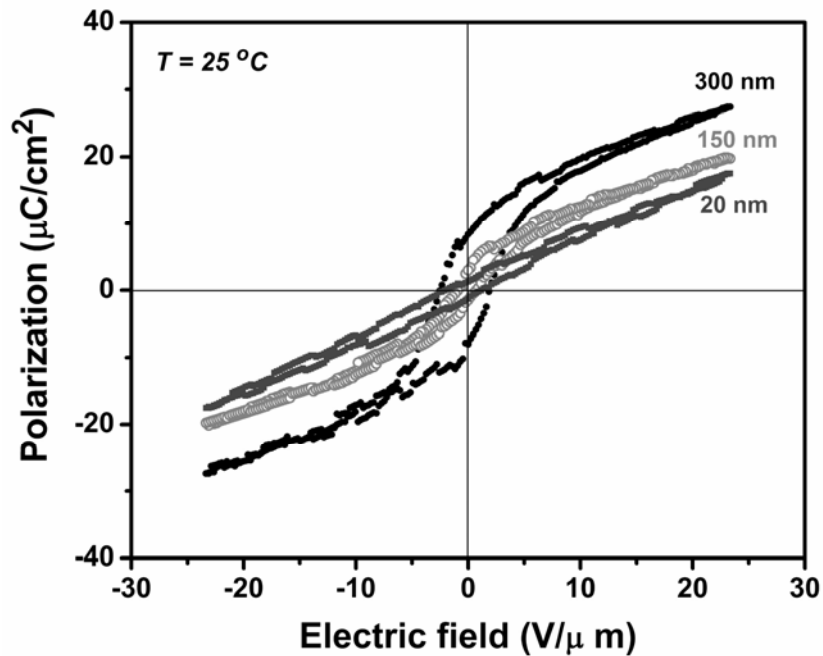
Fig. 3.20   In-plane ferroelectric hysteresis loops of BST thin films deposited on

LaAlO$_3$ substrates.

3.5.2.3 Dielectric tunability of BST thin films

A strong dependence of ε on the dc bias field was observed by the in-plane C-V characteristic of the BST film with thickness of 300 nm. Figure 3.12 shows the dielectric constant and dielectric loss as a function of the surface electric field (E is defined as the ratio of dc bias over finger gap). The measurement is carried out at room temperature and 1 MHz with DC bias sweeping from negative bias field (-13.3 V/μm) to positive bias field (13.3 V/μm) and back again. Interesting phenomena observed in the sample include:

(1)   The butterfly-shaped ε-E dependence confirms the ferroelectric nature of BST thin films. The coercive field calculated from the occurrence of maxium dielectric constant is in agreement well with the value obtained from the P-E loop.

(2)   As expected, the tunability increases with the increasing of electric filed. When E_{max} = 13.3 V/μm, the tunability of dielectric constant $\Delta\varepsilon/\varepsilon$ = 66% while the tunability of loss tangent $\Delta(\tan\delta)/\tan\delta$ = 86%.

Film thickness also has influence on the ε-E curve. As film thickness decreases, the two ε - E peaks get close to each other and the maximum tunability decreases. Figure 3.13 shows the dielectric tunability vs. film thickness relationship. The maximum dielectric tunability of these three films is 66%, 47% and 27%, respectively.
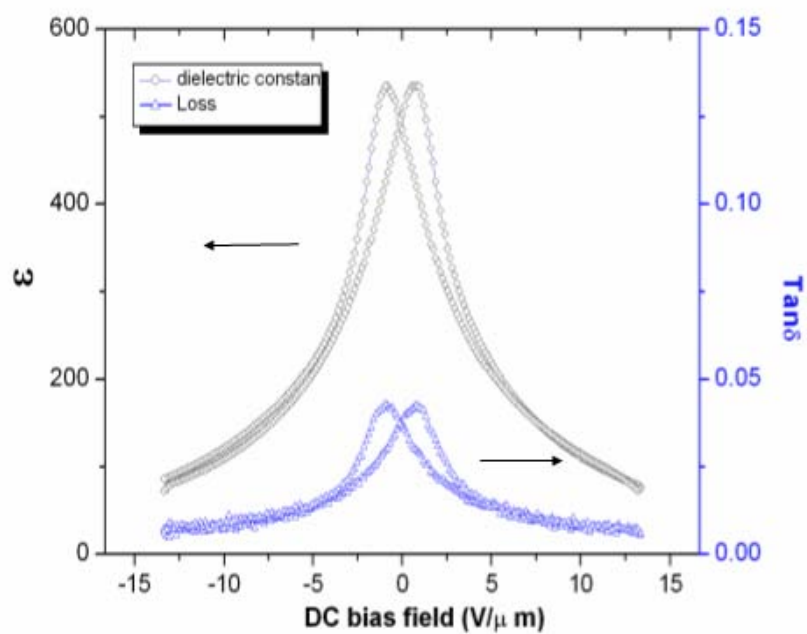
Fig. 3.21   Dielectric constant and loss tangent as a function of dc bias in the 300 nm

thick $Ba_{0.7}Sr_{0.3}TiO_3$ thin film.
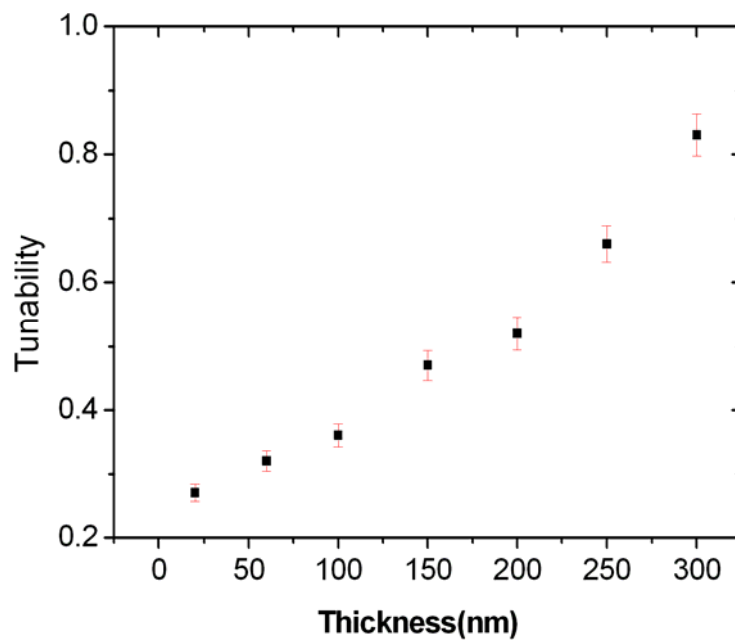
Fig. 3.22   Dielectric tunability as a function of film thickness.

3.6 Discussion

The above experimental results are summarized in Table 3.1. Quite obviously, BST films with a larger thickness exhibit an enhanced ferroelectricity (higher T_c and larger polarization) and larger dielectric constant. While a detailed and theoretical discussion will be given in Chapter 4, in this section we simply analyze the structural factors that are responsible for the observed behaviors.

Table 3.1 Outline of in-plane dielectric and ferroelectric properties of BST films

Thickness (nm)	ε (at room temperature)	Tunability (under 13.3V/μm)	T_c (°C)	Pr (μC/cm^2)
20	540	0.27	23	1.07
50	570	0.32	37	1.23
100	620	0.36	42	2.76
150	660	0.47	45	3.29
200	750	0.52	52	4.28
250	780	0.57	57	5.02
300	820	0.66	77	8.40

We owe the above-mentioned T_c-shift and ferroelectric enhancement to the lattice distortion of BST. Figure 3.14 shows the T_c versus tetragonality dependence of our BST films and BST ceramics (data after H. Landolt, 2002). Both show an upward shift of T_c as the tetragonality increases. The difference is that the variation of tetragonality in BST films is realized by changing the film thickness, while the

variation of tetragonality in the ceramics is obtained by the change of the Ba/Sr ratio. Quite interestingly the latter one seems to be able to more effectively affect the T_c.
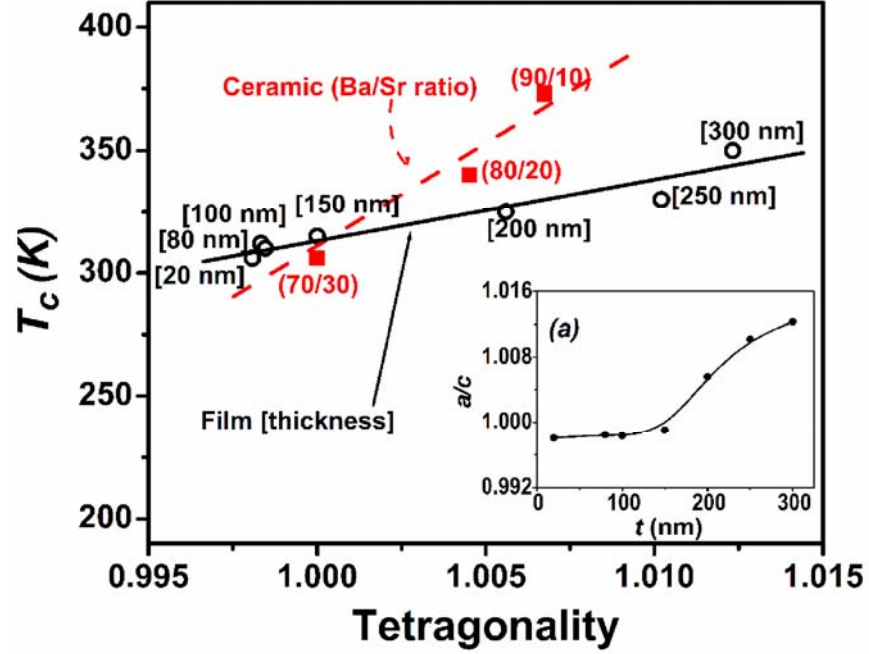
Fig. 3.23   Curie temperature versus tetragonality in $Ba_{0.7}Sr_{0.3}TiO_3$ thin films grown

on $LaAlO_3$ substrate and bulk $Ba_{0.7}Sr_{0.3}TiO_3$ ceramics. The inset shows

the thickness dependence of tetragonality of the thin films.

3.6.1 Structural factors responsible for the ε-t dependence

As shown in Table 3.1, the value of dielectric constant of the BST films increases as the film thickness increases. For example, the room-temperature dielectric constants of the films shown in Figure 3.3 are ε (20 nm) = 540, ε (150 nm) = 660 and ε (300 nm) = 820, respectively. A number of structural factors could affect the value of dielectric constant of a ferroelectric material. In our case, at least the following three factors must be considered: 1) grain size, 2) dead-layer effect and 3) strain and defects. We will try to identify the most critical factor that causes the

above thickness effect.

3.6.1.1 Influence of grain size

In a simplified model, the relationship of the overall dielectric constant of the thin film (ε_{BST}), the dielectric constant of the grains (ε_g) and the dielectric constant of the grain boundaries ($\varepsilon_{g.b.}$) keep a relationship as following:

$$\varepsilon_{BST} = \frac{(\varepsilon_{g.b.} \cdot \varepsilon_g) \cdot (D_{g.b.} + D_g)}{D_{g.b.} \cdot \varepsilon_g + D_g \cdot \varepsilon_{g.b.}}$$

(3.2)

where D_g is the average diameter of the grains and D_{gb} is the average thickness of the grain boundaries.

To examine whether grain size plays a critical role, we may calculate the overall dielectric constant as a function of grain size. For the 20 nm-thick film, we may reasonably assume that ε_g = 1000, $\varepsilon_{g.b.}$ = 30, D_g = 40 nm and $D_{g.b.}$ = 1 nm. By calculation we find that ε_{BST} = 560, which is close to the actual value (540). Now let's check the case of the 300 nm-thick films. The actual dielectric constant of the film is 820. In order to achieve this value, we must have D_g = 150 nm if we keep the other three parameters unchanged. This result is obviously unreasonable because in our experiment, we have found that the grain size of the films is almost a constant despite the thickness variation. The grain size difference between different samples is within 10 nm. This calculation suggests that the grain size variation cannot be the critical factor responsible for the thickness dependence of dielectric constant of BST.

3.6.1.2 "Dead-layer" effect

In ferroelectric thin film-based parallel plate capacitors, a similar thickness

effect has been reported and studied [C. Zhou, 1997; A. K. Tagantsev, 1995; D. D. Fong, 2004; W. L. Zhong, 1997]. This phenomenon is quite similar to our results; i.e., the effective dielectric constant increases as the thickness of the ferroelectric film increases. A so-called "dead-layer" model is often used to explain the thickness dependence of the dielectric constant [K. Natori, 1998; B. T. Lee, 2000; O. G. Vendik, 1998]. As shown in Figure 3.15, a thin film is believed to virtually consist of three layers – an intrinsic layer and two dead layers. The intrinsic layer can be regarded as a standard ferroelectric layer. The dead layer, however, is a non-ferroelectric layer which is typically formed as a result of interdiffusion between the ferroelectric oxide and the electrodes. Mainly due to the non-ferroelectric nature and/or the existence of a large concentration of defects, the dielectric constant of the dead layer is much smaller than that of the intrinsic layer. The overall dielectric constant (or called "effective dielectric constant") of the film is thus controlled by the dead layer. As the film thickness increases, the influence of the dead-layer becomes less significant, resulting in an increase of the effective dielectric constant [C. Zhou, 1997; A. K. Tagantsev, 1995; D. D. Fong, 2004; W. L. Zhong, 1997].
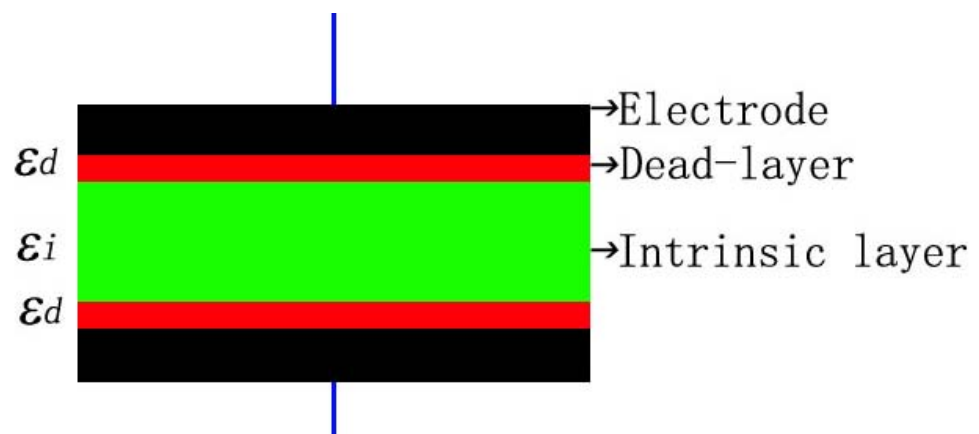
Fig. 3.24   Schematic dead-layer model for interpreting thickness effect in

ferroelectric thin films.

For our samples, however, the thickness effect cannot be understood by applying such "dead-layer" model because the capacitance contribution of the "dead-layer" (the interface between the film and the substrate) to the total capacitance of the coplanar capacitor is negligible, according to the partial capacitance model [S. S. Gevorgian, 1996].

3.6.1.3 Influence of strain/stress

Strain is the relative change in the lattice parameter compared to the relaxed lattice and stress is the force per unit area causing the material to deform from its relaxed state. In linear elastic theory, stress is proportional to strain through the stiffness matrix (C_{ijkl}). Given that the ferroelectric transition is a structural transition, it is reasonable to expect that mechanical pressure applied to the sample may affect the transition. Thin film heterostructures consisting of ferroelectric component are extensively used in modern electronic industry. Since ferroelectrics are a subgroup of piezoelectrics, they all exhibit piezoelectric properties. The coupling between the electrical field and lattice energy plays important role in varing the properties of ferroelectrics. Integration of ferroelectric thin films with lattice-and thermal-expansion-mismatch materials could result in significant strains in ferroelectrics, which in turn affects their physical properties and device performance.

Interfacial strain has been noticed to have influence on the dielectric behaviors of ferroelectric thin films. Pertsev et al. [N. A. Pertsev, 1998] and Schimizu [T. Schimizu, 1997] theoretically showed the critical effects of lattice strain on the dielectric constant of $BaTiO_3$ and $SrTiO_3$, respectively. In particular, Pertsev et al. showed that there is a certain strain value producing the peak dielectric constant. It is

believed that the same strain effect on the dielectric constant holds its validity for the case of BST films.

One of significant factors affecting the dielectric tunability is the structural distortion caused by film strain, which enhances the inverse relationship between dielectric tunability and loss [I. V. Barskii, 1990; W. Chang, 1999; W. Chang, J. S. Horwitz 1999; W. J. Kim, 2000]. The inverse relationship results in either large dielectric tuning with high dielectric loss or small dielectric tuning with low dielectric loss for a reasonably small DC bias voltage and gap size of planar capacitors, depending on either in-plane tetragonal distortion ($a>c$) or normal tetragonal distortion ($a<c$), respectively. Therefore, as long as a strain-induced structural distortion exists in the film, the dielectric properties can never exhibit both large dielectric tuning and low dielectric loss at the same time.

3.6.2 Origin of strain

Various defects in the crystal lattice, whether charged or neutral, can affect properties of dielectrics including perovskite such as BST. The mechanism by which these defects alter the dielectric response is by creating an internally generated electric field, either by means of their own charge, or by causing a deformation of the surrounding volume that change the local fields [M. E. Lines, 1977], then in the first order approximation, the total field acting on the sample is $E_{total} = E_{applied} - \Delta P/\varepsilon$, that means the defective crystal behaves like a perfect crystal biased by an equivalent field $\Delta P/\varepsilon$.

$(Ba_{0.7}Sr_{0.3})TiO_3$ thin films grown on LAO, LAST and MAO (001) substrate by PLD technique were found to both have an elongated in-plane lattice parameter. As a

result of the distortion, the Curie temperature was shifted and the in-plane ferroelectric properties were enhanced as comparing with those of bulk ceramics. These similar behaviors for BST thin films on LAO, LSAT and MAO substrates demonstrate that except the influence of epitaxial stress/strain due to the lattice mismatch, defects, especially oxygen vacancies, play an important role to determine the dielectric and ferroelectric properties of BST films. In the following section, we will conduct experiment to fabricate the homostructure of $SrTiO_3/SrTiO_3$ aiming to examine the influence of oxygen vacancies on the lattice structure of the deposited thin films.

3.6.3 Homoepitaxial growth of STO on STO substrates

To determine the effect of oxygen vacancies on the properties of thin films, we compare the high resolution X-ray reciprocal space mapping of STO thin films fabricated under different ambient pressure. The three samples were prepared by depositing STO thin films with thickness of 100 nm grown on STO substrates. Due to the homoepitaxial growth, the influence from lattice mismatch on the structure can be easily removed, which gives us a possible way to study the effect of oxygen vacancies.

STO thin film was deposited on STO (001) single-crystal substrate through laser molecular-beam epitaxy using a 248 nm krypton fluoride (KrF) excimer laser (Lambda Physik COMPex 205). The energy level and repetition rate of the laser were 250 mJ and 5 Hz, respectively. The distance between the target (STO single crystal) and the substrate was fixed at 5 cm. During the deposition, the substrate temperature was maintained at 750 °C and the oxygen partial pressure was kept at

10^{-3}, 1Pa, 100 Pa respectively. To scrutinize the strain state, asymmetric X-ray reciprocal space mapping (RSM) on $\begin{pmatrix} \bar{1}03 \end{pmatrix}$ reflection was performed using Cu $K_{\alpha 1}$ radiation (Philips X'pert).

Reciprocal space maps (RSMs) are obtained by running ω scans for different values of 2θ and plotting the recorded intensities in a 2D frame. As shown in Figure 3.16, RSM shows a large dependence on the oxygen pressure at 100, 1 and, 10^{-3} Pa. respectively. The STO films at 100 Pa (Figure 3.16 (a)) were coherently grown on STO substrates due to both the in-plane lattice constant ($-\lambda/2Q^{*}_{x}$) and out-of-plane lattice constant ($3\lambda/2Q^{*}_{y}$) have the same value as the supporting substrates. As the growth oxygen pressure decreases to 1 Pa, due to the homoepitaxial growth, there is no change in the in-plane lattice constant. However, the lower oxygen pressure leads to the appearance of oxygen vacancies. The lattice of the films with oxygen deficiency is expected to expand along the out-of-plane direction due to the fact that oxygen vacancies reduce the Coulombic attraction between cation and anion atoms [J. H. Haeni, 2004]. As demonstrated in Figure 3.16 (c), further decreasing the oxygen pressure to vacuum state results in two main points and more elongated along the out-of-plane direction in the reflection pattern of STO films, which indicating two different values of the out-of-plane lattice constant. At the same time, STO films at vacuum pressure still have coherent growth along the in-plane direction.

(a)

Qy*10000(rlu)

Film+Sub

(b)

Qy*10000(rlu)

Sub
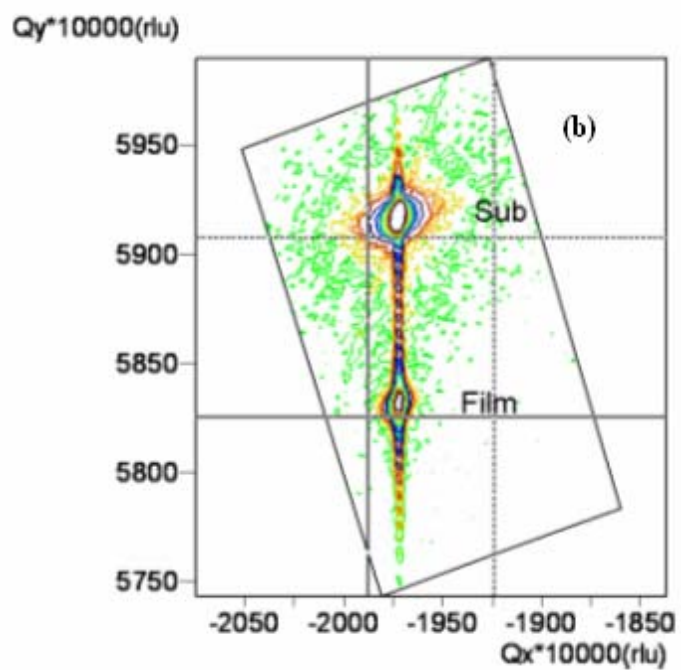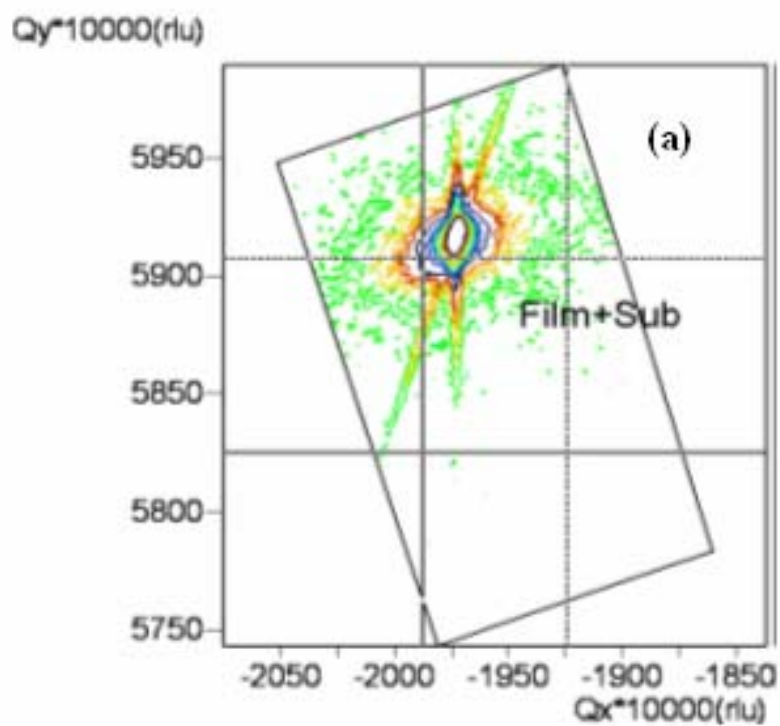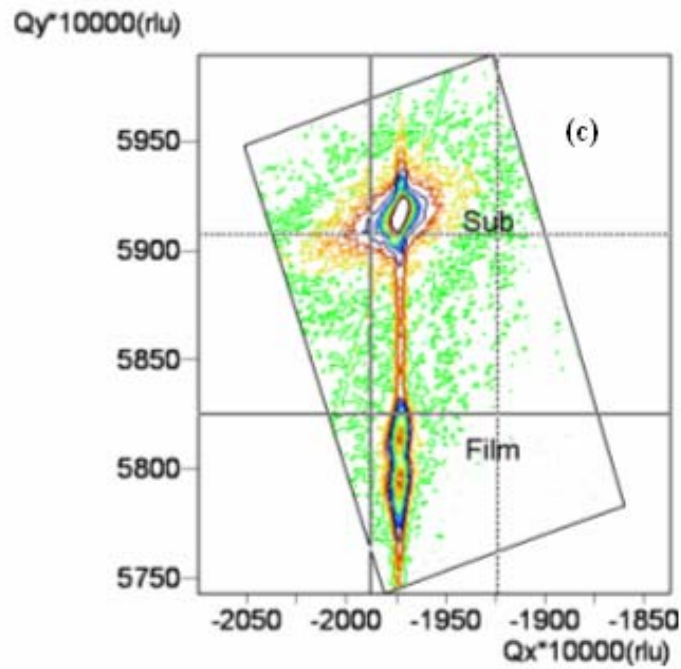
Film

Fig. 3.25   Reciprocal space maps on ($\bar{1}$03) reflections from the STO films grown on

STO (100) substrates with the oxygen pressure of 100 Pa (a), 1 Pa (b) and

10^{-3} Pa (c).

In summary, for homoepitaxial growth of STO on STO substrates, different growth pressure leads to the change of lattice constant along the out-of-plane direction while maintaining the same in-plane lattice constant as the substrates. This change, we believe, is due to the oxygen vacancies since there is no difference in the lattice mismatch as well as the thermal expansion coefficient between the films and substrates. Therefore, oxygen vacancies were found to play an appreciable role in the lattice structure of perovskite thin films.

3.7 Summary

To summarize, we have investigated the structure and properties of BST thin films epitaxially grown on different single crystal substrates and studied the effect of lattice engineering on the in-plane dielectric and ferroelectric behaviors of BST. The results are outlined as below:

(1)   BST thin films were deposited on two types of single crystal substrates – $LaAlO_3$ and $MgAl_2O_4$. The BST thin films are of high crystalline quality and epitaxial in nature.

(2) $(Ba_{0.7}Sr_{0.3})TiO_3$ thin film grown on LSAT (001) substrate was found to have a slightly distorted crystal lattice. As a result of the distortion, the Curie temperature of the thin film was found to be at 73°C which is ~ 40°C higher than that of the bulk ceramic. The in-plane dielectric tunability shows a strong temperature and frequency dependence. These results are believed to be helpful in the development of BST-based microwave materials and devices.

(3)   The lattice parameter of BST thin film is dependent on substrate, film thickness and processing conditions. In most cases, there is a distortion in the lattices of BST thin films as compared with the lattices of bulk BST with the same compositions.

(4)   A correlation between lattice tetragonality and ferroelectric polarization, dielectric constant and dielectric tunability has been established.

(5)   With the aid of homoepitaxial growth of STO on STO substrates and RSM, oxygen vacancies were found to play an important role in the lattice structure of perovskite thin films.

Phenomenological modeling on the structural dependence of dielectric behaviors in BST films

4.1 Introduction

In Chapter 3, we have observed that dielectric constant and tunability of BST thin films increase with increasing film thickness. Lattice distortion rather than grain size variation and dead-layer effect is the key factor responsible for the abnormal dielectric and ferroelectric behavior, as we pointed out. In this chapter, we try to develop a phenomenological model to explain the mechanism of the thickness effect. Basically we need to answer two questions: (1) What are the nature and amplitude of stress/strain in BST thin films? (2) How does the stress/strain affect the dielectric behaviors of BST?

Before the analysis, we need to give a brief introduction of the theoretical work in the literature. M. J. Haun developed a phenomenological thermodynamic theory using a modified Devonshire form of elastic Gibbs free energy. The spontaneous strain as a function of temperature was determined for sol-gel derived $PbTiO_3$ powder [M. J. Haun, 1987]. The theoretical prediction of the phase stability, spontaneous polarization and strains, and dielectric and piezoelectric properties agree well with experimental data. This theory provides us a way of predicting the intrinsic dielectric and piezoelectric properties of perovskite materials. Additionally, O. G. Vendik reported the dependence of the dielectric constant of the ferroelectrics $SrTiO_3$ on temperature and the applied biasing field by solution of the Ginsburg–Devonshire

equation [O. G. Vendik 1997]. Comparison of the simulated and experimental data for both the bulk sample and for the thin film capacitor shows good numerical agreement. This model is intended to be used for developing the computer aided design of microwave components and devices based on ferroelectric films. However, most of the present work is carried on the sandwich structure (electrode/ferroelectrics/electrode) of ferroelectrics. In this chapter, we will report thickness dependence of the dielectric response of BST thin films with coplanar structure by phenomenological thermodynamic theory.

In heterostructures consisting of perovskite-structured oxides and single crystal substrates with a cubic structure, the strain state is related to many structural factors including thermal history, defects (point defects and dislocations), thermal and lattice mismatches between two layers [A. P. Levanyuk, 1988; Y. Takagi, 1948; W. J. Merz, 1950]. Here, we group the strain into biaxial (2-dimensional) and hydrostatic (3-dimensional) components. The sources of biaxial stress are those that directly affect the lattice in only two dimensions. These generally are related to interactions with the substrate and include epitaxial lattice mismatch and differential thermal expansion, but also depend on growth-related parameters [P. W. Forsbergh, 1954; S. T. Lee, 1995; J. A. Thornton, 1989].

A main reason that we consider biaxial and hydrostatic strain in place of usual Cartesian components is that this decomposition helps in understanding the effect of each strain components since the potential sources of hydrostatic stress are physically different from those of biaxial stress [G. A. Rossetti, 1991]. Surprisingly, it also simplifies the theoretical description of the films' dielectric response as presented by C. M. Carlson [C. M. Carlson 2000]. By calculating the residual strain and stress in

terms of hydrostatic and biaxial components from lattice parameters, dependence of dielectric properties on oxygen pressure has been demonstrated. Therefore, consideration and control of both types of strain is important for the optimum performance of devices such as tunable microwave devices and high-density memories.

4.2 Tensor relationships between stress and strain

For cubic materials, by using Voigt notation [M. E. Lines, 1977], the Hooke's law can be written as:

$$\vec{U} = \begin{bmatrix} U_1 \\ U_2 \\ U_3 \\ U_4 \\ U_5 \\ U_6 \end{bmatrix} = \begin{bmatrix} s_{11} & s_{12} & s_{12} & 0 & 0 & 0 \\ s_{12} & s_{11} & s_{12} & 0 & 0 & 0 \\ s_{12} & s_{12} & s_{11} & 0 & 0 & 0 \\ 0 & 0 & 0 & s_{14} & 0 & 0 \\ 0 & 0 & 0 & 0 & s_{44} & 0 \\ 0 & 0 & 0 & 0 & 0 & s_{44} \end{bmatrix} \bullet \begin{bmatrix} \sigma_1 \\ \sigma_2 \\ \sigma_3 \\ \sigma_4 \\ \sigma_5 \\ \sigma_6 \end{bmatrix} = \hat{s} \bullet \vec{\sigma} \qquad (4.1)$$

where U_i is the strain, σ_i is the stress, and S_{ij} is the elastic compliance. 1, 2, and 3 components are those with respect to the Cartesian axes, and the 4, 5, and 6 are the shear components. The elements of the compliance tensor comply with the restrictions as $S_{12}<0$, $S_{11}+S_{12}>0$, $S_{11}+2S_{12}>0$, and $S_{44}>0$ [O. G. Vendik, 1972; A. F. Devonshire, 1954; R. C. Cammarata, 2000; S. B. Desu, 1993]. The poisson's ratio is $\upsilon = -S_{12}/S_{11}$.

In order to account for the lattice parameters, the stress exerted on the film must have equal in-plane components and out-of-plane component. The resulting in-plane and out-of-plane strain is described as

$$\vec{U} = \begin{bmatrix} U_{xy} \\ U_{xy} \\ U_z \\ U_4 \\ U_5 \\ U_6 \end{bmatrix} = \begin{bmatrix} \sigma_{xy}(s_{11}+s_{12})+\sigma_z s_{12} \\ \sigma_{xy}(s_{11}+s_{12})+\sigma_z s_{12} \\ \sigma_{xy}(2s_{12})+\sigma_z s_{12} \\ 0 \\ 0 \\ 0 \end{bmatrix} = \hat{s} \bullet \begin{bmatrix} \sigma_{xy} \\ \sigma_{xy} \\ \sigma_z \\ 0 \\ 0 \\ 0 \end{bmatrix} \tag{4.2}$$

where U_{xy} is the in-plane strain, U_z is the out-of-plane strain. By inverting, we can calculate the stress in terms of the strain.

$$\vec{\sigma} = \begin{bmatrix} \sigma_{xy} \\ \sigma_{xy} \\ \sigma_z \\ 0 \\ 0 \\ 0 \end{bmatrix} = \frac{1}{(s_{11}-s_{12})(s_{11}+2s_{12})} \begin{bmatrix} s_{11}U_{xy} - s_{12}U_z \\ s_{11}U_{xy} - s_{12}U_z \\ (s_{11}+s_{12})U_z - 2s_{12}U_{xy} \\ 0 \\ 0 \\ 0 \end{bmatrix} \tag{4.3}$$

Using the in-plane and out-of-plane strain and stress, we obtain an alternative decomposition of the stress and strain which is much clearer in their physical sources, namely, hydrostatic and biaxial stress and strain. Hydrostatic stress (σ_{hyd}) is applied to all three principle axes equally, while biaxial stress (σ_{bi}) is applied to only the two in-plane axes. Using again the Hooke's law, we determine the separate effect of σ_{hyd} and σ_{bi}. The strain resulting from the σ_{bi} is

$$\vec{U} = \begin{bmatrix} U_1 \\ U_2 \\ U_3 \\ U_4 \\ U_5 \\ U_6 \end{bmatrix} = \begin{bmatrix} U_{bi} \\ U_{bi} \\ U_{bi}(\dfrac{2s_{12}}{s_{11}+s_{12}}) \\ 0 \\ 0 \\ 0 \end{bmatrix} = \begin{bmatrix} \sigma_{bi}(s_{11}+s_{12}) \\ \sigma_{bi}(s_{11}+s_{12}) \\ 2\sigma_{bi}s_{12} \\ 0 \\ 0 \\ 0 \end{bmatrix} = \hat{s} \begin{bmatrix} \sigma_{bi} \\ \sigma_{bi} \\ 0 \\ 0 \\ 0 \\ 0 \end{bmatrix} \tag{4.4}$$

Similarly, we find the strain resulting from the σ_{hyd} is

$$\vec{U} = \begin{bmatrix} U_1 \\ U_2 \\ U_3 \\ U_4 \\ U_5 \\ U_6 \end{bmatrix} = \begin{bmatrix} U_{hyd} \\ U_{hyd} \\ U_{hyd} \\ 0 \\ 0 \\ 0 \end{bmatrix} = \begin{bmatrix} \sigma_{hyd}(s_{11}+2s_{12}) \\ \sigma_{hyd}(s_{11}+2s_{12}) \\ \sigma_{hyd}(s_{11}+2s_{12}) \\ 0 \\ 0 \\ 0 \end{bmatrix} = \hat{s} \begin{bmatrix} \sigma_{hyd} \\ \sigma_{hyd} \\ \sigma_{hyd} \\ 0 \\ 0 \\ 0 \end{bmatrix} \tag{4.5}$$

Combining the effect of both the hydrostatic and biaxial strain

$$\vec{U} = \begin{bmatrix} U_1 \\ U_2 \\ U_3 \\ U_4 \\ U_5 \\ U_6 \end{bmatrix} = \begin{bmatrix} U_{bi}+U_{hyd} \\ U_{bi}+U_{hyd} \\ U_{bi}(\dfrac{2s_{12}}{s_{11}+s_{12}})+U_{hyd} \\ 0 \\ 0 \\ 0 \end{bmatrix} = \begin{bmatrix} \sigma_{bi}(s_{11}+s_{12}) \\ \sigma_{bi}(s_{11}+s_{12}) \\ 2\sigma_{bi}s_{12} \\ 0 \\ 0 \\ 0 \end{bmatrix} = \hat{s} \bullet \begin{bmatrix} \sigma_{bi}+\sigma_{hyd} \\ \sigma_{bi}+\sigma_{hyd} \\ \sigma_{hyd} \\ 0 \\ 0 \\ 0 \end{bmatrix} \tag{4.6}$$

By comparing this result with Eq.[4.3], we see the relationship between in-plane and out-of-plane strain and the biaxial and hydrostatic component.

$$U_{xy} = U_{bi} + U_{hyd}$$
$$U_z = U_{bi}(\frac{2s_{12}}{s_{11}+s_{12}}) + U_{hyd}$$
$$\sigma_{xy} = \sigma_{bi} + \sigma_{hyd} \tag{4.7}$$
$$\sigma_z = \sigma_{hyd}$$

Based on the discussions shown above, it is possible to calculate the strain and stress from the measured lattice parameter determined from the XRD observation.

4.3 Strain and stress in BST with different thickness

From the lattice parameters presented in Chapter 3, we calculate the in-plane and out-of-plane strain and stress for BST/LAO films with different thickness. The

in-plane and out-of-plane strain is calculated in the usual way from the measured lattice parameters.

$$U_{xy} = \frac{a - a_0}{a_0}$$
$$U_z = \frac{c - a_0}{a_0}$$

(4.8)

where a and c are the measured in-plane and out-of-plane lattice parameters respectively, a_0 is the unstrained bulk parameter for $Ba_{0.7}Sr_{0.3}TiO_3$. That is, we assume that a completely unstrained film would have the same bulk lattice constant.

Figure 4.1 shows the in-plane and out-of-plane strains for the BST films on LAO substrates at different thickness. Figure 4.2 demonstrates the corresponding in-plane and out-of-plane stress respectively calculated using Eq.[4.3] and the compliances $S_{11}= 6.075\times10^{-12}$ m^2/N and $S_{12}= -2.308$ N/m^2 [H. Landolt, 2002], as estimated from those of $SrTiO_3$ and $BaTiO_3$ by means of Vegard's law[L. Vegard, 1921]. As shown in Figure 4.1, 4.2, the strain and stress show a significant dependence on the thickness. Above $t>150$ nm, all these strains and stresses are positive (tensile), consistent with the lattice parameters being larger than that of bulk. Additionally, there is also an increase trend in stress/strain with thickness, for example, the in-plane strain ranging from 5×10^{-4} to 12×10^{-4} with the corresponding stresses ranging between 0.2 GPa and 0.6 GPa. Moreover, the out-of-plane strain is ranging from 0.8×10^{-4} to 1.3×10^{-4} with the corresponding stresses ranging between 0.2 GPa and 0.5 GPa. Below $t\leq150$ nm, the stress and strain show a relatively smaller dependence on the thickness comparing with $t>150$ nm associated with a different trend. All these stress and strain are negative (compressive), consistent with the lattice parameters being smaller or close to the bulk BST.
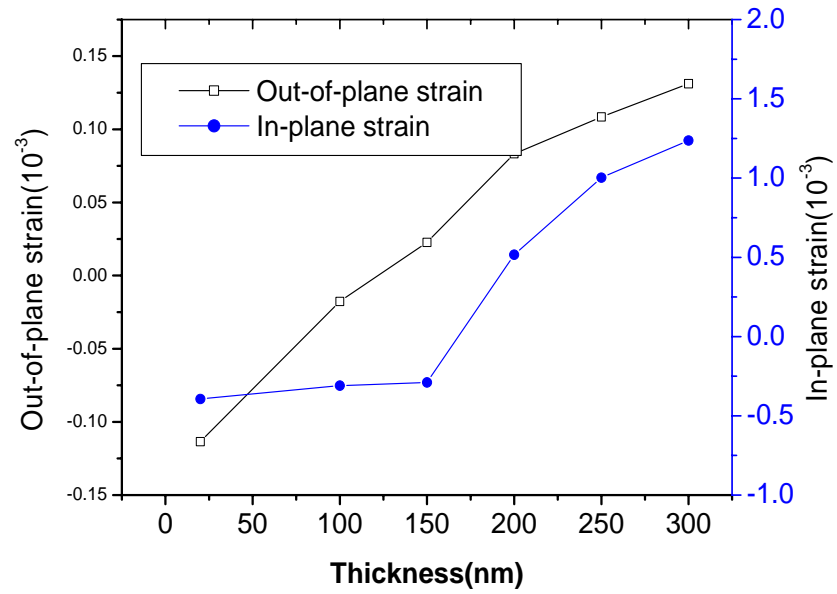
Fig. 4.1   The in-plane and out-of-plane strains for the BST films on LaAlO$_3$

substrates at different thickness.
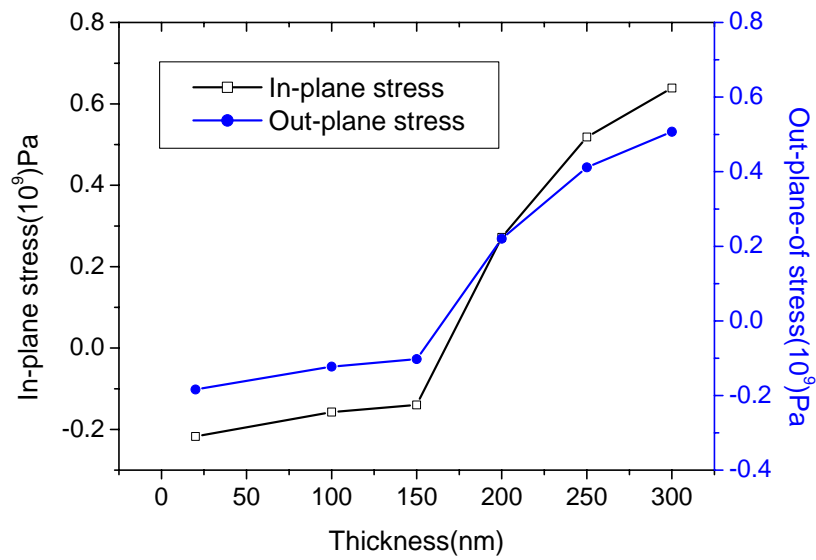
Fig. 4.2   The in-plane and out-of-plane stresses for the BST films on LaAlO$_3$

substrates at different thickness.

According to the relationships determined by Eq.[4.7], we can calculate the

strain in terms of hydrostatic and biaxial strain from the in-plane and out-of-plane component. The hydrostatic and biaxial component can be described as

$$U_{bi} = \frac{s_{11} + s_{12}}{s_{11} - s_{12}}(U_{xy} - U_z = 0.550 \bullet (U_{xy} - U_z)$$

$$U_{hyd} = \frac{(s_{11} + s_{12})U_z - 2s_{12}U_{xy}}{s_{11} - s_{12}} = 0.437 \bullet U_z + 0.550 \bullet U_{xy}$$

(4.9)

Figure 4.3 shows the calculated hydrostatic and biaxial strain values for BST films with different thickness. The corresponding stress values are calculated and indicated in Figure 4.4. Comparing with the dependence of in-plane and out-of-plane strain on the film thickness, the hydrostatic and biaxial strain shows the same trend**.** Above t>150 nm, all these strains and stresses are positive (tensile). The relative value of hydrostatic strain is larger than the corresponding biaxial strain. For example, at t =200 nm, hydrostatic strain is 3.2×10^{-4}, while biaxial strain is 1.9×10^{-4}. Also, there is a general increasing trend in stress/strain with thickness. That is, the hydrostatic strain ranging from 3.2×10^{-4} to 7.9×10^{-4} with the corresponding stresses ranging between 0.2 GPa and 0.5 GPa. On the other hand, the biaxial strain ranging from 1.8×10^{-4} to 4.8×10^{-4} with the corresponding stresses ranging between 0.05 GPa and 0.13 GPa. Below t≤150 nm, all these stress and strain are negative (compressive) which show less dependence on the thickness than t>150 nm.
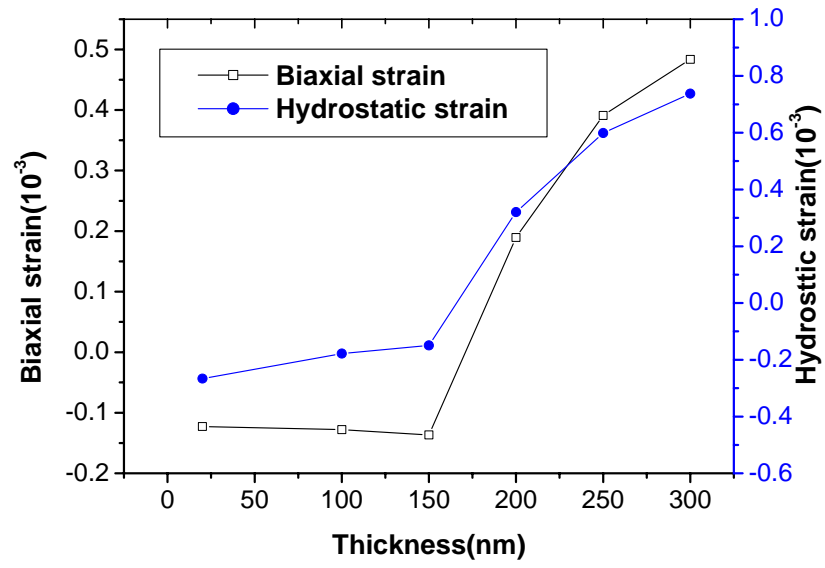
Fig. 4.3　　The biaxial and hydrostatic strains for the BST films on LaAlO$_3$ substrates at different thickness.
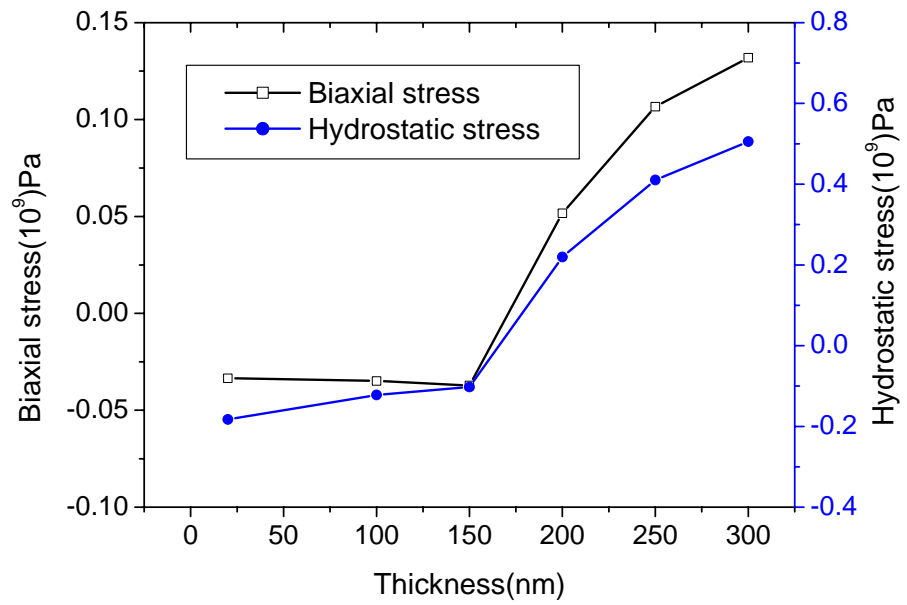
Fig. 4.4　　The biaxial and hydrostatic stresses for the BST films on LAO substrates at different thickness.

For the whole studied thickness range, both the hydrostatic and biaxial strain change from compression to tension with the thickness. Moreover, the relative value of hydrostatic component is larger than that of biaxial component. While the actual mechanism is not well understood, this difference can be explained in terms of the sources of hydrostatic and biaxial strain [O. G. Vendik, 1997; O. G. Vendik, L. T. Ter-Martirosyan, 2000]. The sources of biaxial strain are generally lattice mismatch and thermal expansion mismatch. On the case of BST/LAO, the lattice mismatch is around 4% (a_{BST}=3.965 Å, a_{LAO}= 3.793 Å) without obvious thermal expansion mismatch ($\alpha_{BST}=\alpha_{LAO}$= ~$10\times10^{-6}$/K). The sources of hydrostatic strain are generally point defects. The energetic film growth like PLD is responsible for the large amount of defects like equilibrium concentration of oxygen vacancies and nonequilibrium concentration of interstitial defects. Furthermore, it is reported that the compression leads to the decrease of cell volume and tension to the increase of cell volume [L. Zhang, 1997]. The transition of strain from compression to tension for BST films on LAO substrates leads to the increase of unit cell volume calculated from the XRD observation.

4.4 Effects of strain on dielectric response of BST

So, now that we have determined the strain in our BST/LAO films at different thickness, the remaining challenge is to understand its effect of the dielectric response presented in Chapter 3. The interplay between thermal, elastic, and dielectric properties of macroscopic ferroelectrics can be described by treating the material as a continuum without regard to any underlying atomic structure [B. D. Silverman, 1962; P. W. Forsbergh, 1954; R. C. Cammarata, 2000]. This

phenomenological treatment assumes that the dielectric system can be described by three independent variables chosen from the conjugate pairs (temperature, entropy), (stress, strain), and (electric field, polarization) [M. E. Lines, 1977; T. M. Shaw, 1999; S. K. Streiffer, 1999]. Although there have been a few attempts to model these systems microscopically [O. G. Vendik, 1972; C. M. Carlson, 2000], the complexity of calculation rises quickly due to the strong coupling between the order parameter (polarization) and the strain. Thus, phenomenological theories continue to play a large role in modeling ferroelectric behavior.

4.4.1 Theromodynamic potentials

There are many potentials which describe the thermodynamics of a given system, and the choice of which to use is made such that the independent variables correspond to the experimental conditions of interest, thus the remaining three variables are dependent and determined by the given equation. No one potential contains more or less information than another, but simply describes the same system in terms of different independent variables.

Two popular choices are the Helmholz free energy (A) and the elastic Gibbs energy (G), which describes systems at constant strain and stress respectively [W. Chang, 2000; S. B. Desu, 1996]. G is most often used to describe the properties of bulk ferroelectric materials since experiments on these materials are usually done under constant stress, not strain.

The situation for a thin film grown on thick, rigid substrates is not so clear out. This system does not correspond to one at either completely constant strain or stress, but is "in between" [N. A. Pertsev, 1998]. The films have the in-plane strains given

by the presence of the substrate, while the other dimensions are at constant stress [N. A. Persev, 1998]. According to the equation ($G=A-\sigma_iU_i$), Helmholz free energy (*A*) can be obtained from *G* by adding the terms σ_iU_i, which is knows as the Legendre transformation [M. E. Lines, 1977]. This transformation is used to change the potential at constant stress (*G*) to one at constant strain. So, the new appropriate potential $\breve{G}$ for films on a thick substrate is obtained from *G* using the following Legendre transformation [N. A. Pertsev, 1998]

$$\bar{G} = G + \sigma_1 U_1 + \sigma_2 U_2 + \sigma_6 U_6.$$

$$dG = -SdT - U_i d\sigma_i + E_i dP_i \tag{4.10}$$

The differential form of Ğ is found from that of G in the usual way.

$$d\bar{G} = -SdT + \sigma_1 dU_1 + \sigma_2 dU_2 + \sigma_6 dU_6 - U_3 d\sigma_3 - U_4 d\sigma_4 - U_5 d\sigma_5 + E_i dP_i \tag{4.11}$$

This confirms that functional dependence of Ğ is what we wanted.

$$\bar{G}(T, U_{1,2,6}, \sigma_{3,4,5}, \vec{P}) = G(T, \vec{\sigma}, \vec{P}) + \sigma_1 U_1 + \sigma_2 U_2 + \sigma_6 U_6 \tag{4.12}$$

The equations of state determine the other parameters and given by

$$(\frac{\partial \bar{G}}{\partial T})_{U_{1,2,6}, \sigma_{3,4,5}, P_1} = -S, (\frac{\partial \bar{G}}{\partial [\sigma_{3,4,5}]})_{T, U_{1,2,6}, P_4} = -U_{3,4,5},$$

$$\tag{4.13}$$

$$(\frac{\partial \bar{G}}{\partial [U_{3,4,5}]})_{T, \sigma_{3,4,5}, P_i} = +\sigma_{1,2,6}, (\frac{\partial \bar{G}}{\partial P_i})_{T, U_{1,2,6}, \sigma_{3,4,5}} = E_i$$

4.4.2 Explicit form of G for perovskite ferroelectrics

Using the Landau-Ginsburg-Devonshire formalism the elastic Gibbs free energy was expanded in a power series of polarization assuming isothermal conditions. The

nonzero coefficients of the energy function were limited by the symmetry of the paraelectric phase. G is taken as an expansion in even powers of the polarization and stress with temperature dependence contained in the expansion coefficient. Using Voigt's notation, the elastic energy can be described as [M. J. Huan, 1997]

$$
\begin{aligned}
G =\ & a_1(P_1^2 + P_2^2 + P_3^2) + a_{11}(P_1^4 + P_2^4 + P_3^4) + a_{12}(P_1^2 P_2^2 + P_2^2 P_3^2 + P_3^2 P_1^2) \\
& + a_{111}(P_1^6 + P_2^6 + P_3^6) + a_{112}[P_1^4(P_2^2 + P_3^2) + P_3^4(P_1^2 + P_2^2) + P_2^4(P_1^2 + P_3^2)] \\
& + a_{123} P_1^2 P_2^2 P_3^2 - \frac{1}{2} s_{11}(\sigma_1^2 + \sigma_2^2 + \sigma_3^2) - s_{12}(\sigma_1\sigma_2 + \sigma_1\sigma_3 + \sigma_3\sigma_2) \\
& - \frac{1}{2} s_{44}(\sigma_4^2 + \sigma_5^2 + \sigma_6^2) - Q_{11}(\sigma_1 P_1^2 + \sigma_2 P_2^2 + \sigma_3 P_3^2) \\
& - Q_{12}[P_1^4(P_2^2 + P_3^2) + P_3^4(P_1^2 + P_2^2) + P_2^4(P_1^2 + P_3^2)] \\
& - Q_{44}(P_2 P_3 \sigma_4 + P_1 P_3 \sigma_5 + P_2 P_1 \sigma_6)
\end{aligned}
\tag{4.14}
$$

where P_i and σ_i are the polarization and stress; α_i, α_{ij}, α_{ijk} are the dielectric stiffness and high order stiffness coefficient at constant stress; S_{ij} is the elastic compliance coefficient at constant polarization; and Q_{ij} is the cubic electrostrictive constant in polarization notation [M. E. Lines, 1977; F. Jona, 1987]. Electrostriction is the effect where an applied electric field produces a strain in the material that depends quadratically on the filed (Note that this is different from piezoelectricity where the strain depends linearly on the field).

According to the Eqs

$$
\left(\frac{\partial G}{\partial T}\right)_{\sigma_i, P_i} = -S, \left(\frac{\partial G}{\partial \sigma_i}\right)_{T, P_i} = -U_i, \left(\frac{\partial G}{\partial P_i}\right)_{T, \sigma_i} = E_i
\tag{4.15}
$$

σ_1, σ_2, and σ_6 can be eliminated from the explicit form of $\breve{G}$ and substituted to the coupled expressions for U_1, U_2, and U_3 in terms of σ_1, σ_2, and σ_6 in Eq. [4.10]. Then, the resulting general form of $\breve{G}$ is given in Eq. [4.16]. Here, we are not putting any boundary conditions applying to our specific films. Later, we can apply the

appropriate boundary conditions for the situation of interests.

$$\bar{G} = a_1^* P_1^2 + a_2^* P_2^2 + a_3^* P_3^2 + a_{11}(P_1^4 + P_2^4) + a_{33}^* P_3^4 + a_{12}^* P_1^2 P_2^2 + a_{13}^*(P_1^2 P_3^2 + P_2^2 P_3^2)$$
$$+ a_{111}(P_1^6 + P_2^6 + P_3^6) + a_{112}[P_1^4(P_2^2 + P_3^2) + P_3^4(P_1^2 + P_2^2) + P_2^4(P_1^2 + P_3^2)]$$
$$+ a_{123}P_1^2 P_2^2 P_3^2 - Q_{44}\left(P_2 P_3 \sigma_4 + P_1 P_3 \sigma_5 + P_2 P_1\left(\frac{U_6}{s_{44}}\right)\right) \qquad (4.16)$$
$$+ \frac{1}{2(s_{11} - s_{12})(s_{11} + s_{12})}[s_{11}(U_1^2 + U_2^2) - 2U_1 U_2]$$
$$- \frac{1}{2}s_{44}\left(\sigma_4^2 + \sigma_5^2 + \left(\frac{U_6}{s_{44}}\right)^2\right) - \sigma_3 \frac{s_{12}}{s_{11} + s_{12}}(U_1 + U_2) - \sigma_3^2 \frac{(s_{11} - s_{12})(s_{11} + 2s_{12})}{2(s_{11} + s_{12})}$$

$$a_1^* = a_1 - \frac{(Q_{11}s_{11} - Q_{12}s_{12})U_1 + (Q_{12}s_{11} - Q_{11}s_{12})U_2}{(s_{11} - s_{12})(s_{11} + s_{12})} - \frac{Q_{12}s_{11} - Q_{11}s_{12}}{s_{11} + s_{12}}\sigma_3,$$
$$a_2^* = a_1 - \frac{(Q_{12}s_{11} - Q_{11}s_{12})U_1 + (Q_{11}s_{11} - Q_{12}s_{12})U_2}{(s_{11} - s_{12})(s_{11} + s_{12})} - \frac{Q_{12}s_{11} - Q_{11}s_{12}}{s_{11} + s_{12}}\sigma_3,$$
$$a_3^* = a_1 - \frac{Q_{12}}{s_{11} + s_{12}}(U_1 + U_2) - (Q_{11} - \frac{2s_{12}}{s_{11} + s_{12}}Q_{12})\sigma_3,$$
$$a_{11}^* = a_{11} + \frac{(Q_{11} + Q_{12})^2}{4(s_{11} + s_{12})} + \frac{(Q_{11} - Q_{12})^2}{4(s_{11} - s_{12})},$$
$$a_{33}^* = a_{11} + \frac{Q_{12}^2}{s_{11} + s_{12}},$$
$$a_{12}^* = a_{12} + \frac{(Q_{11} + Q_{12})^2}{2(s_{11} + s_{12})} - \frac{(Q_{11} - Q_{12})^2}{2(s_{11} - s_{12})} + \frac{Q_{44}^2}{2s_{44}},$$
$$a_{13}^* = a_{12} + \frac{Q_{12}(Q_{11} + Q_{12})}{s_{11} + s_{12}}$$

4.4.3 G including biaxial and hydrostatic strains

By substituting the expression for σ_3 in terms of U_{xy} and U_z described in Eq. [4.3], then replacing U_{xy} and U_z with U_{bi} and U_{hyd} as given in Eq. [4.9], in addition to the boundary conditions ($U_1 = U_2 = U_{xy}$, $U_6 = 0$, and $\sigma_4 = \sigma_5 = 0$), the resulting form of $\breve{G}$ is given in Eq. [4.17]. It is easy to see that the presence of the strain renormalizes the Curie-Weiss temperature. Note that while the second order coefficients (α_i^*) in $\breve{G}$

reduces to those of G when U_{bi}=0, the forth order coefficients $(\alpha_{ij}{}^{*})$ behaves in a different way. This is because $\check{G}$ and G behave differently even there is no strain. That is, films mechanically constrained on a substrate show different behavior from the corresponding bulk materials.

$$\bar{G} = a_1^*\left(P_1^2 + P_2^2\right) + a_3^* P_3^2 + a_{11}^*(P_1^4 + P_2^4) + a_{33}^* P_3^4 + a_{12}^* P_1^2 P_2^2 + a_{13}^*\left(P_1^2 P_3^2 + P_2^2 P_3^2\right)$$
$$+ a_{111}\left(P_1^6 + P_2^6 + P_3^6\right) + a_{112}\left[P_1^4\left(P_2^2 + P_3^2\right) + P_3^4\left(P_1^2 + P_2^2\right) + P_2^4\left(P_1^2 + P_3^2\right)\right] \qquad (4.17)$$
$$a_{123} P_1^2 P_3^2 P_2^2 + \frac{U_{bi}^2}{s_{11} + s_{12}} + \frac{2 U_{bi} U_{hyd}}{s_{11} + s_{12}} + \frac{U_{hyd}^2}{2(s_{11} + s_{12})}$$

$$a_1^* = a_1 - \frac{Q_{11} + Q_{12}}{s_{11} + s_{12}} U_{bi} - \frac{Q_{11} + 2Q_{12}}{s_{11} + 2s_{12}} U_{hyd},$$

$$a_3^* = a_1 - \frac{2Q_{12}}{s_{11} + s_{12}} U_{bi} - \frac{Q_{11} + 2Q_{12}}{s_{11} + 2s_{12}} U_{hyd},$$

$$a_{11}^* = a_{11} + \frac{(Q_{11} + Q_{12})^2}{4(s_{11} + s_{12})} + \frac{(Q_{11} - Q_{12})^2}{4(s_{11} - s_{12})}, a_{33}^* = a_{11} + \frac{Q_{12}^2}{s_{11} + s_{12}},$$

$$a_{12}^* = a_{12} + \frac{(Q_{11} + Q_{12})^2}{2(s_{11} + s_{12})} - \frac{(Q_{11} - Q_{12})^2}{2(s_{11} - s_{12})} + \frac{Q_{44}^2}{2s_{44}}, a_{13}^* = a_{12} + \frac{Q_{12}(Q_{11} + Q_{12})}{s_{11} + s_{12}}$$

4.5 Curie temperature as a function of strain in BST

Before we study the strain effect on the Curie temperature of BST films with both hydrostatic and biaxial strain, we first briefly review the literature reported by [N. A. Pertsev, 1998], where they demonstrated the temperature-strain phase diagrams for BaTiO$_3$ and PbTiO$_3$ films grown on cubic substrate with only biaxial strain. The transition takes place at temperature T_c=max [T_1, T_3], T_3 and T_1 being the temperatures at which the paraelectric phase lose its stability with respect to the appearance of P_3 and P_1=P_2. Setting $\alpha_1{}^*$=$\alpha_3{}^*$=0 for the case of without hydrostatic strain. With the aid of Eqs [4.17], we find

$$T_3 = T_0 + 2C\varepsilon_0 \frac{2Q_{12}}{s_{11} + s_{12}} u_{bi}$$

$$T_1 = T_0 + 2C\varepsilon_0 \frac{Q_{11} + Q_{12}}{s_{11} + s_{12}} u_{bi},$$

(4.18)

where C and ε_0 are the Curie-Weiss constant and the dielectric susceptibility of the vacuum. As shown in Figure 4.5, regardless of the difference between the phase diagrams for BaTiO$_3$ and PbTiO$_3$, it is evident that the transition is of second-order, while the corresponding bulk transitions is of first-order since the coefficient α_{11}^*, α_{33}^* are positive. Moreover, the transition temperature should linearly depend on strain and should increase with the magnitude of biaxial strain, no matter it is compressive and tensile.
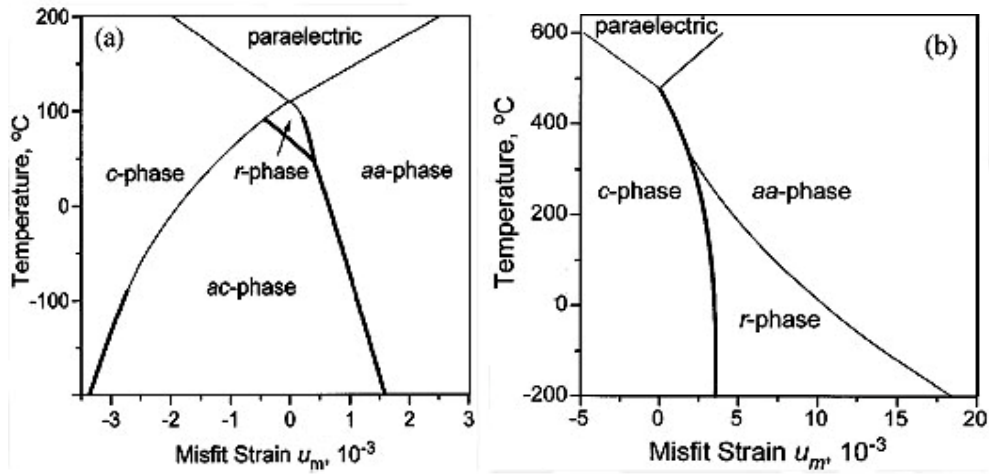
Fig. 4.5   Phase diagrams of (001) single-domain BaTiO$_3$ (a) and PbTiO$_3$ (b) thin films epitaxially grown on cubic substrates.

In the above, the dependence of the transition temperature on the biaxial strain for BaTiO$_3$ and PbTiO$_3$ has been demonstrated. Next, the influence of hydrostatic strain will be considered simultaneously for our BST thin films which have the combined contributions of both hydrostatic and biaxial strain. Setting $\alpha_1^* = \alpha_3^* = 0$,

with the aids of Eqs [4.17], transition temperatures for BST films are given as

$$T_3 = \theta + 2C\varepsilon_0 \left(\frac{2Q_{12}}{s_{11} + s_{12}} U_{bi} + \frac{Q_{11} + 2Q_{12}}{s_{11} + 2s_{12}} U_{hyd} \right),$$

$$T_1 = \theta + 2C\varepsilon_0 \left(\frac{Q_{11} + Q_{12}}{s_{11} + s_{12}} U_{bi} + \frac{Q_{11} + 2Q_{12}}{s_{11} + 2s_{12}} U_{hyd} \right),$$

(4.19)

where $Q_{11} = 0.1$ m^4/C^2, $Q_{12} = -0.035$ m^4/C^2, such that $Q_{11} + Q_{12} > Q_{11} + 2 Q_{12} > 0$, as is also the case for S_{ij} values. From Eq. [4.19], we can observe the hydrostatic strain has the same effect on both transition temperatures. As shown in the hydrostatic strain dependence on the thickness, below 150 nm, the sign of the hydrostatic strain is negative and the magnitude is decrease with increasing of thickness. Therefore, the transition temperature will increase as the thickness increases according to the Eqs [4.19]. Above 150 nm, the sign of the hydrostatic strain is positive and the magnitude increases with the increasing of thickness. Thus, the transition temperature will correspondingly increase with the thickness. On case of the biaxial strain, the transition temperature should linearly depend on strain and increase with the magnitude of biaxial strain, no matter compressive and tensile. According the experimental result shown in Chapter 3, the magnitude of biaxial strain always increases with the thickness. Therefore, the combined contributions of hydrostatic and biaxial strain lead to the linearly increase of transition temperature with the increasing of film thickness, which is in good agreement with our experimental results as described in Chapter 3.

4.6 Dielectric constant-strain relationship for BST films with different thickness

4.6.1 Calculation of $\varepsilon_{ij}/\varepsilon_0$ from $\check{G}$

We have already calculated the Curie temperature-strain relationship, now we move on to the dielectric response. The dielectric constant is a tensor defined as $\varepsilon_{ij}/\varepsilon_0 = 1 + \chi_{ij}$, where χ_{ij} is the dielectric susceptibility. The inverse dielectric susceptibility is the partial derivation of the electric field with respect to the polarization [A. P. Levanyuk, 1998].

$$\left(\varepsilon_0 \chi_{ij}\right)^{-1} = \frac{\partial E_j}{\partial P_i} = \frac{\partial^2 \bar{G}}{\partial P_i \partial P_j} \tag{4.20}$$

However, this gives the dielectric constant as a function of polarization. Actually, we need it in terms of electric field. According to the equation of state described in Eq.[4.13] and the explicit form of $\check{G}$ in Eq. [4.17], we can calculate electric field as function of polarization.

$$E_1 = \frac{\partial \bar{G}}{\partial P_1} = P_1\left(2a_1^* + 2a_{13}^* + 2a_{12}^* P_2^2\right) + 4a_{11}^* P_1^3,$$

$$E_2 = \frac{\partial \bar{G}}{\partial P_2} = P_2\left(2a_1^* + 2a_{13}^* P_3^2 + 2a_{12}^* P_1^2\right) + 4a_{11}^* P_2^3, \tag{4.21}$$

$$E_3 = \frac{\partial \bar{G}}{\partial P_3} = P_3\left(2a_3^* + 2a_{13}^*[P_1^2 + P_2^2]\right) + 4a_{33}^* P_3^3\Big),$$

where we have determined the expansion of $\check{G}$ at the fourth order in P for simplicity. This simplification is valid since the phase transition for the films is of second order. Terms of sixth order in P are necessary to describe a first-order transition [S. K.

Streiffer, 1999; F.Jona, 1962; M.E. Line, 1977].

The above equations give three dependent equations involving three variables. In practice, it seems impossible to calculate the P_1, P_2, and P_3. Therefore, further approximations are need. Firstly, we suppose the applied field has only one component (either E_1 or E_3) even though normally the coplanar electrode produces not only in-plane component but also out-of-plane one [S. S. Gevorgian, 1996]. In this way, the relationship between E and P is demonstrated as following

$$E_i = 2a_i^* P_i + 4a_{ii}^* P_i^3, i = 1,3, \tag{4.22}$$

Using the above equation, the P can be solved.

$$P_i = [\frac{E_i}{8a_{ii}^*} + \sqrt{\left(\frac{E_i}{8a_{ii}^*}\right)^2 + \left(\frac{a_i^*}{6a_{ii}^*}\right)^3}]^{1/3} + [\frac{E_i}{8a_{ii}^*} - \sqrt{\left(\frac{E_i}{8a_{ii}^*}\right)^2 + \left(\frac{a_i^*}{6a_{ii}^*}\right)^3}]^{1/3} \tag{4.23}$$

where i=1. 3. By inserting P to the Eq. [4.20], the relative dielectric constant can be calculated.

$$\frac{\varepsilon_{ii}}{\varepsilon_0} = 1 + \frac{1/(3a_{ii}^* \varepsilon_0)}{\left[\frac{E_i}{a_{ii}^*} + \sqrt{\left(\frac{E_i}{a_{ii}^*}\right)^2 + \left(\frac{2a_i^*}{3a_{ii}^*}\right)^3}\right]^{2/3} + \left[\frac{E_i}{a_{ii}^*} - \sqrt{\left(\frac{E_i}{a_{ii}^*}\right)^2 + \left(\frac{2a_i^*}{3a_{ii}^*}\right)^3}\right]^{2/3} - \frac{2a_i^*}{3a_{ii}^*}} \tag{4.24}$$

As shown in this equation, it is obvious that the dielectric constant is associated with the electric field. Because the dielectric stiffness constants α_i^*, α_{ii}^* are related to temperature and strain as given by Eq. [4.17], the relative dielectric constant correspondingly depends on temperature and strain.

4.6.2 Zero-field dielectric constants at room temperature of BST films with different thickness

To investigate thickness dependence of zero-field dielectric constant of BST films as discussed in Chapter 3, we replace E_i with $E=0$ in Eq.[4.24] Then,

$$\varepsilon_{ii}/\varepsilon_0 = 1 + (2\varepsilon_0 \alpha_i^*)^{-1} \ , \ i=1,3 \tag{4.25}$$

All the calculations presented in the following section are made for ε_{11}. The dependence for ε_{33} is qualitatively similar except that the temperature shifts due to biaxial strain for ε_{11} are in the opposite trend. Thus,

$$\varepsilon_{11}/\varepsilon_0 = 1 + (2\varepsilon_0 \alpha_1^*)^{-1}$$

$$a_1^* = a_1 - \frac{Q_{11} + Q_{12}}{s_{11} + s_{12}} U_{bi} - \frac{Q_{11} + 2Q_{12}}{s_{11} + 2s_{12}} U_{hyd} \tag{4.26}$$

$$a_1 = \frac{T - \theta}{2\varepsilon_0 C}$$

Here we assume value of Curie constant C as 1.9×10^5 K [C. M. Carlson, 2000] at room temperature. θ is the Curie-Weiss temperature. Due to the second-order transition, the Curie-Weiss temperature is equal to Curie point. As shown in Chapter 3, T_c exhibits dependence on the thickness. The relationships between hydrostatic and biaxial strain and thickness have already described in Chapter 3. By the above known parameters, we calculated α_1^* as shown in Figure 4.6. Then, the relative dielectric constant can be obtained by Eqs [4.26]. Figure 4.7 shows the thickness dependence of normalized relative dielectric constant calculated from Eqs [4.26]. The value of dielectric constant of the films increases with increasing film thickness. The curve predicted by theory and the experimental curve are extremely alike

although there exists a large difference for the corresponding value.
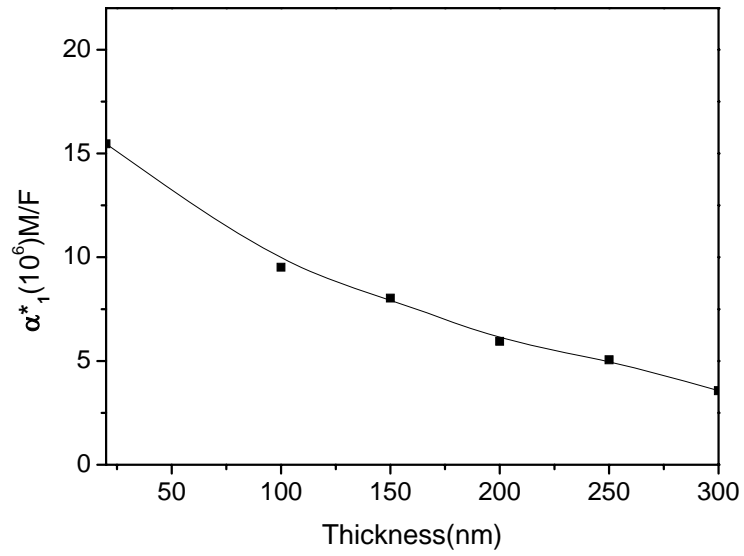
Fig. 4.6   The thickness dependence of the dielectric stiffness constants α_1^*.
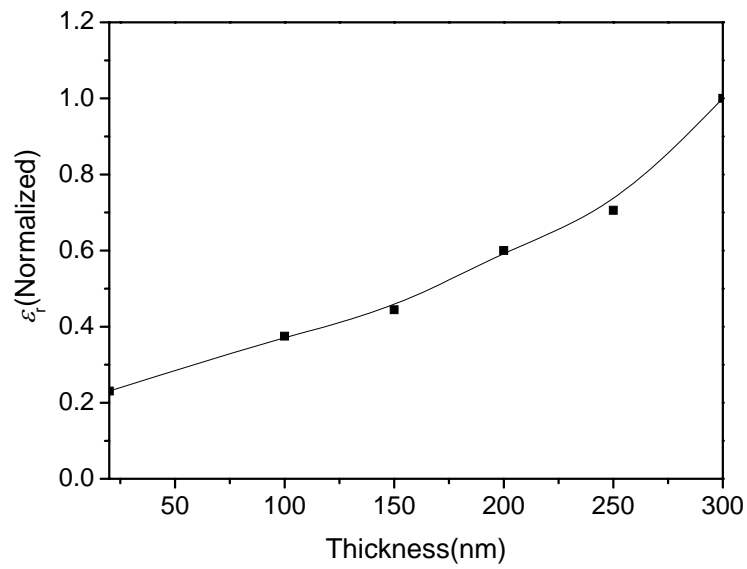
Fig. 4.7   The thickness dependence of normalized dielectric constant.

4.6.3 Dielectric properties of BST films under electric field

For application in frequency agile microwave electronic components the dependence of dielectric constant on electric field (tunability) is a very important issue. Eq.[4.26] only calculates the dielectric constant at zero field and does not show how the dielectric constant changes with electric field and ultimately, the relationship between strain and tunability. The effect of electric field on dielectric constant (ε_{11}) can be solved by Eq.[4.24]. α_I^* has been already calculated, and α^*_{11} is given as [C. M. Carlson, 2000]

$$a_{11}^* = a_{11} + \frac{(Q_{11} + Q_{12})^2}{4(s_{11} + s_{12})} + \frac{(Q_{11} - Q_{12})^2}{4(s_{11} - s_{12})} \tag{4.25}$$

α_{11} is a positive value due to the second order transition and assumed as 4×10^6 (m^5/FC^2K). According to Eq.[4.25], the value of α^*_{11} can be obtained and then inserted to Eq.[4.24]. Unlike α_I^*, which is dependent on the thickness, α^*_{11} has no dependence on strain, and can be considered as a fixed value for different thickness. Additionally, we proposed electric field ranging from -5×10^7 V/m to 5×10^7 V/m based on the experimental situations. The fitted curve at thickness of 200 nm was demonstrated in Figure 4.7. As found in Figure 4.7, (1) the main effect of an applied electric field is to suppress the magnitude of the dielectric response, which is in good agreement with our experimental results; (2) there are still some discrepancies between our calculations and the experimental data due to the simplification of our model. The tunability almost amounts to 90%.
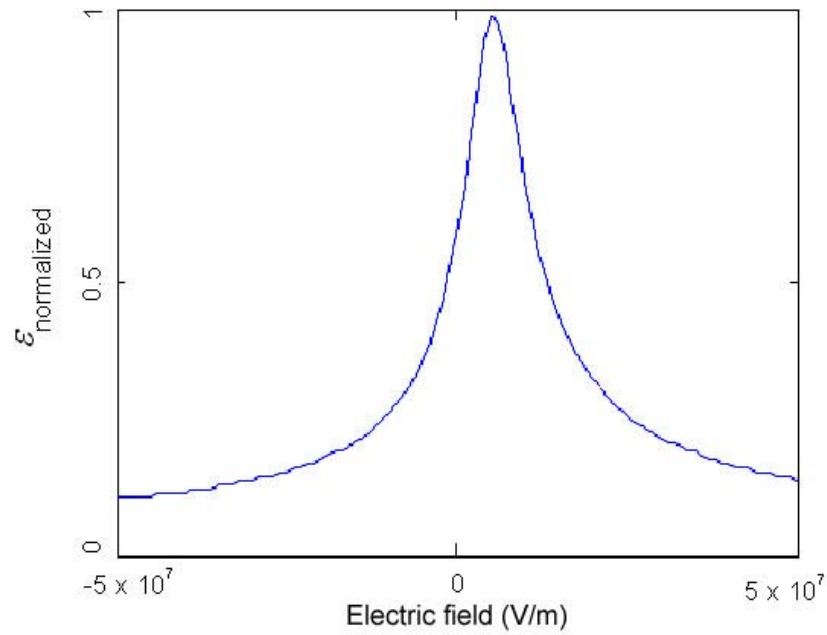
Fig. 4.8   Fitted curve of dielectric constant as function of electric field for BST thin films at thickness of 200 nm.

4.7 Summary

In this chapter, theoretical analysis by phenomenological method has been carried out to study the strain effect on the in-plain dielectric properties of BST thin films with different thickness. By grouping the strain into biaxial (2-dimensional) and hydrostatic (3-dimensional) components which can be calculated from the XRD results, using the Landau-Ginsburg-Devonshire formalism and performing mathmatical calculations from the elastic Gibbs free energy, we found our theoretical results is coincident with the experimental observation. The transition temperature (Curie temperature) and dielectric constant decrease with the decreasing of film thickness associated with a decreasing of dielectric constant with the electric field.

Deposition of STO/BST

thin films on silicon wafers

5.1 Introduction

Perovskite oxides are an amazing family of materials that share a common crystal structure (i.e., a structure analogue to that of the natural crystal $CaTiO_3$) but exhibit a broad range of interesting physical properties (e.g., $LaAlO_3$ – insulation, $PbZrTiO_3$ – piezoelectricity, $BaTiO_3$ – ferroelectricity, YBCO – superconductivity, $LaSrMnO_3$ – colossal magnetoresistance, etc). By combining perovskite oxide thin films with different properties, it is possible to develop novel all-perovskite-oxide micro/nano-devices (e.g., all-perovskite ferroelectric field effect transistor, p-n junction, fuel cell, ferroelectric memory, microwave devices and MEMs) [Y. Watanabe 1995; J. Zhang, 2002; M. F. Hsu, 2006; R. Ramesh, 1992; S. S. Gevorgian, 1997]. In order to obtain the best properties and performance in such devices, it is usually desirable that all layers maintain an epitaxial relationship, which can be achieved by growing the thin films on single crystal substrates (e.g., $SrTiO_3$ is one of the most popularly used substrates). Such heterostructures, however, are usually too expensive for commercial applications. To grow them on silicon wafers can certainly lead to a dramatic reduction in cost. However, the direct growth of perovskites on Si or platinized silicon ($Pt/Ti/SiO_2/Si$) is technically not a good choice because the films

grown on such wafers often have low crystalline quality and poor physical properties.

The recently developed SrTiO$_3$/Si wafer seems to have provided a solution to the above problem. STO has a perovskite crystal structure with lattice constant $a_0 =$ 3.905 Å. In the STO/Si heterostructure, the ultra-thin but epitaxially aligned SrTiO$_3$ film functions as a template for the epitaxial growth of subsequent perovskite oxide layers while the Si substrate guarantees good processing compatibility with the mature silicon technology (hence a lower cost for the whole structure) [Y. Wang, 2002; G. Y. Yang, 2002]. It is interesting to note that, although originally the development of the SrTiO$_3$/Si heterostructure was mainly motivated by the potential use of SrTiO$_3$ as a high-*k* material, the present research has actually been focusing on the use of the SrTiO$_3$/Si as substrates for all-perovskite oxide devices. The heterostructure of BST/STO/high-R silicon for tunable microwave devices is one good example. Potentially this structure can replace the conventional heterostructure of BST/single crystal provided: (1) BST thin films in both structures are of the same quality and (2) The electrical resistivity of silicon is high enough. Recently there are theoretical work on the influence of silicon resistivity on the performance of the device. It is concluded that silicon with a resistivity larger than 3000 Ω.cm will be good enough for making microwave devices with a working frequency around several GHz [B. Rong, 2004; S. Gevorgian, 1998].

Good crystallinity, epitaxial alignment and clean interface are the major requirements for the SrTiO$_3$/Si heterostructure. To achieve this goal is technically difficult mainly because silicon is readily oxidized even in vacuum and the formed amorphous silicon oxide significantly influences the crystallization and growth of the

SrTiO$_3$ film. In the literature, the problem is solved by (1) conducting the deposition in a high vacuum environment and (2) using strontium as a buffer layer before SrTiO$_3$ is deposited. High quality SrTiO$_3$ films have been developed by molecular beam epitaxy (MBE) [H. Mori, 1991; B. K. Moon, 1991; B. K. Moon, H. Ishiwara, 1994; R. A. Mckee, 1991; R. A. Mckee, F. J. Walker, 1993; R. A. Mckee, F. J. Walker, M. F. Chisholm, 1998; Z. Yu, 1999; Z. Yu, J. Ramdani, 2000]. Theoretical works have also been conducted to investigate the growth mechanism of SrTiO$_3$ and the energy states of the SrTiO$_3$/Si structure. Some silicon based perovskite-oxide heterostructures and prototype devices have also been developed [Z. Yu, 2004; K. Eisenbeiser, 2000; C. H. Ahn, 2004; R. A. McKee, 1998; R. A. McKee, F. J. Walker, 2001; J. Lettieri, 2002; M. N. K. Bhuiyan, 2005; M. N. K. Bhuiyan 2005; J. Robertson, 2000].

Because MBE is a high-cost technique, there is a need to explore the use of less expensive method to integrate SrTiO$_3$ with Si. In the literature, there are attempts to develop SrTiO$_3$/Si by using pulsed laser deposition (PLD) [F. Sanchez, 1992; F. Sanchez, R. Aguiar, 1998; O. Nakagawara, 1995] or e-beam deposition [H. Mori, 1991; B. K. Moon, 1991; B. K. Moon, H. Ishiwara, 1994] techniques.

In this chapter we report our work on the integration of SrTiO$_3$ thin films on Si by means of the laser molecular beam epitaxy (laser MBE). We choose to use laser MBE technique because: (1) It is much less expensive than conventional MBE procedure; (2) The laser-MBE technique is analogous to many other physical vapor depositions (PVD) such as sputtering and PLD. Therefore the processing – structure relationship that we obtain in the research may be more applicable to other PVD processes; and (3) In a laser-MBE system, a wide range of temperature, atmosphere

and ultrahigh vacuum environment is available, making it convenient to achieve the optimized condition for the growth of high quality SrTiO$_3$ thin films. The possible disadvantage of this technique, however, is that the use of a ceramic target may make it more difficult to obtain a clean interface between STO and Si. This is because the plume (generated by the irradiation of the ceramic surface by a pulsed laser beam) may contain oxygen atoms which can react with silicon, leading to the formation of an amorphous silicon oxide layer on the substrate surface. Thus how to suppress or prevent the oxidizing reactions is the major problem to be tackled in this work.

5.2 Thin film integration and characterization

5.2.1 Thin film deposition by laser-MBE

The technique of laser molecular beam epitaxy (laser-MBE) was employed in thin film deposition. Figure 5.1 shows the laser-MBE system in our laboratory. The basic features of the system include: (1) Pre-loading chamber, (2) Ultra-high vacuum (UHV) chamber; (3) RHEED; (4) Rotating target and substrate holder.

The deposition was conducted via a three-step procedure: 1) Wet-cleaning: A (001) Si wafer was treated by standard chemical cleaning procedures followed by HF etching. The freshly cleaned wafer, together with two targets (high-purity Sr and SrTiO$_3$), were then installed in the vacuum chamber of the laser-MBE system. After the target installation, the chamber was immediately evacuated by using a mechanical pump and a molecular turbo pump. 2) Dry-cleaning: When the pressure in the chamber was lower than 1×10^{-6} Torr, the Si wafer was heated up to 850 °C and kept at this temperature for 15 mins, with the aim of removing the residual hydrogen

on the Si surface. Then the temperature was lowered to a temperature T_d and a very thin layer of strontium was deposited by irradiating the Sr target with a pulsed KrF excimer laser beam. This step aimed to remove the SiO_2 layer that had been freshly formed during the processing [M. N. K. Bhuiyan, 2005; B. K. Moon, 1994]. 3) Deposition: Following the deposition of the Sr layer, a STO layer was deposited using the same laser. Initially a relatively low substrate temperature (~650 °C) and low oxygen pressure (0.02 Pa) were used, while at a later stage the temperature and oxygen pressure were increased to ~800 °C and 50 Pa, respectively.
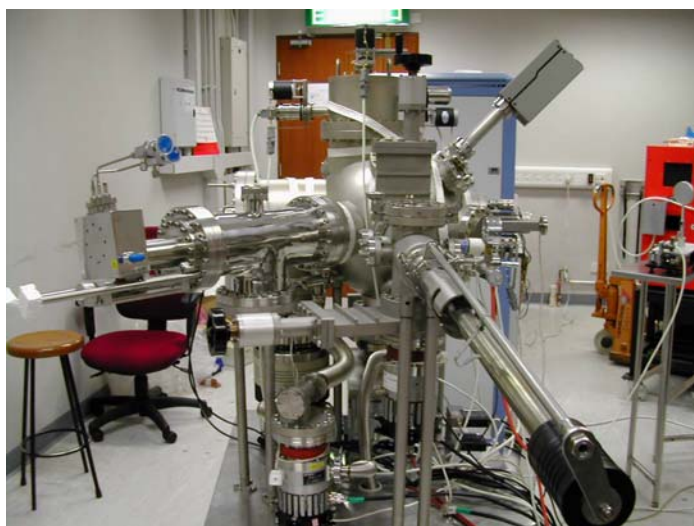
Fig. 5.1   The laser-MBE system for thin film deposition.

5.2.2 Structural characterizations

A number of techniques were employed to characterize the heterostructure $SrTiO_3$/Si. They include:

1) Atomic force microscopy. The surface morphology of the STO thin film was observed in an atomic force microscope (AFM, Digital Instrument Nanoscope IV) working in the tapping mode.

2) X-ray diffraction (XRD). The crystallographic characterization was performed on a Bede D1 scientific diffractometer (namely, a four-circle goniometer) with a high-precision MRD-cradle (angle coordinates are ω、φ and χ) and a EDRc scintillation detector, using a graphite monochromator and Cu Kα radiation. X-ray diffraction techniques such as symmetric (*2θ/θ* scans, *ω/2θ* scans, *ω* scan, and pole figure) and asymmetric (*2θ-ω*) geometries were carried out to determine the structure.

3) X-ray reflection (XRR). XRR scans were also performed using an X-ray tube current of 40 mA and a voltage of 50 kV. The incident beam was confined by a 0.1 mm slit, and the scattered beam was confined by a 0.1 mm slit at the detector stage and 0.1 mm slit before the detector stage. The intensities of the reflected X-ray beams at different angles were collected in seconds by a multichannel detector. In order to measure the angles accurately and to minimize the experimental error, the rotational axis of sample circle (ω circle) was aligned exactly by rocking the samples at a fixed 2θ. Thus, XRR measurements are only sensitive to vertical electron density contrast and therefore suitable to determine layer thicknesses as well as surface and interface roughness.

4) High-resolution transmission electron microscopy (TEM). Details of the analysis will be given in the coming sections. A JEOL JEM-2011 transmission electron microscopy (TEM) operating at 200 kV was used to observe the crystal structure and interfaces at atomic level. The high resolution scanning transmission electron microscopy images were taken using a high angle annular dark field detector in a scanning transmission electron microscope (STEM, Tecnai G2 FEG). The Electron energy loss spectroscopy (EELS) measurements were performed in the STEM line

scan mode, using a Gatan Imaging Filtering system attached to the same microscope. The electron probe size was maintained at 0.3 nm.

5.3 Structure features of as-produced STO/Si

5.3.1 Processing optimization

The structure of the STO film and STO/Si interface were found to be very sensitive to the processing parameters, including deposition temperature, atmosphere and pressure, laser energy and pulse rate, and the thickness of the Sr template. This observation is consistent with literature reports [Z. Yu, 2004; J. Lettieri, 2002; M. N. K. Bhuiyan, 2005]. Among these parameters, however, the parameters that have the most critical influence is the thickness of the Sr template t_{Sr} and the deposition temperature for the Sr template T_d. Samples prepared under optimized processing conditions ($T_d \approx 650 \pm 50°C$ and $t_{Sr} \approx 1.2 \pm 0.4$ nm) tend to be of high quality and have a sharp and clean (free of amorphous material) STO/Si interface, while samples prepared under conditions outside the above range either have a rough and saw-like interface (when the deposition temperature is too high and/or the Sr template is too thick) or a thick amorphous layer (when the deposition temperature is too low and/or the Sr template is too thin). This processing-structure relationship, we believe, is closely related to the reaction $SiO_2 \rightarrow Si + 2O$ and the role that Sr plays in the reaction. SiO_2 in the above chemical equation corresponds to the amorphous SiO_2 layer that forms on the fresh Si surface during its contact with air (i.e., in the time interval after the chemical cleaning and before the achievement of high vacuum in the chamber) and exposure to the plumb (in the first few seconds of STO deposition).

The rate of the decomposition of SiO_2 at high temperatures could be enhanced by the catalyst Sr, as suggested in the literature. It is reasonable to assume that, under optimized conditions, the SiO_2 layer could be completely removed, so the surface of the Si substrate would become very clean.

Figure 5.2 and 5.3 show two typical TEM images of samples with undesirable interfacial structures. Correspondingly the samples often exhibit poor crystalinity and a polycrystalline nature in XRD patterns (data not shown).
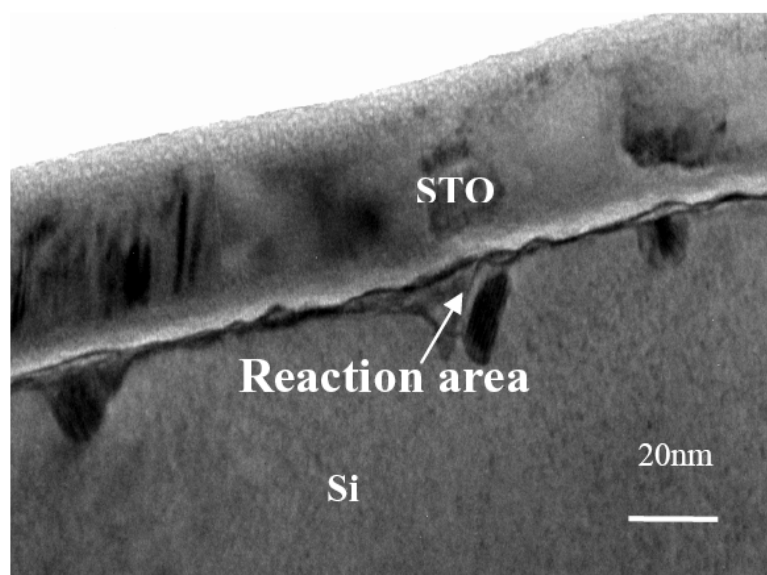
Fig. 5.2   STO/Si sample with an undesirable saw-like interface.
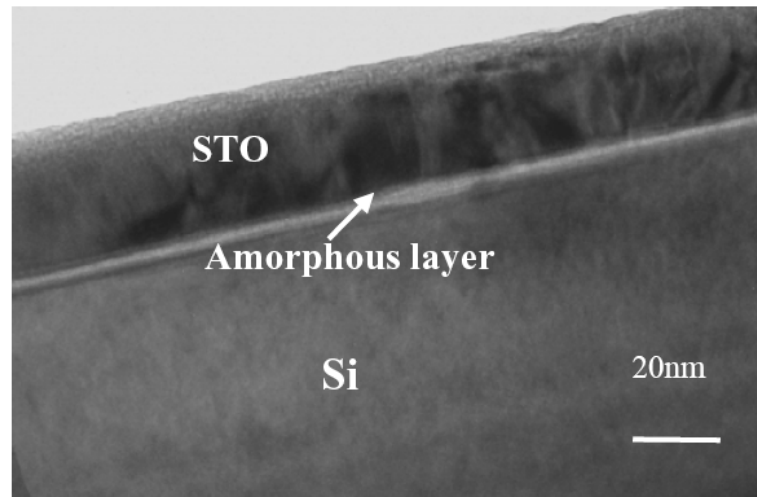
Fig. 5.3   STO/Si sample with an undesirable amorphous layer at the interface.

The optimized processing conditions are summarized as below:

1) Deposition of Sr layer: base vacuum = 10^{-5} Pa, substrate temperature = 650~700 °C, deposition pressure = vacuum, laser energy = 160-180 mJ and repetition rate = 1 Hz.

2) Deposition of STO: base vacuum = 10^{-5} Pa, substrate temperature = 650~700 °C, oxygen pressure = 1-5 Pa, laser energy = 220-250 mJ and repetition rate = 2 Hz.

3) Post-deposition annealing: 700 -750 °C, oxygen pressure = 30 -100 Pa.

5.3.2 Typical structure of STO/Si prepared under optimized conditions

STO/Si samples prepared under the optimized conditions are found to have the following structural features: (1) epitaxial alignment of STO on Si; (2) high crystallization quality of STO; (3) clear and sharp interface between STO and Si. While detailed structural information of a fabricated thin film is available only after a

series of post-deposition structural characterization experiments, an in-situ observation of the reflection high energy electron diffraction (RHEED) of the sample surfaces gives useful information for accessing the quality of the film under preparation.

Figure 5.4 demonstrates typical RHEED patterns obtained in the fabrication processes that usually led to the growth of high-quality STO thin films. Figure 5.4a is for the as-annealed Si substrate just before STO growth. The pattern reveals that the silicon surface is clean and atomically flat. Figure 5.4b is the RHEED pattern for an as-deposited STO film observed with the incident electron beam parallel to the (110) direction of Si. The streak-type pattern indicates that STO was epitaxially grown on Si and atomically smooth as well.
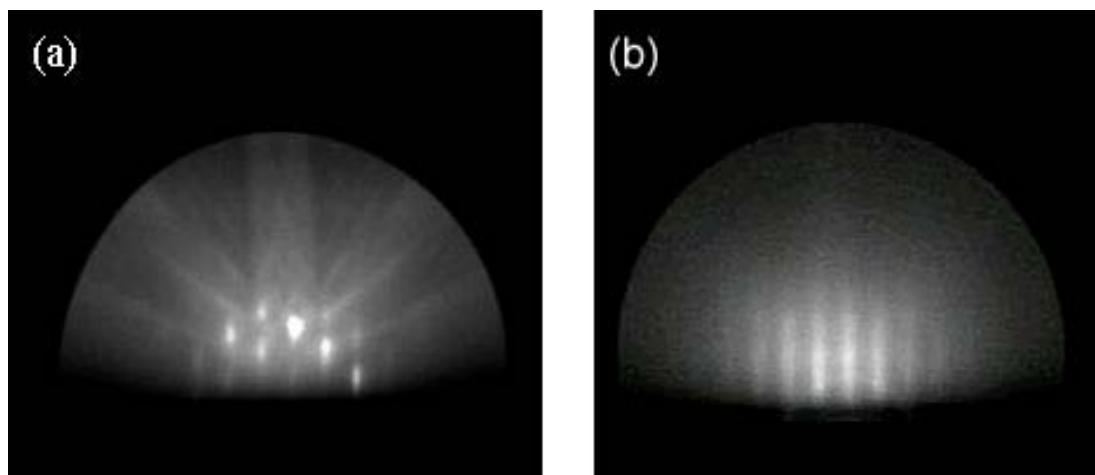
Fig. 5.4   Reflection high energy electron diffraction pattern for: (a) as annealed Si substrates just before STO growth and (b) as deposited STO films.

More detailed structural information about STO and the STO/Si interface is given below.

5.3.2.1 Surface morphology of STO observed on AFM

The surface morphology of the STO thin films was observed in a atomic force microscope. Figure 5.5 shows a typical AFM image of the sample. The scan area was 2×2 µm. The height of the Z-axis was 30 nm. The average grain size was estimated to be about 30-40 nm in diameter. The root-mean-square (RMS) roughness was about 1.02 nm, indicating a relatively smooth film surface, which is consistent with the above RHEED observation.
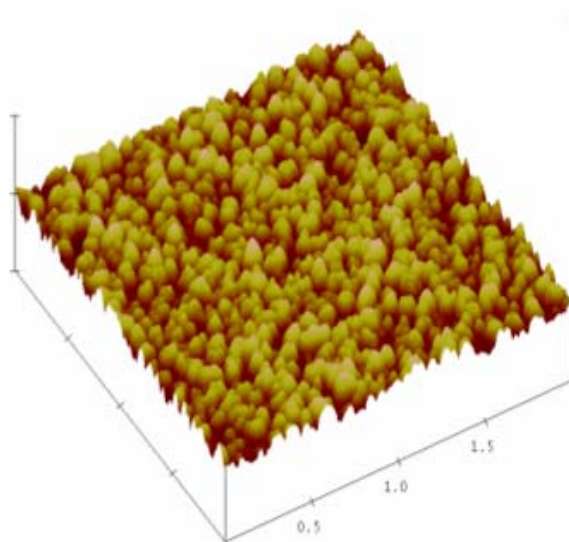
Fig. 5.5   Atomic force microscope image of the surface of a STO thin film grown on a Si substrate.

5.3.2.2 Quality of crystallization of STO (by XRD)

Figure 5.6 shows the X-ray diffraction (XRD) $\theta/2\theta$ scan of the sample. The STO thin film has a pure perovskite phase with a crystallites highly oriented along the (00l) direction. The in-plane alignment of the STO thin film with respect to the major axes of the (001) Si substrate was also investigated by XRD off-axis ϕ-scans and the results are shown in the inset of Figure 5.6. Based on the XRD data, it is

concluded that the crystal structures of STO and Si have the relationship of $(100)_{STO}//(100)_{Si}$ and $<100>_{STO}//<110>_{Si}$, which is consistent with results reported in the literature [G. Y. Yang, 2002; Y. Wang, 2002]. Both the in-plane and out-of-plane alignment were evaluated by ω-scan measurements taken around the STO (002) and (110) reflections. The full widths at half maximum (FWHM) were found to be ~0.306 ° and ~0.859° for the two ω-scan patterns, respectively. This result further confirms that the film exhibits high epitaxy.
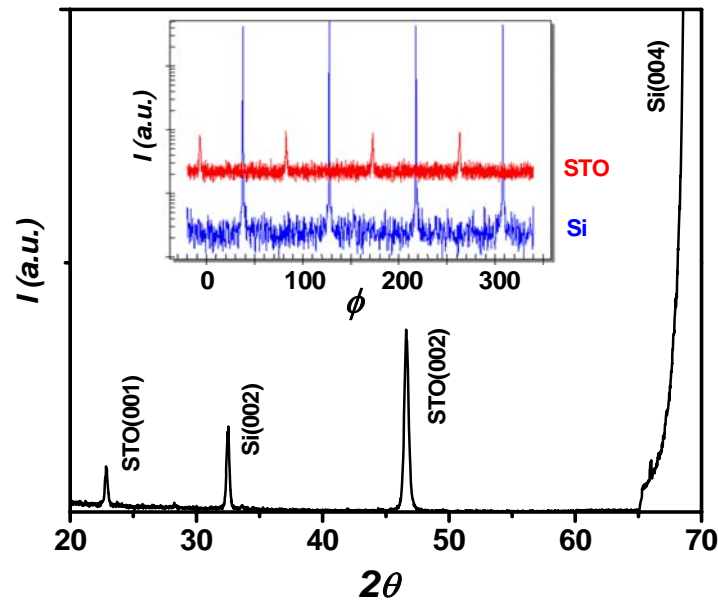
Fig. 5.6   X-ray diffraction patterns of STO/Si. The inset shows the offset φ-scan results of the sample.

X-ray pole figure is another helpful technique in the qualitative analysis of epitaxial film texture. Figure 5.7 shows the two dimensional (left) and three-dimensional (right) χ-φ scans for STO (110) reflection (i.e. step size is 1° for χ and 0.2° for φ). We obtain fourfold symmetrical concentrated poles corresponding to the STO (110) plane, which are located at φ values of 0 °, 90 °, 180 ° and 270 °.

The results are consistent with the *φ* scan.
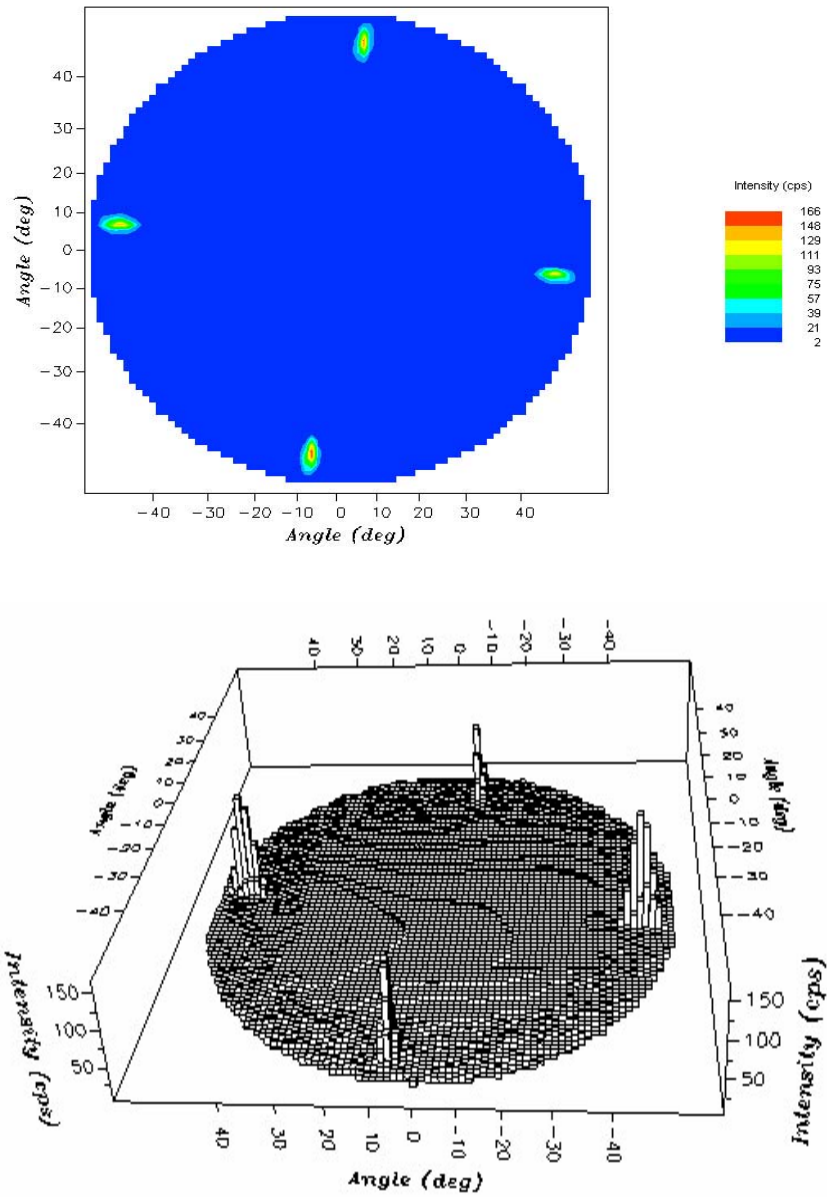
Fig. 5.7   Pole figure of STO (110) reflection respectively. top: two-dimensional

image, bottom: three-dimensional image.

The lattice parameters of STO have been determined using the asymmetrical

scan with aspect to the STO (202) plane and the symmetrical scan with aspect to the

STO (200) plane. The exact (200) and (202) peak positions were derived from the

Pseudo-Voigt function simulation. The out-of-plane lattice parameter ($c=2\,d_{002}$) and

the in-plane lattice parameter ($a = 2 / \sqrt{d_{202}^{-2} - d_{002}^{-2}}$) were found to be 0.3898 and 0.3902 nm, respectively. As compared with the cubic structure ($a = c = 0.3905$ nm) of STO bulk materials, the thin film has a slightly distorted lattice structure which is very likely due to the stress generated in the deposition process.

The relationship between the STO lattice and Si lattice is schematically shown in Figure 5.8.
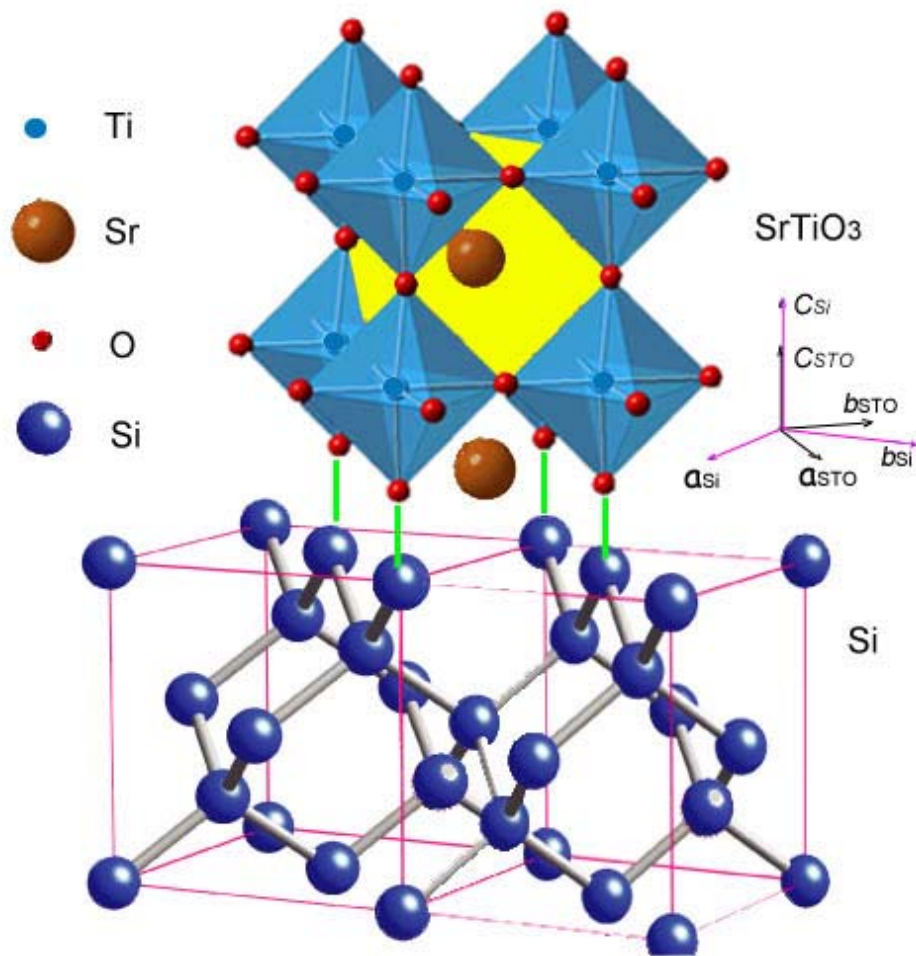
Fig. 5.8   Epitaxial relationship of STO lattice and Si lattice. There is a slight distortion in the STO lattice as compared with bulk material. There is a 45° rotation between the [100] direction of Si and [100] direction of STO.

5.3.2.3 Interfacial structure (by TEM & STEM)

Cross-sectional images of the STO/Si structures were observed in TEM. Figure 5.9 shows the interfacial structure of STO/Si (high resolution and conventional resolution images). Consistent with XRD results, the STO layer is well crystallized and epitaxially aligned. Between the STO and Si layers, a clean, sharp and fully crystallized interface layer was observed. The thickness of the interface layer is about 1.2 nm. No misfit dislocations were found at the interface, implying that there is only a slight elastic distortion in the STO lattice along the in-plane direction due to the lattice mismatch between the STO and Si layers (the lattice spacings along STO [100] and Si [110] are 0.390 and 0.385 nm, respectively, and the mismatch between them is ~1.4%).
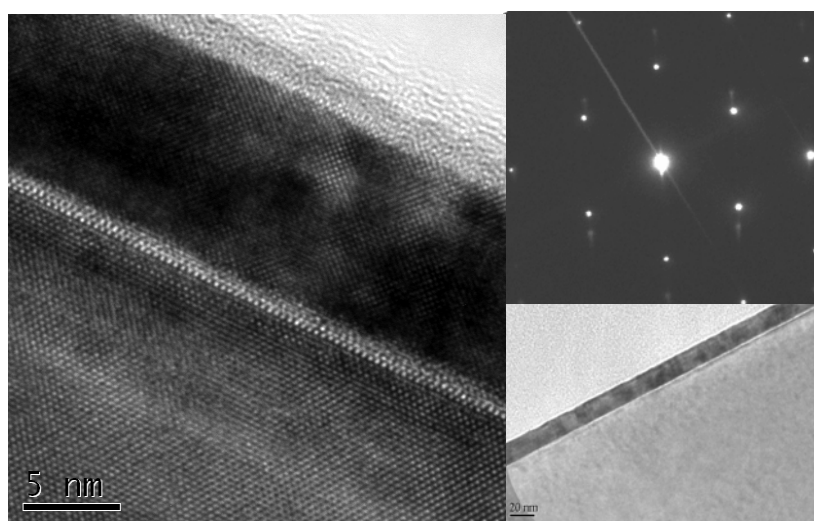
Fig. 5.9   High-resolution TEM image of STO/Si interface. STO is well crystallized and epitaxially aligned. The upper right insert shows selected area electron diffraction pattern taken at the interface and the other insert shows a low magnification image.

A more detailed microstructure of the STO/Si interface was disclosed by a high

resolution STEM equipped with an electron energy loss spectrum (EELS) system, as shown in Figure 5.10. A Sr-deficient layer with a thickness of 1-2 monolayers was found in-between the Si and the STO film. This observation suggests that strontium deposited in the step of dry-etching of the fabrication process had actually evaporated from Si. The EEL spectra taken at the Ti L edge from locations A, B, and C (as marked in the STEM image) reveal a valence decrease of the Ti, as the electron probe moves from the film interior to the interface. One can see that the EEL spectrum taken from location A has a double peak splitting feature, which is characteristic of the Ti^{4+}. The peak splitting disappears with peak center red shifting in the EEL spectrum taken from location B. This is the signature of Ti^{3+}. The double peak further shifts to lower energy at location C before the Ti signal completely vanishes, suggesting a further decrease in the Ti valence. The variation of Ti valance is obviously the result of the change of the atmosphere in the step of STO deposition. The results exclude firstly, the possible formation of interfacial SiO_2 layer when one should not obtain any signal from the Ti; and secondly, the existence of interfacial $TiSi_2$, when one should expect valence increase in Ti instead of decrease. Such interfacial configuration is different from the previous literature reports, and interesting enough, it also leads to epitaxial growth of STO on Si.
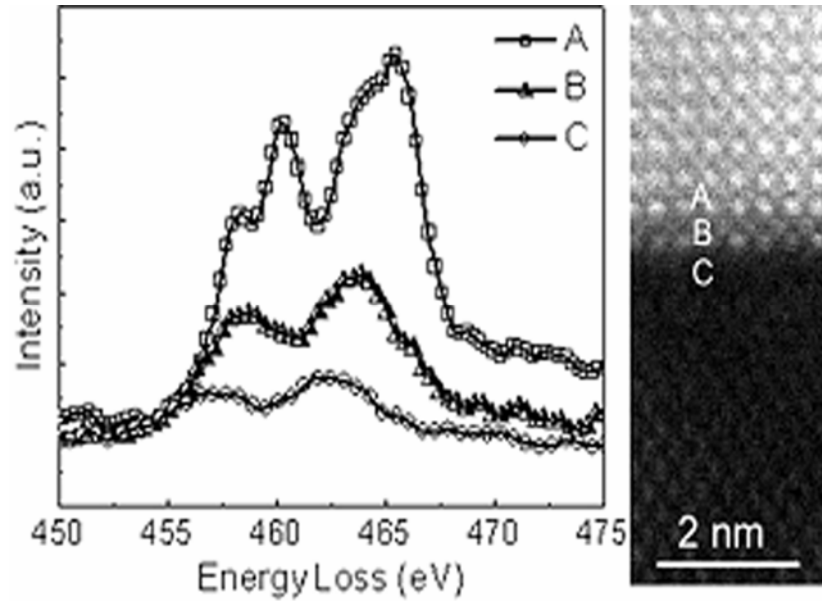
Fig. 5.10   Electron energy loss spectra taken at the Ti L edge from location A, B and

C, as indicated in the high resolution scanning transmission electron

microscopy image (right-hand side).

5.3.2.4 Structure characterization over large area (by XRR)

The quality of the thin film was further accessed by x-ray reflectivity (XRR) measurements. The XRR technique is a powerful complementary to locally probing microscope method like TEM, SEM, and AFM [R. A. Mckee, 1998; Z. Yu, J. Ramdani, 2000]. In our study, we use the XRR tests to purse structure information of the films, such as thickness, electron density, and roughness.

Figure 5.11 shows the X-ray reflectivity profiles of our STO/Si sample. The interference fringes of reflectivity curve of STO films exhibit prominent oscillations. Qualitatively, the fringes result from the interference among X-rays scattered by the electron density difference between substrate and film at the interface regime; the period of the fringes reflects the thickness of the films. This large oscillation

amplitude refers to obvious difference of electron density between the thin layer and the substrate. In addition to interference fringes (kiessig fringes), there also exists a critical angle at which total external reflection of the radiation takes place.
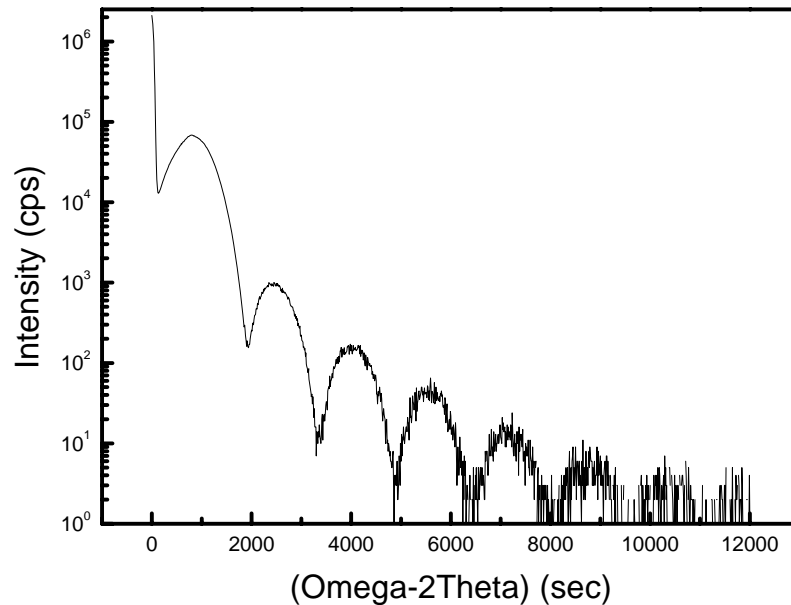
Fig. 5.11   X-ray reflectivity profile of the STO/Si sample.

Software simulation was conducted to pursue structural information of our samples using a software package, Bede REFS, offered by Bede company. The first step of the data treatment was to assume a layered structure of the sample. In the simulation, we assumed three possible structures: 1) STO/Si with a clear interface, 2) STO/Si with strontium silicate along the interface and 3) STO/Si with Sr along the interface. Based on dynamical diffraction theory, the software helped generate different intensity versus omega-2theta curves corresponding to different structure types. In our case, we found that only the curve generated based on the first structure fit well with the experimental data, as shown in Figure 5.12, while the other two gave poor consistency. This result suggests that there is a clear interface in the STO/Si

sample, which is in good agreement with the TEM observations.
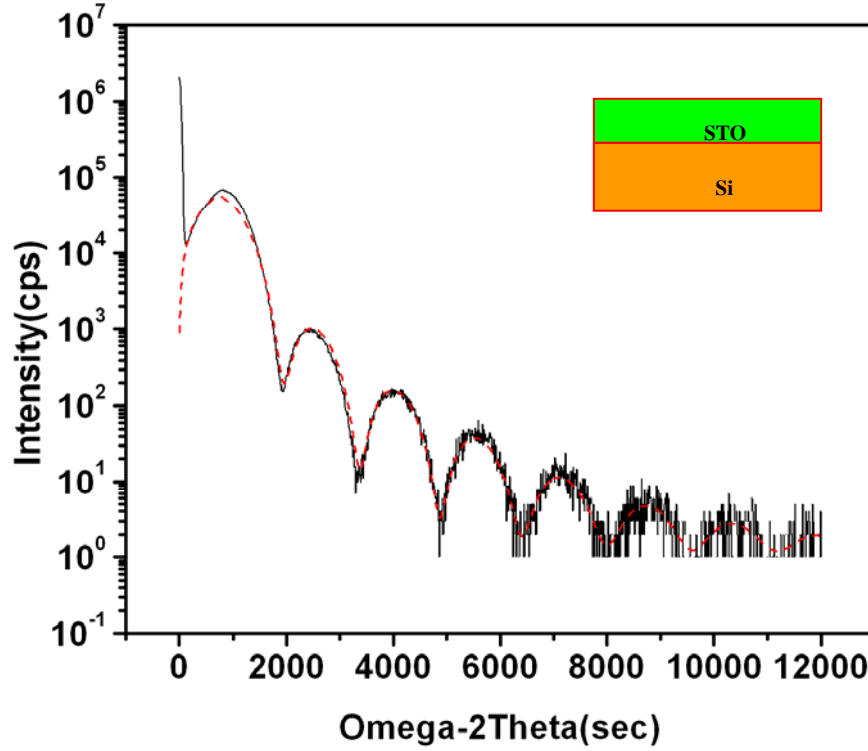
Fig. 5.12 X-ray reflectivity profile of the STO/Si sample. The black curve is the experimental result and the red line is the software simulation result corresponding to STO/Si layered structure.

More structural information was obtained by analyzing the XRR data. From the interference oscillations observed in the reflectivity profile, for example, the thickness of STO layer, , where λ is the wave length of X-ray, θ_{i+1} and θ_i are the angles of the $(i+1)^{\text{th}}$ and i^{th} peaks of the oscillations, respectively. Details of the STO/Si structure are given in Table 5.1.

Table 5.1　　Structural information of the STO/Si sample by XRR analysis

	Thickness (nm)	Roughness (Å)
STO films	10.48	2.09
Si substrates	∞	2.00

The thickness uniformity of the STO thin film was examined through XRR measurements conducted at different PHI angles by rotating samples around the surface normal. The profiles (data not shown) obtained at four different angles (Phi = 0, 90, 180 and 270°, respectively) were found to be analog to each other with negligible intensity differences. This suggests that the STO film is very uniform over a relatively large area.

5.4 Electrical characterization of the STO/Si sample

The electrical properties of STO and the STO/Si heterostructure were characterized. For convenience of measurements, the silicon substrate used for this purpose was conventional n-type silicon rather than high-resistivity one. Gold (Au) electrode was formed on top of the films by subsequent sputtering Au at room temperature with a shadow mask of 0.20 mm^2. The so-formed MOS capacitors were evaluated by I–V measurement performed with Advantest TR8652 Digital Electrometer. C-V measurement was carried out by HP 4291 impedance analyzer. An equivalent oxide thickness t_{eq} can be defined for a MOS capacitor as $t_{eq} = \varepsilon_0 \varepsilon_{SiO2} /(C/A)_{ox}$ [C. Y. Hu, 1995], .in which ε_{SiO2} and ε_0 are the dielectric constants of silica and the permittivity of free space. C/A_{ox} is the specific capacitance of the MOS

capacitor.

Figure 5.13 shows specific capacitance against voltage for a 150-Å-thick film of $SrTiO_3$ on (001) Si. The capacitor exhibits a C/A value of about 1.2×10^{-3} pF/um^2 under a voltage of -2 V. Based on the above analysis, we verified that the measured STO capacitor has a capacitance effective oxide thickness of less than 18 Å. If we subtract the known 2-3 Å for charge quantum confinement effect at the oxide Si interface [C. Y. Hu, 1995], we can estimate that the 150 Å $SrTiO_3$ behaves comparably to a 16 Å SiO_2 gate insulator. The interface trap density was estimated using a method proposed by Terman [L. M. Terman, 1962]. By comparing the theoretical C–V curve for a 16 Å SiO_2 gate insulator on silicon with our measured C–V curve at 1 MHz, we calculated an interface state density $D_{it}=7.8 \times 10^{-10}$ cm^2 eV. Meanwhile, only a small shift in gate voltage was observed in the hysteresis of the STO capacitor using a dual C–V sweep from -3 V to 2 V.
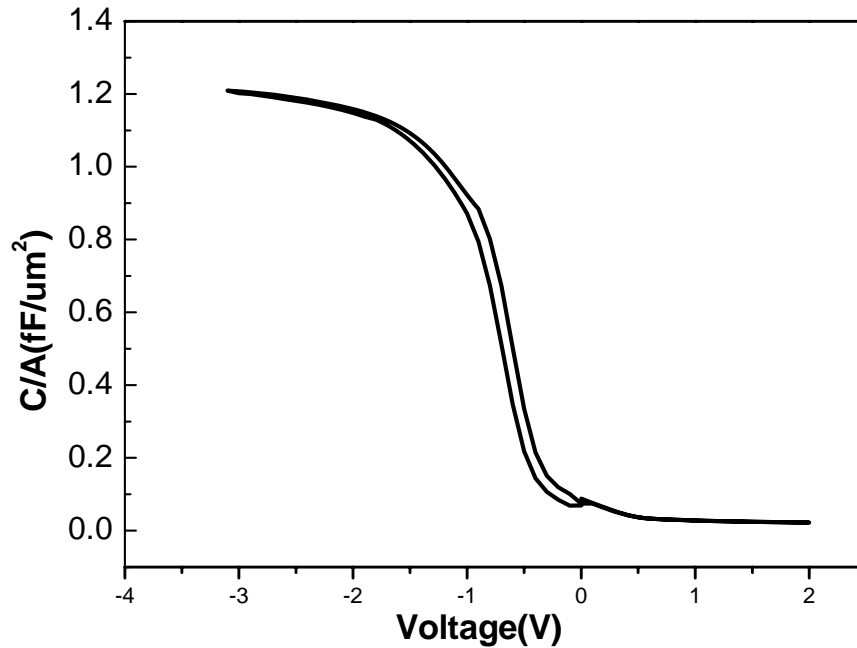
Fig. 5.13   Capacitance-voltage dependence of the STO/Si heterostructure.

Figure 5.14 shows the leakage current density as a function of bias voltage for the STO films. The magnitude of the horizontal axis represents the applied voltage on the gold electrode for the STO film. The film was found to be electrically highly resistive. When the test voltage = 1 V, for example, the leakage current density of the STO film (200 nm thick) is $\sim 5\times10^{-6}$ A/cm^2. This resistivity is similar to or even better than literature reports.
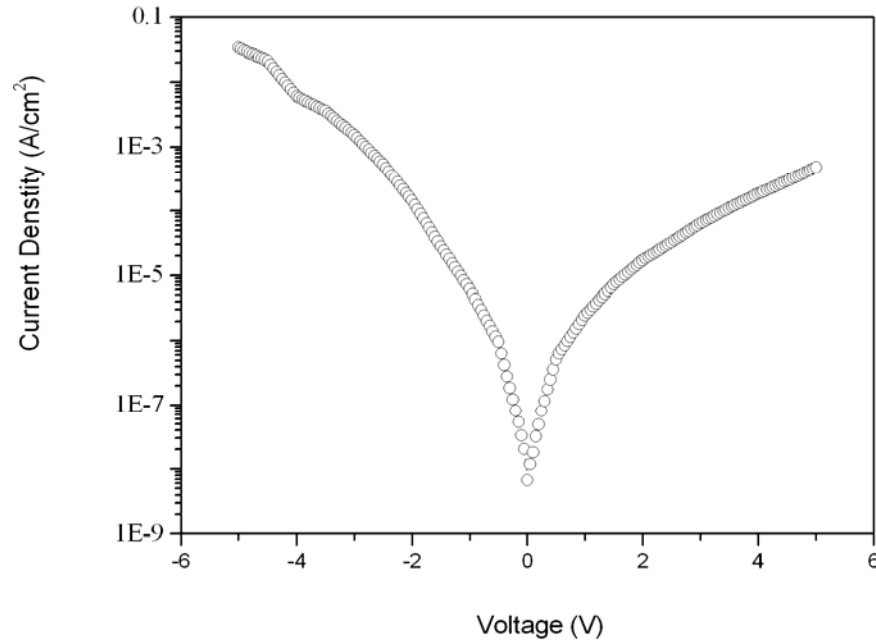
Fig. 5.14   Current-voltage dependence of the STO/Si heterostructure.

5.5 Sample heterostructure with STO/Si as substrate

Apart from the structural and electrical characterizations, we have developed a heterostructure of NBCO/STO/Si (NBCO stands for the superconducting oxide with a nominal composition of NdBa$_2$Cu$_3$O$_7$) to demonstrate the application of STO/Si as

substrate. The deposition conditions for the NBCO film were very much similar to that for STO. X-ray diffraction measurements revealed that the NBCO was well crystallized and epitaxially aligned with STO as shown in Figure 5.15. As shown in the inset of Figure 5.15, the epitaxial relationship of all layers is as: $(001)_{NBCO}//(001)_{STO}//(001)_{Si}$ and $[100]_{NBCO}//[100]_{STO}//[110]_{Si}$.
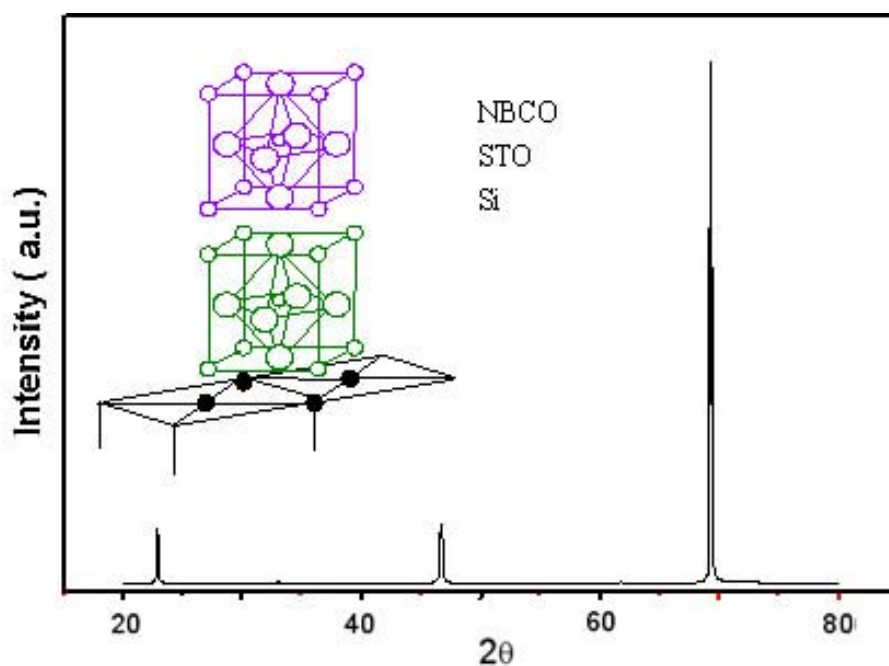
Fig. 5.15   X-ray diffraction pattern of the NBCO/STO/Si heterostructure. The inset shows the epitaxial relationship of the unit cells of NBCO, STO and Si.
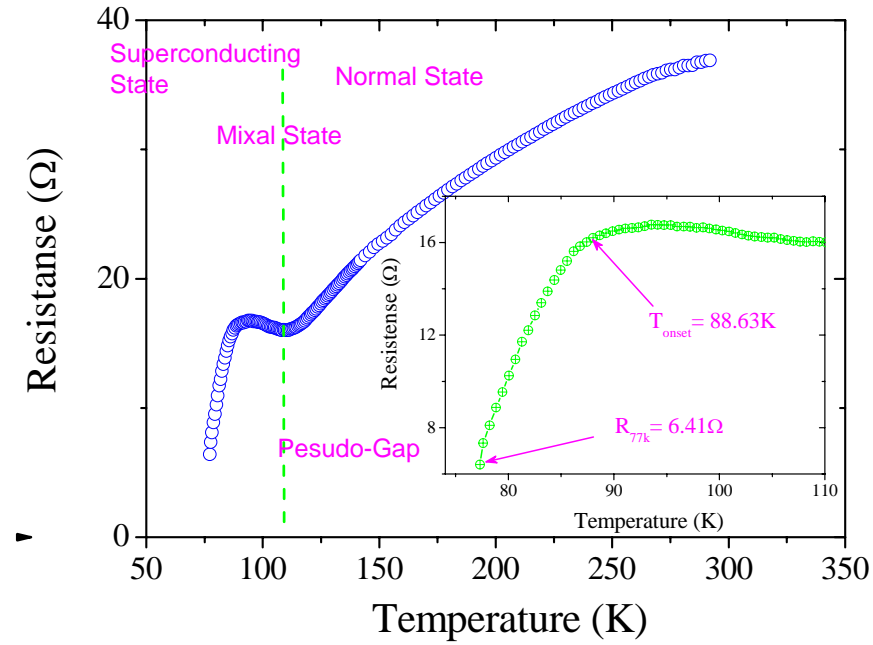
Fig. 5.16 Electrical resistivity as a function of temperature in a NBCO thin film

grown on STO/Si.

The electrical resistivity of the NBCO layer was determined over a wide temperature range. As shown in Figure 5.16, the resistivity decreased as the temperature decreased and dropped very quickly when the temperature was below 90 K, a behavior very much analogue to the NBCO film grown on $SrTiO_3$ single crystal substrates [Y. J. Li, 1998]. This result suggests that our NBCO film grown on STO/Si is of high quality.

5.6 Integration of BST thin film on Si

5.6.1 The necessary of integration BST thin films on Si

Barium strontium titanate (BST) thin films grown on oxide single-crystal substrates (such as MgO, $LaAlO_3$) for tunable microwave devices have been

extensively studied over the years. Recently, there has been an increasing interest in the integration of BST thin films on silicon substrate for similar applications. It is reported that the loss tangent of Si substrate changes with resistivity and frequency [S.Gevorgian, 1998]. Namely, low resistivity silicon substrates contribute high dielectric loss at high frequencies, while the high resistivity silicon substrates will significantly reduced dielectric loss. Therefore, the use of high resistivity silicon substrate is an attractive potential for mass-produced low loss microwave devices. By conducting computer simulation using lumped element model to study the influence of Si resistivity on the performance of BST-based phase shifter with the assumption of the dielectric constant of silicon is a constant value (11.7) regardless of resistivity, the comparative study indicates that by using high resistivity silicon, we can achieve low tangent loss, low return loss and low insertion loss at high frequency applications. Additionally, it is interesting to note that, although originally the development of the $SrTiO_3$/Si heterostructure was mainly motivated by the potential use of $SrTiO_3$ as a high-k material, the present research has actually shown the $SrTiO_3$/Si structure can be a good reference for integration of other perovskite oxide devices on Si. The heterostructure of BST/high-R silicon for tunable microwave devices is one good example. Potentially this structure can replace the conventional heterostructure of BST/single crystal provided.

5.6.2 Processing technique of BST thin films on Si

To further achieve low tangent loss, low return loss and low insertion loss at high frequency applications, The Si substrates were first oxidized to form a block layer with the thickness of 500 nm. According to the deposition process of STO on

Si, the deposition was conducted via a two-step procedure: The freshly cleaned wafer, together with two targets (high-purity Sr and $Ba_{0.7}Sr_{0.3}TiO_3$), were installed in the vacuum chamber of the laser-MBE system. After the target installation, the chamber was immediately evacuated by using a mechanical pump and a molecular turbo pump. 1) Dry-cleaning. When the pressure in the chamber was lower than 1×10^{-6} Torr, the Si wafer was heated up to 850 °C and kept at this temperature for 15 mins, with the aim of forming a atomically smooth surface. Then the temperature was lowered to a temperature T_d and a very thin layer of strontium was deposited by irradiating the Sr target with a pulsed KrF excimer laser beam. This step aimed to remove the thin SiO_2 layer to produce a layer which is crystallized and has a lattice structure which matches with that of perovskite BST. 2) Deposition. Following the deposition of the Sr layer a BST layer was deposited. Initially a relatively low substrate temperature (~650 °C) and low oxygen pressure (0.02 Pa) were used, while at a later stage the temperature and oxygen pressure were increased to ~800 °C and 50 Pa, respectively.

5.6.3 Structure characterization of BST thin films on Si

Crystallographic characterizations of the samples were performed in a Bruker AXS D8 Discover X-ray diffractometer. The surface morphology of the BST thin film was observed in an atomic force microscope (AFM, Digital Instrument Nanoscope IV) working in the tapping mode. A JEOL JEM-2011 transmission electron microscope (TEM) was used to observe the crystal structure and interfaces at the atomic level. Gold interdigital electrodes on the thin films were fabricated by the photolithography and wet chemical etching techniques. The capacitance was

measured using a HP4191B impedance analyzer (50M to 1.8G). The dielectric constants of the thin films were extracted from the measured data using a Mathematica program based on Gevorgian's model [S. S. Gevorgian, 1996].
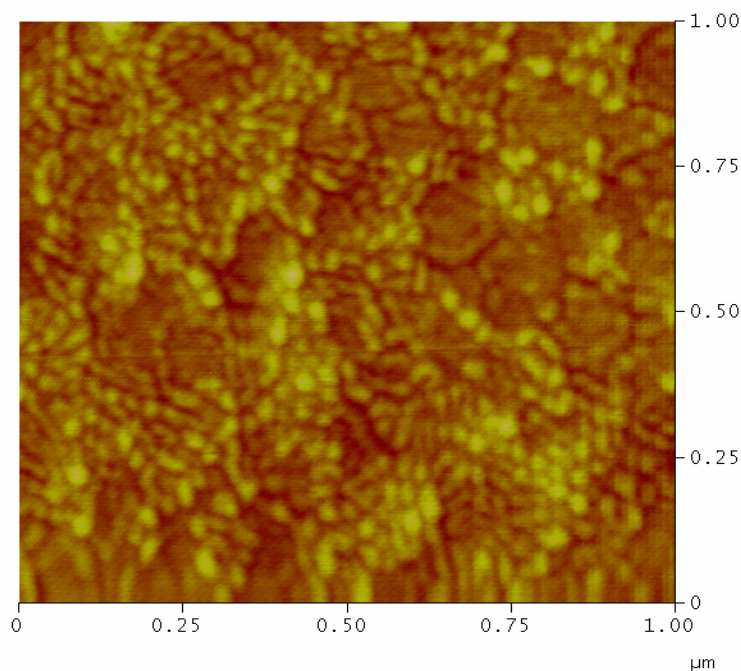
Fig. 5.17   Atomic force microscope image of BST/SiO$_2$/Si.
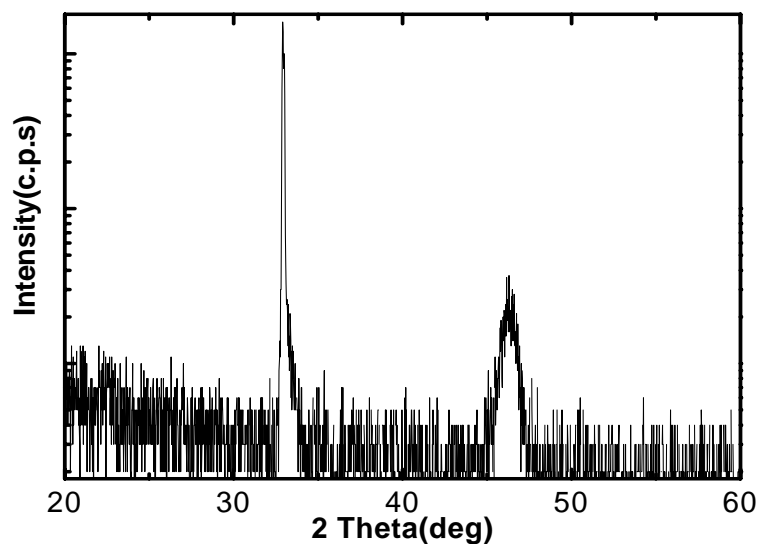
Fig. 5.18   X-ray diffraction patterns of BST/SiO$_2$/Si.

The structure of the BST 70/30 thin film was investigated by means of AFM

and XRD. AFM observation indicates that the film has a smooth and dense surface, as shown in Figure 5.17 The average grain size was estimated to be ~ 30 nm in diameter. The root-mean-square (r.m.s.) roughness is about 1.542 nm over a 1×1 μm^2 area of the film. Figure 5.18 shows the typical θ-2θ X-ray diffraction patterns of the film. Only BST (00l) peaks appear indicating the BST films were single phase and c-axis oriented.

Transmission electron microscopy (TEM) studies were carried out on a JEOL JEM-2011 microscope operated at 200 kV. The cross-sectional image in Figure 5.19 shows that the BST film was crystallized and about 70 nm thick. The density of dislocations is very high near the interface and is reduced as the film grown thicker. The inset shows the corresponding component as indicated as A1, A2, A3. Between the Si and BST thin films, there exists an amorphous SiO_2 layer which acts as a block layer to reduce the microwave loss. Using Sr to remove a thin layer of SiO_2 and produce an ordered surface is found to be crucial for the subsequent BST films. Selected area diffraction patterns (SAD) taken at A1, A2, A3 are demonstrated in Figure 5.20.
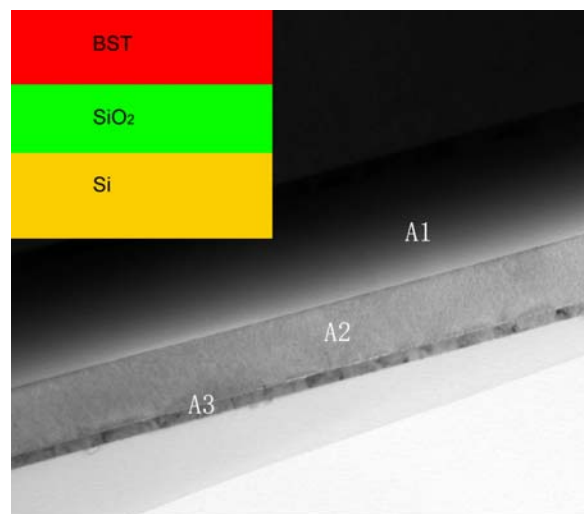
Fig. 5.19   The cross-sectional transmission electron microscope image of BST/Si.
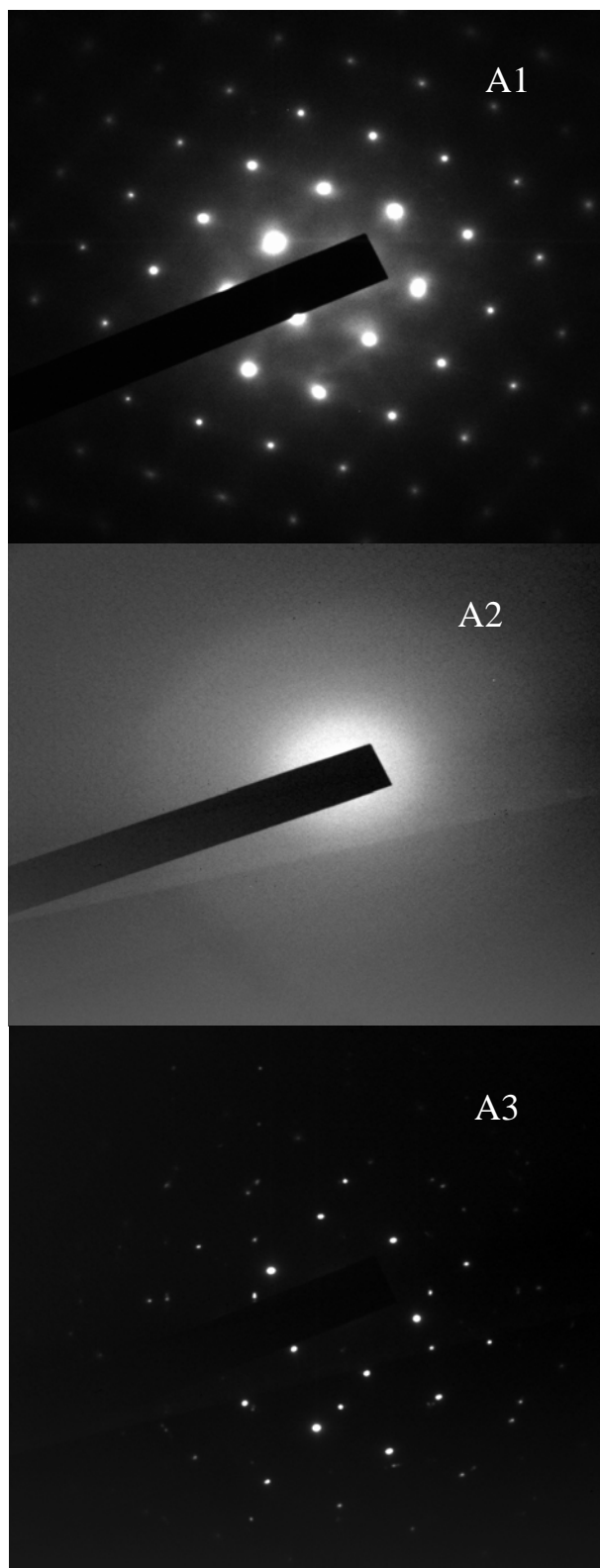
Fig. 5.20　Selected area diffraction patterns of BST/Si taken at A1, A2, A3.

5.6.4 Electric properties of BST thin films on Si

The in-plane C-V characteristics of the BST film were investigated at 1 GHz. The tunability is a description of the dielectric constant as a function of DC bias, which is defined as $\Delta\varepsilon / \varepsilon = (\varepsilon_{E=0} - \varepsilon_E) / \varepsilon_{E=0}$, where ε_E and $\varepsilon_{E=0}$ are the dielectric constant measured under a DC bias with field strength E and under no DC bias, respectively. As shown in Figure 5.21, a strong dependence of ε on the DC bias field was observed. To raise and lower the voltage both reduce the value of the dielectric constant. The maximum in-plane dielectric tunability is calculated to be 50% at 1 GHz under a moderate DC bias field of 13.3 V/μm. Our results are comparable with some of the reported data on BST films based on single crystal oxide substrate, even with parallel plate capacitors. These results indicate that BST/Si structure is believed to be a promising candidate in the development of ferroelectric-based microwave devices.
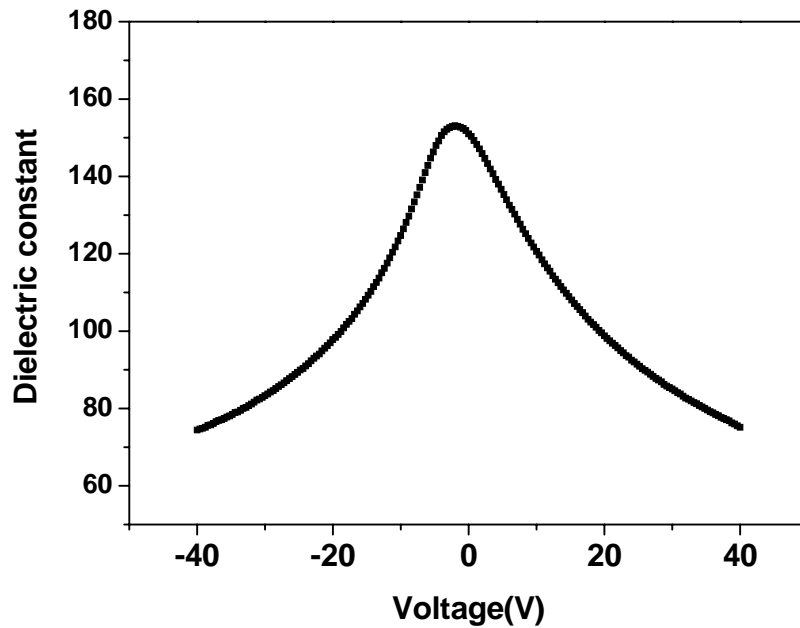
Fig. 5.21   In-plane C-V curve of BST thin film grown on Si substrate at 1 GHz.

5.7 Summary

High quality $SrTiO_3$ thin films have been deposited on Si wafer through laser molecular beam epitaxy. Prepared under optimal conditions, STO thin films were found to be well crystallized and epitaxially aligned. XRR and TEM observation revealed that heterointerface was relatively atomically smooth except for certain local dislocation due to the interaction and diffusion at the interface layer.

The electrical measurements indicated that the STO film was highly resistive. STO buffered Si substrates is good enough for the following epitaxial growth of perovskite oxide thin films.

Basing on the processing technique of integrating of STO on Si, BST thin films were successfully deposited on the Si with the SiO_2 layer as the block layer. This BST/Si structure is believed to be a promising candidate in the development of ferroelectric-based microwave devices.

CHAPTER 6

Simulation and characterization of $Ba_{0.7}Sr_{0.3}TiO_3$ thin films based phase shifter

6.1 Introduction

Ferroelectric phase shifter design is based on the nonlinear dielectric property, which can be manipulated by application of a DC electric field in various ferroelectric materials, such as $BaTiO_3$, $(Ba,Sr)TiO_3$, and $(Na_{0.5},K_{0.5})NbO_3$. At present the advanced devices technology using thin film process for the ferroelectric thin films enables the development of microwave tunable devices including tunable filters, frequency converters, and parametric amplifiers. Among the various ferroelectric materials, $(Ba,Sr) TiO_3$ has been regarded as one of the most promising ferroelectric materials for tunable microwave applications, due to high dielectric tunability, high breakdown field and relatively low dielectric loss. To obtain high quality BST thin films, various process techniques are being used. Using the process parameters studied in the above chapters, highly crystallized barium strontium titanate thin films with desirable dielectric property has been obtained. This section describes the detailed of the BST films based phase shifter. Design, simulation, modeling, fabrication and experimental results of the ferroelectric phase shifter are presented and discussed here.

6.2 Critical design parameters

The performance of phase shifter based on the BST thin film ferroelectric materials depends on several design parameters. The followings are the importants:

1) Tunability of BST thin films

2) Thickness of the BST thin films.

3) The total number of interdigital capacitors

4) Dimension of 50 Ω transition lines, interdigital capacitor, distribute parameter inductance, and ¼ λ impedance line.

6.3 Target performance of phase shifter

i) 9 GHz +/- 200 MHz bandwidth

ii) 22.5 degrees per bit; 45 degrees for 2 bits

iii) Insertion loss (S_{21}>-5dB); return loss (S_{11}<-10dB)

6.4 Device Structure

The substrate we use in previous chapters is LAO which has a rhombohedral structure at room temperature. It has a relatively high surface roughness a rough surface due to crystallographic twinning, which leads to the creation of defects during epitaxial growth. Among the other commercially available single crystal oxide substrates, MgO is known to be hygroscopic and CaO is an inevitable impurity. LSAT has been regarded as a promising substrate in terms of crystal structure and cost. Therefore, our BST based phase shifters were deposited on the single crystal

$(LaAlO_3)_{0.3}(Sr_2AlTaO_6)_{0.7}$ (LSAT) substrates. Additionally, we also used SiO_2/Si substrates for BST based phase shifters, unfortunately, the performance was not comparable to that of phase shifters based on LSAT. Therefore, we partially describe the phase shifters on LSAT in detail in the following section.

Figure 6.1 shows the cross sectional view of the ferroelectric BST based phase shifter. Figure 6.2 show the top metal structure of phase shifter. As shown in Figure 6.2, The top electrode designed with the Ground–Signal-Ground (GSG) configuration, consists of 2 sets of interdigital transducers that exhibit a low pass filter model and BST thin films is used for dielectric tunability. The transmission line can be designed to behave as series inductors. The overall length and width of each phase shifter are 9.2 mm and 8.9 mm respectively. So, the overall device dimension is 9.2 mm $\times$ 8.9 mm. Figure 6.3 demonstrates the dimensions of the DC block capacitor and the interdigital capacitors. The thickness of the BST thin films is taken as 300 nm. Gold (Au) is used as a conductor metal of this phase shifter. Since Au is not good interfacing with BST materials, a very thin layer of Ti/W (200 nm) is used as an adhesion layer to increase the adhesion of the top metal.
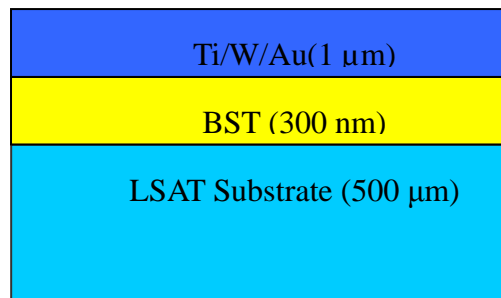
Fig. 6.1   Cross sectional view of different layers of the BST based phase shifter.
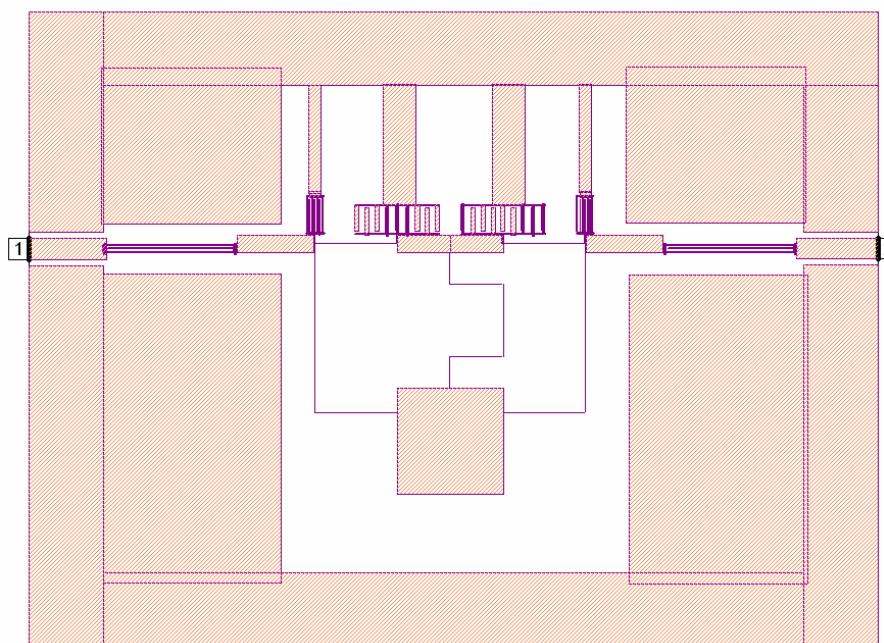
Fig. 6.2   Top metal pattern of the BST based phase shifter.
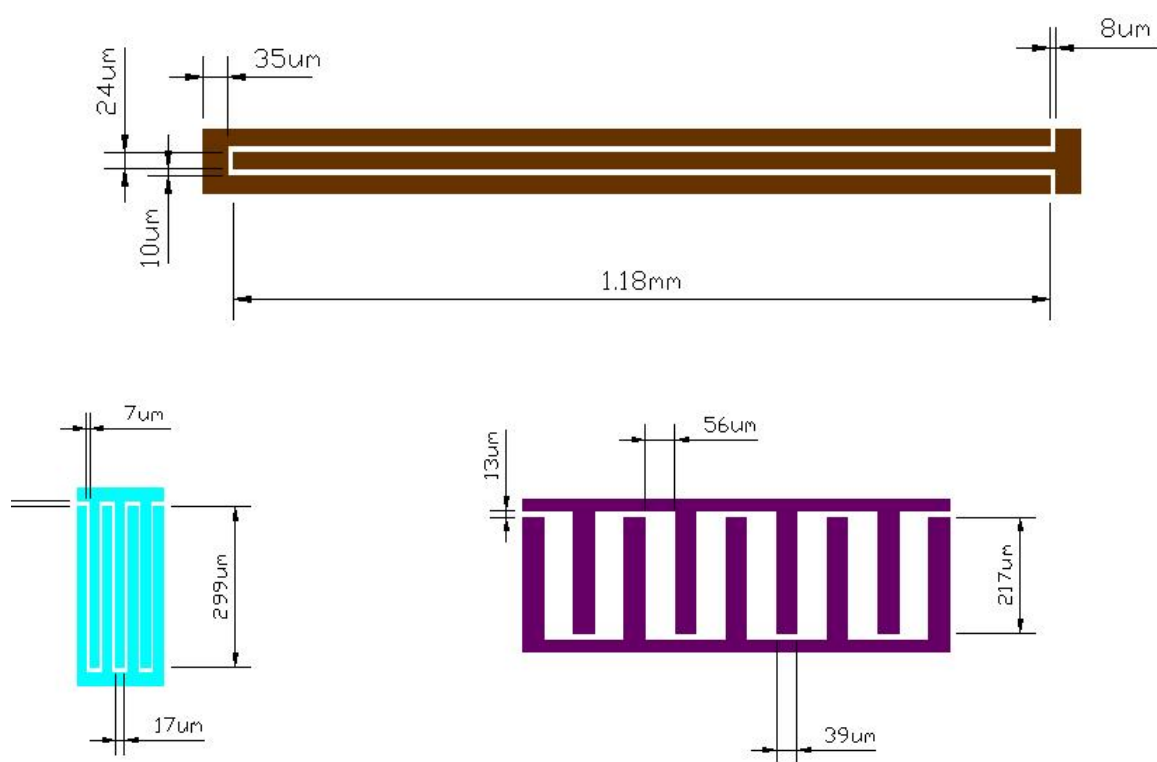
Fig. 6.3   Dimension of the DC block capacitor and intergital capacitors.

6.5 Modeling of the phase shifter

To help design the phase shifter which can produce the expected performance at microwave frequency, in this section, we focused our attention on the modeling of phase shifter using Applied Wave Research's (AWR) Microwave Office tools. Electromagnetic simulation will be considered later and the results were compared. Figure 6.4 shows lumped element electrical modeling of the phase shifter described in Figure 6.2. From the electrical modeling, we see that the designing is based on the low pass filter with two sets of interdigital capacitors as well as the DC block capacitors. One can easily realize that the degree of phase shift depends on the number of interdigital capacitors. If larger phase shift is needed, more interdigital capacitors should be used. Since the parasitic capacitance of the transmission line is very small, we can ignore their influence in our current design. DC bias can be added to the interdigital capacitor to change the value of capacitance of the dielectrics and achieve the resulting phase shift. According to the degree of phase shift, we can deduce the values of each element in the circuit. Then we use the distribute elements to replace the lump elements as shown in Figure 6.5.
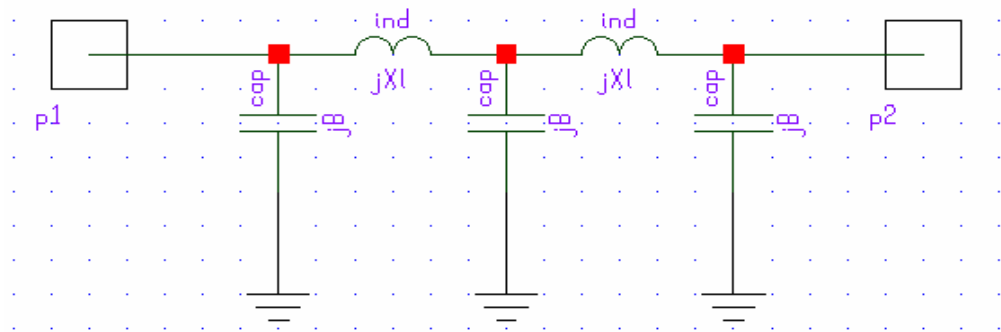
Fig. 6.4   Lumped element electrical model of low pass phase shifter.
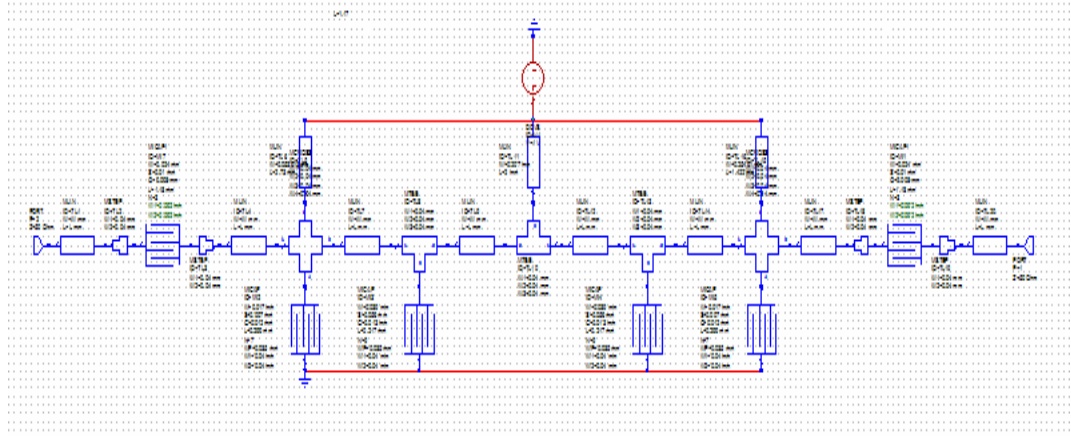
Fig. 6.5   Equivalent electrical model of the phase shifter with distribute elements.

In our lumped element model as shown in Figure 6.4, the series inductance branch was fixed to be 0.4 nH and tuning of the phase shifter of the lumped element model were carried out to obtain 0.1 pF at about 9 GHz.   The dimensions of the interdigital transducers on both the inner and outer arms of the schematic model are fine tuned in simulation to correspond to the individual sections of the lumped element model in Figure 6.4.   By systematically optimizing the electrical model, the optimal performance of BST thin films based phase shifter can be obtained. The magnitude and phase of S_{11} and S_{21} as function of frequency under different tunability (*K*) are demonstrated in Figure 6.6 and Figure 6.7 respectively. At the whole frequency range, it can be observed there is no large dependence of the insertion loss (S_{21}) on the tunability. To lower or raise the tunability, the insertion loss remains unchanged. It is noted that the insertion loss keep the value of great than -0.5 dB. Unlike the influence of tunability on the insertion loss, the return loss is more sensitive which is found to be lower than -14 dB at the whole studied frequency range. Furthermore, at the same frequency, to decrease the capacitance of interdigital capacitors will result in the decrease of return loss. On case of the phase of S

parameters, as shown in Figure 6.7, the phase of S_{21} changes with the tunability at the same frequency. At 9 GHz, the degree of phase change is up to 50° with the tunability of 60%. Larger phase shift can be obtained by adding more interdigital capacitors into the circuit. These simulated results indicate that this electrical model based on low pass filter can meet the requirement of our ferroelectric phase shifter.
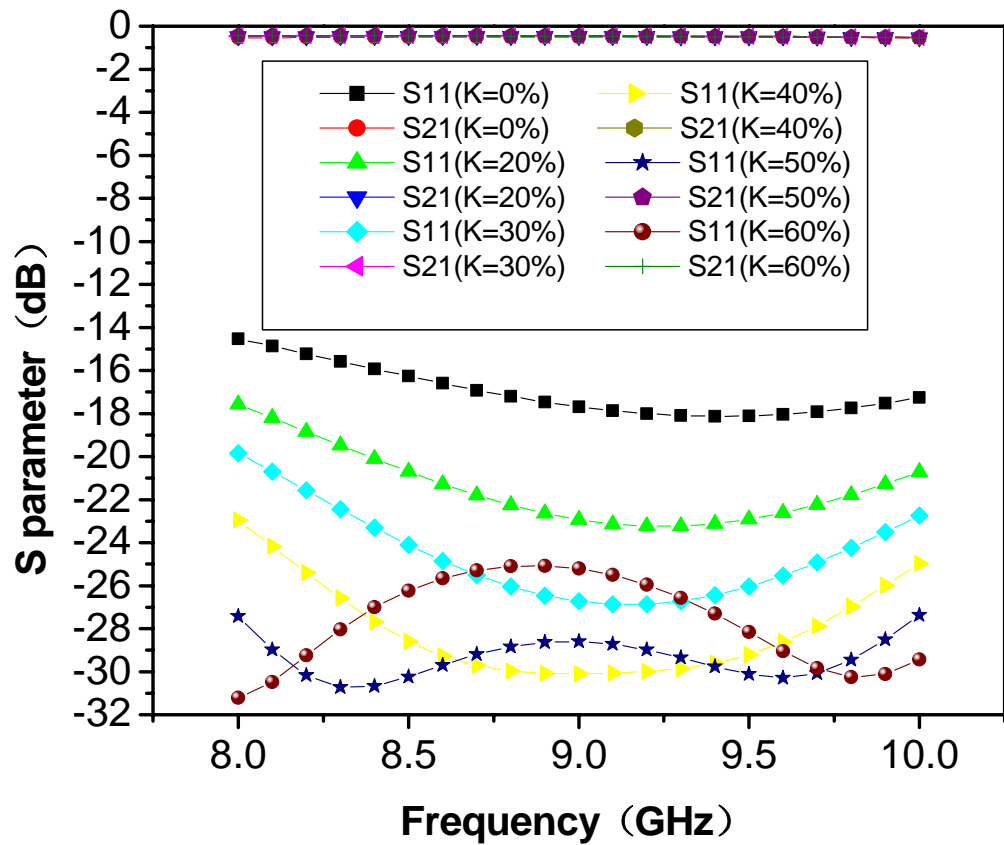
Fig. 6.6   Simulated magnitudes of *S* parameters under different tunability of the
BST thin films.
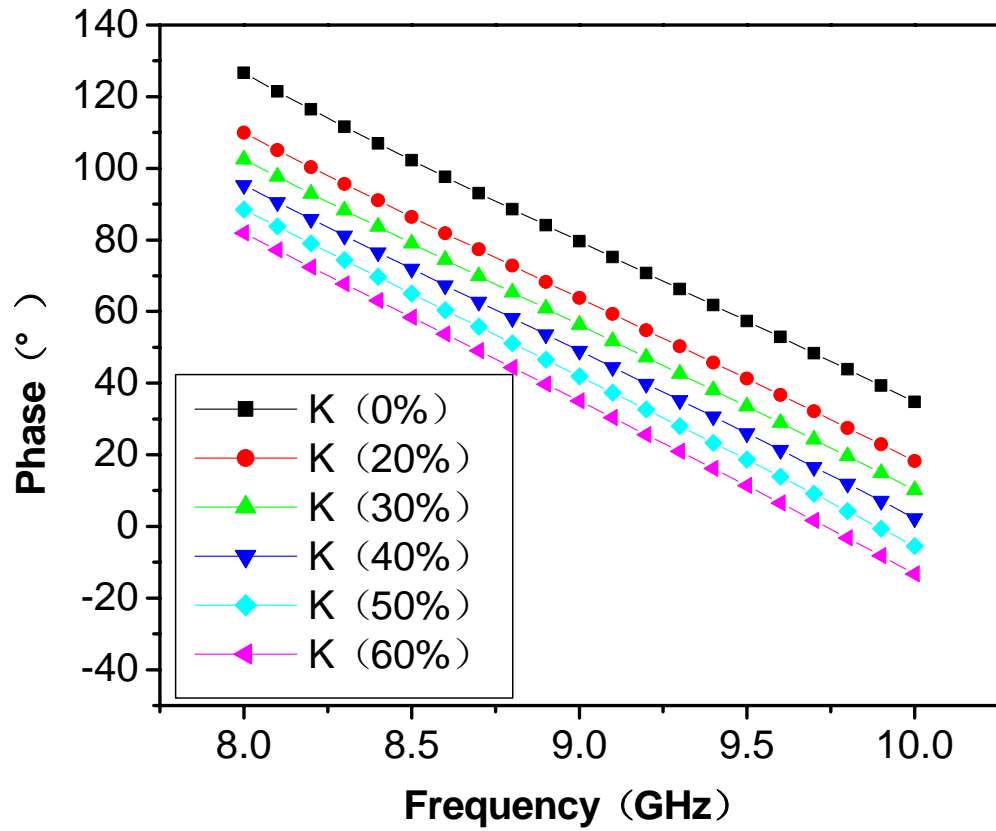
Fig. 6.7   Simulated Phase of S_{21} under different tunability of the BST thin films.

6.6 Discussion on Electromagnetic (EM) simulation results

6.6.1 Dependence of performance of phase shifter on the dielectric layer BST

The performance (e.g. high return, low insertion loss and etc.) of the ferroelectric BST thin films based phase shifter depends on the physical and electrical properties of the ferroelectric materials of BST thin films. High capacitance value increases the return but it also increases the insertion loss. The capacitance value can be increased by using high dielectric constant of the ferroelectric thin-films or changing the physical dimension like the thickness of the dielectric layer. The

dielectric constant of the BST thin films can be changed with the variation of composition (Ba/Sr ratio) and thickness can be controlled when we deposit the thin films. In light of this, the physical and electrical properties of the dielectric layer influence on the performance of the phase shifter should be studied to operate the device at the optimized performance. AWR simulation tools offer us the chance to carry on such kind of work because electromagnetic (EM) simulation could be conducted given the proper boundary conditions. In this part, we will focus our attention on the EM simulation of our developed BST thin films based phase shifter. The relationship between physical and electrical properties of the dielectric layer and the performance of phase shifter can be obtained.
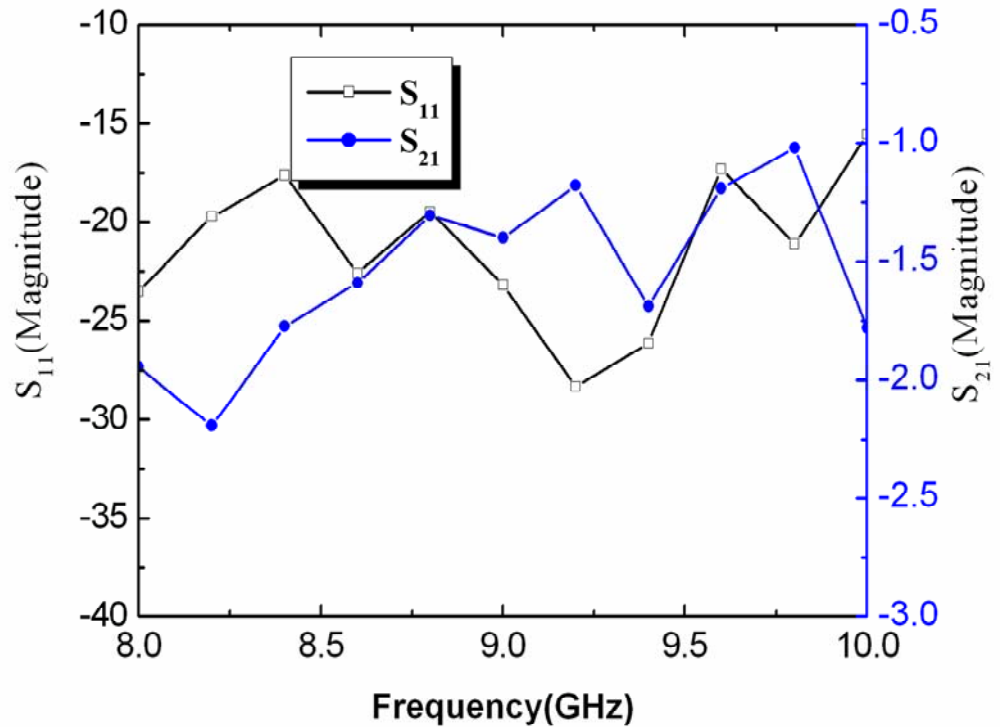
Fig. 6.8   EM simulated *S* parameters as function of frequency.

6.6.2 EM simulated S parameters of BST thin films based phase shifter

In these current designs, relative dielectric constant, loss and thickness of the dielectric layer are fixed at 300, 0.04 and 300 nm respectively. By setting up the enclosure and applying the proper boundary conditions to the EM structure shown in Figure 6.2, the simulated S parameters as function of frequency is demonstrated in Figure 6.8. The insertion loss is larger than -5 dB while the return loss is lower than -15 dB when the frequency is ranging from 8 to 10 GHz. it is found that EM simulated results show a small difference from the above results simulated from the electrical model. For example, at a particular frequency of 9 GHz, the insertion loss simulated from electrical model is -0.3 dB instead of -1.3 dB while sacrificing the return loss from -27 dB to -17 dB.

6.6.3 Influence of parameters of dielectric layer on the phase shifter

A comparative study on the simulation between the physical properties (thickness) of BST thin films and the performance was conducted. The thickness of BST thin films is selected from 20 nm, 60 nm, 100 nm, 200 nm and 300 nm while the value of the dielectric constant and frequency is fixed at 300 and 9 GHz respectively. The thickness dependence of S parameter is shown in Figure 6.9. By increasing thickness from 20 nm to 300 nm, the return loss changes from -8.6 dB to -27 dB while the insertion loss from -9.2 dB to -1.3 dB. We can achieve high return loss and low insertion loss at thickness of 300 nm. This justifies for the use of 300 nm BST thin films for our phase shifter.
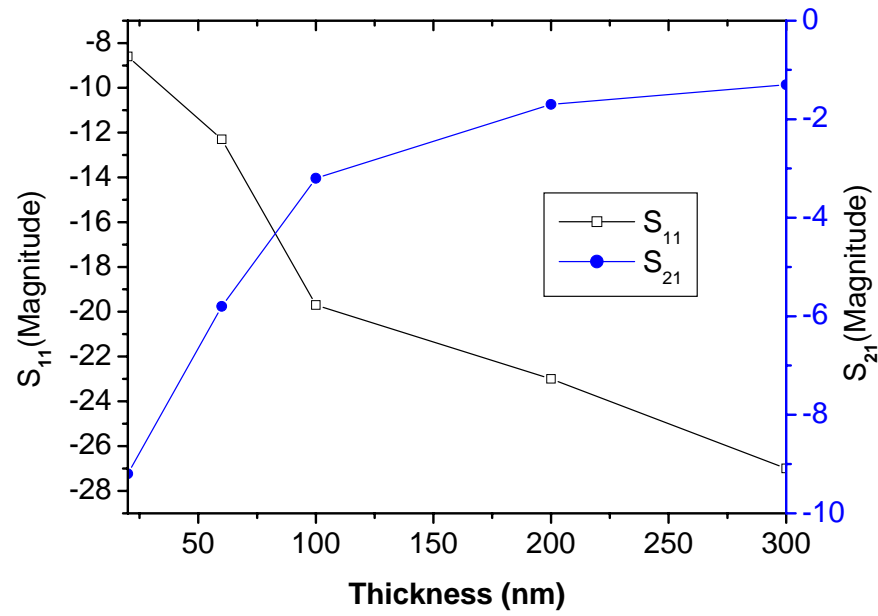
Fig. 6.9   The thickness dependence of S parameters.

Apart from the influence of thickness on the *S* parameters, it is worthwhile to study the dependence of *S* parameters on the dielectric constant to investigate the phase shift produced by the changing of dielectric constant at our designed frequency of about 9 GHz. Figure 6.10 shows the insertion loss and return loss of the device as function of dielectric constant. The insertion loss stays larger than -2 dB when the dielectric constant of BST films is increased from 100 to 500 as shown in Figure 6.10.   On the other hand, the return loss is lower than -18 dB.   At our designated frequency of 9 GHz, there is no significant change in the value of the insertion loss comparing with the variation of the return loss.

The influence of the dielectric constant of BST thin films on the phase of *S_{21}* is as shown in Figure 6.11.   At the designed frequency of 9 GHz, it is found that the change the dielectric constant affects the phase of *S_{21}*.   By changing the dielectric constant from 100 to 500, a stable phase shift of 80 degrees can be approximated. To

get 45 degrees phase shifter, the change of dielectric constant from 300 to 100 is needed.   It shows (not shown here) that dielectric constant, however, does not have large contribution to the phase of S_{11} of the device.

By simulation it is found that the physical and electrical properties of BST thin films have important effect on the performance of phase shifter.   At our designated frequency of 9 GHz, we can achieve required phase shift, insertion loss and the return loss when BST thin films have thickness of 300 nm and the change of dielectric constant from 300 to 100. These parameters may be a good reference for practical application of ferroelectric phase shifter and will be utilized in our following experimental phase shifter based on BST thin films.
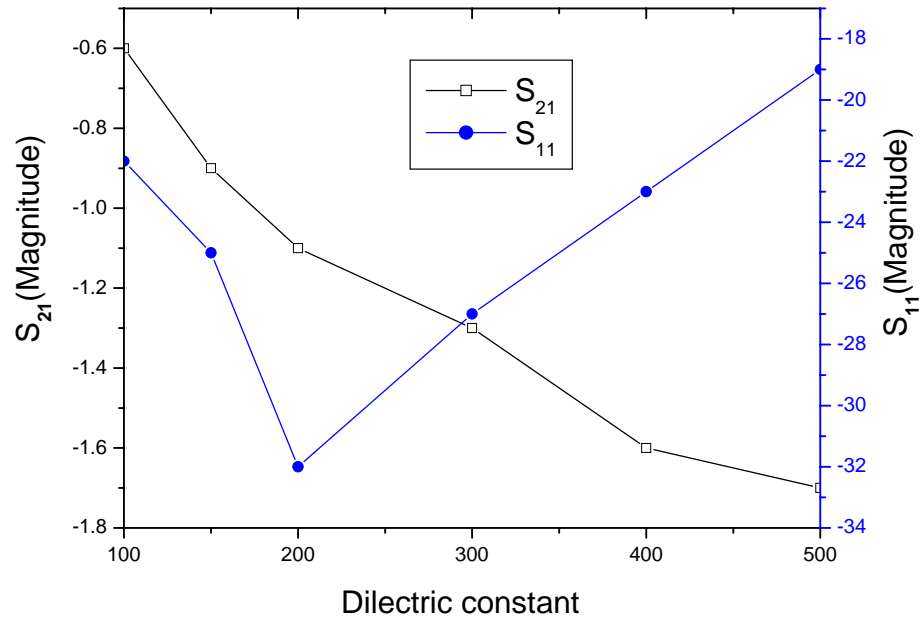
Fig. 6.10   The dielectric constant dependence of *S* parameters.
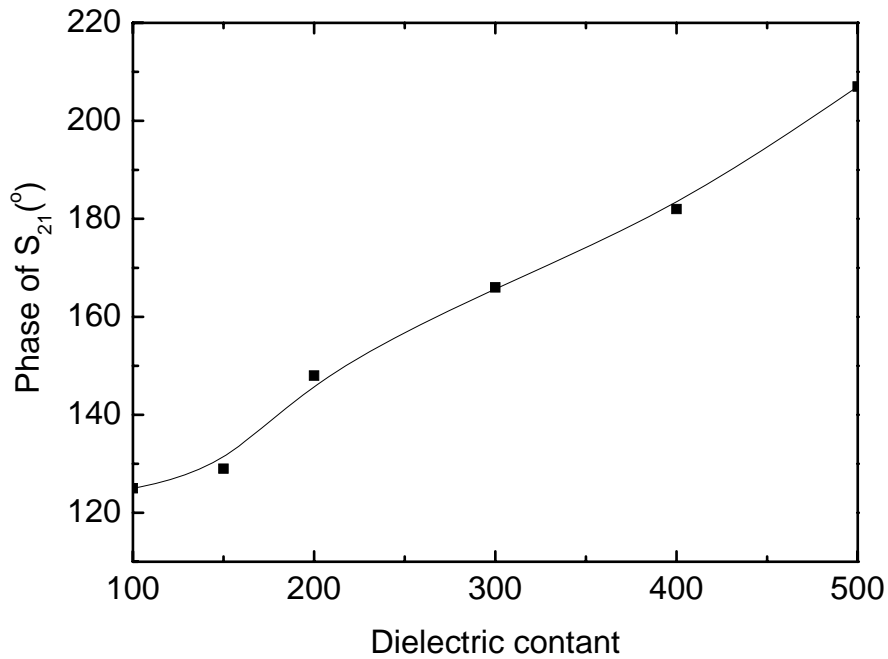
Fig. 6.11 The phase of S_{21} vs. dielectric constant.

6.6 Experimental procedure and results

6.6.1 Experimental procedure

The $Ba_{0.7}Sr_{0.3}TiO_3$ (BST) thin film with thickness of 300 nm was deposited on a LSAT substrates using pulse laser deposition (PLD) process under the optimized fabrication parameters. After the BST thin film deposition, metal layer (200 nm Ti/W + ~1 µm Au) was defined and processed using standard photolithography and wetting etching process to complete the device fabrication. Figure 6.12 shows the final structure of the sample with a phase shifter pattern. Microwave testing of the device was performed by a network analyzer 8720ES (Agilent, USA) with a standard probe station Microtech RF-1 (Cascade, USA) and a pair of air coplanar ground-signal-ground (GSG) microprobes (Cascade, USA). For adding DC bias to

the microwave measurement, an external DC power supply Agilent 6629A was used.
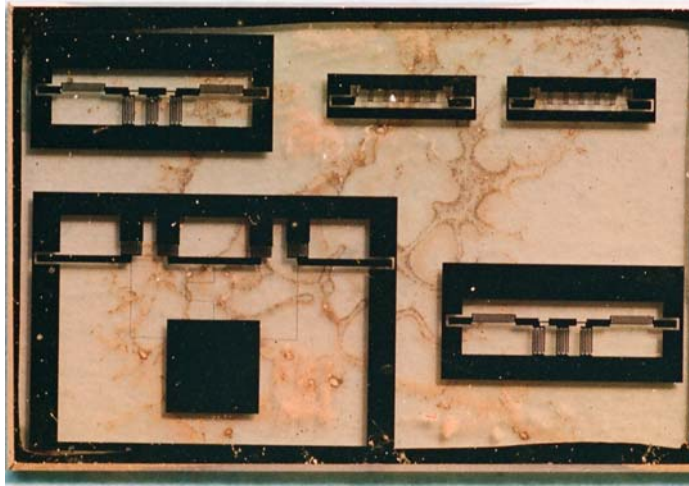
Fig. 6.12   The final structure of the sample with a phase shifter pattern.

6.6.2 Experimental results

The frequency response of the phase of S_{21} for the BST thin film based phase shifter at room temperature is plotted in Figure 6.13. This figure shows that the phase of S_{21} decreases with increasing frequency for all applied voltages within the frequency range of 8 to 10 GHz. There is an obvious change when the applied voltage changes from 0.0 to 10.0 V. As the applied voltage increases from 10.0 to 50.0 V, there is no large increase in the phase values. From 50.0 to 70 V the phase also changes slightly. This change in phase values corresponds to a decrease in the equivalent circuit capacitance and also in the relative dielectric constant of BST. As shown in Figure 6.13, a differential phase shift of around 70º can be obtained at the working frequency 9 GHz. The degree of phase shift is larger than that we expected.
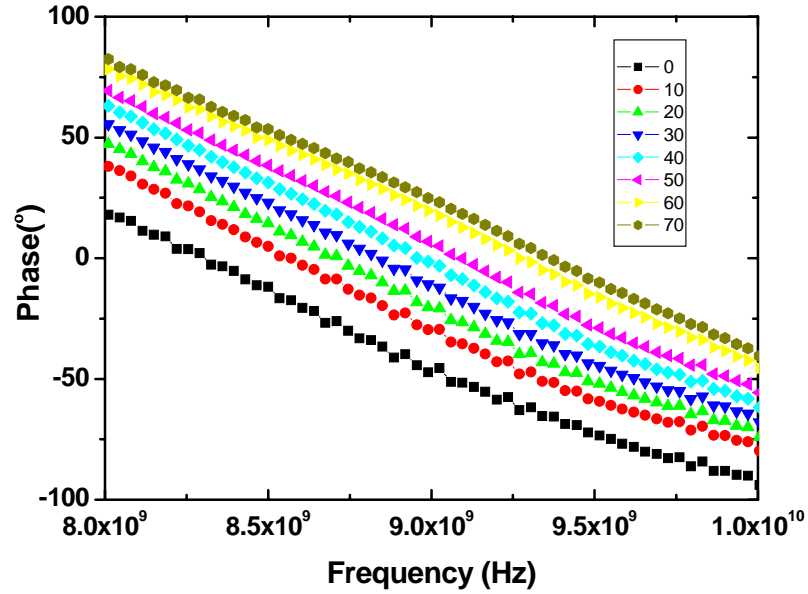
Fig. 6.13   The frequency response of the phase of S_{21} for the BST thin film based

phase shifter.

Figure 6.14 shows the experimental measurements of insertion loss and return

loss without and with a bias voltage of 70 V respectively. At 0 V, the insertion loss of

this phase shifter was measured approximately to be -1.31 dB at 9 GHz and was

above -5 dB up to 10 GHz. This figure also shows that the insertion loss slightly

changes with increasing frequency within the whole frequency range. By applying a

voltage up to 70 V, no large change of the insertion loss can be observed. Comparing

with the value of insertion loss without the bias at the same frequency, there is a

slight decrease. On the case of return loss, S_{11} has been obtained approximately to be

-14.3 dB and -15.5 at DC bias of 70 V and 0 V respectively under the working

frequency of 9 GHz. Furthermore, S_{11} indicates an unchanged trend with the

frequency and DC bias as shown in Figure 6.14.
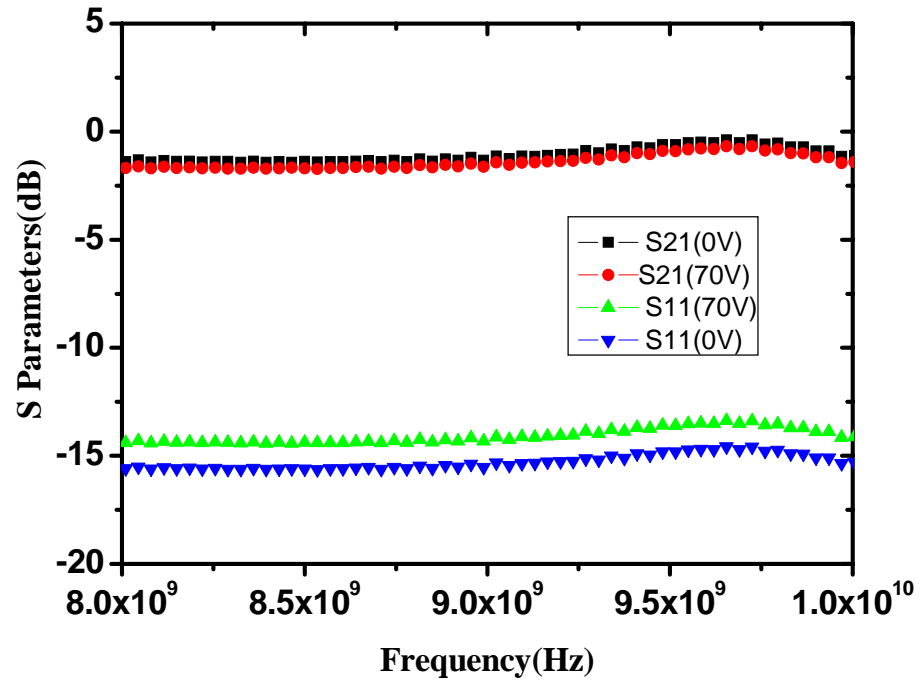
Fig. 6.14   The experimental swept frequency for insertion loss and return loss at the voltage of 0 and 70 V.

The figure-of-merit (FoM) defined as degree of phase shift per dB is the most important parameter to evaluate the performance of a phase shifter. To calculate FoM, the equation can be defined as the quotient of the differential phase shift and the insertion loss. At 9 GHz, the differential phase shift is 70º and the insertion loss is -1.3 dB under a DC bias of 70 V, the figure-of-merit of this phase shifter is determined to be about 60°/dB, which suggests that the BST thin films based phase shifter could be a promising candidate for tunable microwave devices application. Additionally, it is useful to note that this value can be improved:

1) Through material and pattern optimization.

2) By applying higher DC voltage to increase the electric field.

3) By using more interdigital capacitors to increase the phase shift

4) By lowering the insertion loss through improving the electrode patterning.

6.7 Summary

In this Chapter, the simulation and experimental work were introduced on BST thin film based microwave devices. Also the performance of phase shifter under DC bias has been preliminarily developed and described.

By simulation, it is found that the ferroelectric phase shifter based on the low pass filter can achieve our required phase shift, insertion loss and return loss at the designated frequency of 9 GHz. Moreover, physical and electrical properties of the dielectric layer BST thin films have significant influence on the performance of phase shifter. The BST thin films with thickness of 300 nm and the change of dielectric constant from 300 to 100 were found to be the required specifications for our target performance.

A figure-of-merit of 60°/dB for the realized BST thin films phase shifter has been demonstrated at 9 GHz and at room temperature, applying a DC bias voltage of 70 V. This figure-of-merit can be expected to be distinctly improved, if particularly the microwave losses can be reduced and the tunability of the relative dielectric constant can be increased, or if still higher electrical field strength can be applied on the phase shifter. Since ferrlelectric phase shifters on low-cost ferroelectric BST thin films are suitable to be compactly integrated in phased array antennas, they can provide a very cost-effective technology for future microwave phase control devices.

Conclusion and future work

7.1 Conclusion

In the course of this study, high quality epitaxial $Ba_{0.7}Sr_{0.3}TiO_3$ (BST) thin films were deposited using pulsed laser deposition on single crystal substrates. Lattice strain influence on the structure and electrical properties has been investigated. A phenomenological thermodynamic theory using a modified Devonshire form of elastic Gibbs free energy was employed to study the strain effect. Performance of BST thin films based phase shifter was developed and characterized. Integration of perovskite material on Si was also carried out, demonstrating the possible integration of perovskite ferroelectrics with semiconductor industry. The main conclusions can be summarized as follows:

I. We establish the clear relationship between lattice tetragonality and ferroelectric and dielectric behaviors in BST thin films. Grown on single crystal substrates like $(LaAlO_3)_{0.3}(Sr_2AlTaO_6)_{0.7}$, $LaAlO_3$, $MgAl_2O_4$, we found that the BST films had a distorted structure. This distorted lattice structure leads to the enhanced dielectric and ferroelectric properties along the in-plane direction. Additionally, the structure, dielectric properties and ferroelectric properties of $Ba_{0.7}Sr_{0.3}TiO_3$ thin film along the in-plane direction is very sensitive to film thickness. When varying the thickness from 20 nm to 300 nm, it is observed that the in-plane lattice parameter (a) increased from 0.395 to 0.402 nm while

the out-of-plane lattice parameter (*c*) remained almost unchanged, which led to an increased *a*/*c* ratio (tetragonality) changing from 0.998 to 1.012. The remnant polarization (*Pr*) and coercive field (*Ec*) change from 8.39 μC/cm^2 and 2.17 V/μm to 1.07 μC/cm^2 and 1.71 V/μm   respectively. A reduction of Curie temperature and the reduction of the dielectric constant were also observed when thickness is decreased.

II. With the aid of homoepitaxial growth of STO on STO substrates and RSM, oxygen vacancies were found to play an appreciable role in the lattice structure of perovskite thin films.

III. Phenomenological method has been used to study the strain effect on the in-plane dielectric properties of BST thin films by means of biaxial (2-dimensional) and hydrostatic (3-dimensional) components calculated from the XRD results. The relationship between the dielectric properties and film thickness was attained by Landau-Ginsburg-Devonshire formalism including the fourth order Landau expansion of the polarization in the expression of the Gibbs free energy. Namely, the calculated Curie temperature and dielectric constant are proportional to the film thickness, which agrees well with our experimental results.

IV. Integration of perovskite thin films on Si is important from application of view. SrTiO$_3$ thin films have been deposited on Si (001) wafers by laser molecular-beam epitaxy using an ultra-thin Sr layer as the template. Structure characterization indicated that STO thin films were well crystallized and epitaxially aligned with Si with a sharp, smooth and clear interface. This STO

buffered Si can be used as promising substrates for integration of other function materials. According to this processing technique, BST thin films were also successfully grown on Si substrates with SiO_2 as a blocking layer to further decrease the microwave loss.

V. BST thin film based phase shifter has been designed with the aid of a commercial simulation software Applied Wave Office tools. The device performance was evaluated theoretically and experimentally. At the studied frequency range, the insertion and return loss were measured to satisfy with our target performance, namely, $(S_{21}) > $ -5 dB, $(S_{11}) < $ -10 dB. A figure-of-merit was found to be around 60°/dB at 9 GHz and at room temperature by applying a moderate DC bias voltage of 70 V. These results indicate that this prototype of phase shifter can provide a very cost-effective technology for future microwave phase control devices.

7.2 Future work

To understand the structure-properties relationship is an important issue to realize practical application of ferroelectric materials. In this work, lattice strain influence on the structural and electrical properties has been investigated. However, there are other important factors which play an important role to determine the dielectric and ferroelectric properties as described in the followings:

1) Interface effect – the influence of the state of the interface between the film and the substrate on the ferroelectric behaviors (polarization, coercive field strength and Curie temperature) and dielectric properties of BST

2) Grain size effect – the correlation of the grain size and the ferroelectricity and dielectric behaviors of BST thin films.

3) Doping effect – the influence of dopants and doping level on the dielectric behaviors, particularly the microwave frequency dielectric loss, of BST thin films.

4) Orientation effect – the influence of lattice orientation on the ferroelectric and dielectric properties of epitaxial BST thin films.

The loss in ferroelectric films is another important issue, especially for tunable microwave devices. Decreasing the dielectric loss of the ferroelectric film is of crucial importance for practical applications, and should be studied as function of the associated parameters. In this work the frequency dispersion was not considered. The frequency dispersion is fundamentally connected with characteristics of the dielectric loss. In light of this, frequency dispersion is desirable to be investigated.

Although a phenomenological thermodynamic theory has been successfully used to explore the strain effect on the dielectric properties of ferroelectric materials, there are still some discrepancies between our calculations and the experimental data due to the simplification of our model, especially on the case of dielectric constant versus the electric field. It is desirable to have a more comprehensive model for more accurate calculations. Such calculations will give more insight and better corrections between lattice strain and the dielectric response of BST films.

STO buffered Si substrates make it possible to integrate the perovskite functional materials with semiconductor industry. Based on the deposition parameters for epitaxial growth of STO on Si, Other perovkite functional thin films

(CRO/YBCO) could be grown on Si. Thus, crystalline substrates (MgO, LaAlO$_3$, Sapphire), which have been extensively considered for fabrication of tunable ferroelectric devices can be replaced.

The design of coplanar tunable microwave phase shifter could be optimized, eg. using smaller electrode gap and adding the total number of interdigital capacitors in the phase shifter to attain high effective electric field. Moreover, the electrode fabrication process need to be further improved to decrease the loss.

Integration of BST thin films on Si has been attained. Designing, simulation and fabrication of tunable microwave devices based on BST films on Si substrate can be conducted.

Appendix

Thermodynamics study on the mechanism

of removing SiO$_2$ using Sr

As mention previously, to grow single crystal STO films on Si substrates, the first important step is to obtain a clean Si surface without an interfacial amorphous Si oxide layer. A method for removing SiO$_2$ and producing an ordered Si surface using Sr has already been developed. The main role that Sr plays during the oxide removal process is used as catalysts promoting Si formation and passivating the newly exposed Si surface, preventing further etching and the formation of pits in the substrate. However, theory of thermodynamic has never been used to explore the mechanism of cleaning Si surface using Sr due to its sensitivity and difficulty to predict. In the following part, we will demonstrate the mechanism of deoxidation of SiO$_2$ due to the catalytic reaction SiO$_2$ + 2Sr $\rightarrow$ Si + 2SrO with the aid of thermodynamic equations.

Table A.1 lists the thermochemical data including enthalpy and entropy of the reactant and resultant in the above reaction at the standard pressure 1 bar (10^5 Pa) and 25 °C. Table A.2 shows the Moore heat capacity at constant pressure as the function of temperature at different temperature range [G. M. Barrow, 1988]. The physical state of the substance is indicated in parentheses by "s" for solid and "g" for gaseous state. These data will be used later to derive Gibbs free energy and Helmholtz free energy.

0

Table A.1 Enthalpy and entropy of the reactant and resultant

Material	$SiO_2(s)$	$Sr(g)$	$Si(s)$	$SrO(g)$
$\Delta_f H_m^\theta(298.15K)/(kJ \cdot mol^{-1})$	-217.1	40.174	0	-12.3
$S_m^\theta(298.15K)/(J \cdot mol^{-1} \cdot K^{-1})$	10.372	39.677	4.498	57.145

Table A.2 Moore Heat capacity at constant pressure: $C_{p,m} = a + bT + cT^2$

Material	$SiO_2(s)$		$Sr(g)$	$Si(s)$	$SrO(g)$
	298.15~543K	543~1996K	298.15~2000K	298.15~1685K	298.15~2000K
$a/(J \cdot mol^{-1} \cdot K^{-1})$	11.209	17.119	4.974	5.455	8.69
$b/(J \cdot mol^{-1} \cdot K^{-2})$	7.529	0.452	0	0.922	0.16
$c/(J \cdot mol^{-1} \cdot K^{-3})$	-2.412	-9.335	0	-0.846	-0.76

At the room temperature 25 °C

$$\Delta_r H_m^\theta(298.15K) = \sum_B v_B \Delta_f H_B^\theta$$
$$= 2\Delta_f H_m^\theta(SrO) + \Delta_f H_m^\theta(Si) - 2\Delta_f H_m^\theta(Sr) - \Delta_f H_m^\theta(SiO_2)$$

(5.1)

$$\Delta_r S_m^\theta(298.15K) = \sum_B v_B S_B^\theta = 2S_m^\theta(SrO) + S_m^\theta(Si) - 2S_m^\theta(Sr) - S_m^\theta(SiO_2)$$

(5.2)

$$\Delta_r G_m^\theta(298.15K) = \Delta_r H_m^\theta(298.15K) - T\Delta_r S_m^\theta(298.15K)$$

(5.3)

Substitute the corresponding data shown in Table A.1 to get

$$\Delta_r H_m^\theta(298.15K) = 112.152 kJ \cdot mol^{-1}$$

$$\Delta_r S_m^\theta(298.15K) = 29.062 \ J \cdot mol^{-1} \cdot K^{-1}$$

$$\Delta_r G_m^\theta(298.15K) = 103.48716 \ kJ \cdot mol^{-1}$$

At the experimental temperature, for each system, we may write

$$d\Delta_r H_m^\theta = \Delta_r C_{p,m} dT \tag{5.4}$$

$$\Delta_r C_{p,m} = \Delta a + \Delta bT + \Delta cT^2 \tag{5.5}$$

Substitute Eq. [5.5] to Eq. [5.4] and do the integral, we have

$$\Delta_r H_m^\theta = \Delta_r H_{mo}^\theta + \Delta aT + \frac{\Delta b}{2} T^2 + \frac{\Delta c}{3} T^3 \tag{5.6}$$

for

$$\Delta a = 2a(SrO) + a(Si) - 2a(Sr) - a(SiO_2)$$

$$\Delta b = 2b(SrO) + b(Si) - 2b(Sr) - b(SiO_2)$$

$$\Delta c = 2c(SrO) + c(Si) - 2c(Sr) - c(SiO_2)$$

Substitute the corresponding data shown in Table A.2 to get Table A.3

Table A.3 Δa, Δb and Δc at different temperature range.

Temperature	298.15～543K	543～1385K
$\Delta a/(J \cdot mol^{-1} \cdot K^{-1})$	1.678	-4.232
$\Delta b/(J \cdot mol^{-1} \cdot K^{-2})$	-6.287	0.79
$\Delta c/(J \cdot mol^{-1} \cdot K^{-3})$	0.046	6.969

Substitute T= 298.15 K, $\Delta_r H_m^\theta(298.15K) = 112.152 kJ \cdot mol^{-1}$ to Eq. [5.6], we

get

$$\Delta_r H^{\theta}_{mo}(298.15 - 543K) = -15.300 kJ \cdot mol^{-1}$$

Therefore, Eq. [5.6] can be given by

$$\Delta_r H^{\theta}_m(298.15 - 543K) = -15300 + 1.678T - 3.1435T^2 + 0.01533T^3$$

Hence, with the similar method,

$$\Delta_r H^{\theta}_m(543K) = 1513.132 kJ \cdot mol^{-1}$$

and $\quad \Delta_r H^{\theta}_{mo}(543 - 1385K) = -3.7052033 \times 10^5 J \cdot mol^{-1}$

Therefore, $\quad \Delta_r H^{\theta}_m(543 - 1385K) = -370520 - 4.232T + 0.395T^2 + 2.323T^3$

Therefore, $\Delta_r H^{\theta}_m$ as function of temperature can be written as the following

$$\Delta_r H^{\theta}_m(T) = \begin{cases} -15300 + 1.678T - 3.1435T^2 + 0.01533T^3 & (298.15 - 543K) \\ \\ -3.7052033 \times 10^5 - 4.232T + 0.395T^2 + 2.323T^3 & (543 - 1385K) \end{cases} \quad (5.7)$$

Substitute Eq. [5.5] to Van't Hoff Equation,

$$d\ln K^{\theta} / dT = \Delta_r H^{\theta}_m /(RT^2) \quad (5.8)$$

where K^{θ} is equilibruium constant. Integrating Eq. [5.7], we have

$$\ln K^{\theta} = -\frac{\Delta_r H^{\theta}_{mo}}{RT} + \frac{\Delta a}{R} \ln\left(\frac{T}{K}\right) + \frac{\Delta b}{2R} T + \frac{\Delta c}{6R} T^2 + I$$

Hence,

$$\Delta_r G_m^\theta = \Delta_r H_{mo}^\theta - \Delta a T \ln\left(\frac{T}{K}\right) - \frac{\Delta b}{2} T^2 - \frac{\Delta c}{6} T^3 - IRT \qquad (5.9)$$

Substitute the corresponding data to Eq. [5.8], we have

$$I(298.15 - 543K) = -18.31215 J \cdot mol^{-1}$$

Therefore, Gibbs free energy of formation ranging from 298.15 K to 543 K

$$\Delta_r G_m^\theta (298.15 - 543K) = -15300 - 1.678 T \ln\left(\frac{T}{K}\right) - \frac{-6.287}{2} T^2 - \frac{0.046}{6} T^3 + 152.15637 T$$

$$(5.10)$$

Substitute T = 543 K to Eq. [5.9], we have

$$\Delta_r G_m^\theta (543K) = -239.0152 kJ \cdot mol^{-1} \qquad (5.11)$$

and $\quad \Delta_r H_{mo}^\theta (543 - 1385K) = -3.7052033 \times 10^5 kJ \cdot mol^{-1} \qquad (5.12)$

$$I(543 - 1385K) = -123227.21 J \cdot mol^{-1} \qquad (5.13)$$

Substitute Eq. [5.10], [5.11], [5.12] to Eq. [5.8], we get

$$\Delta_r G_m^\theta (543 - 1385K) = -60088576 + 4.232 T \ln\left(\frac{T}{K}\right) - \frac{0.79}{2} T^2 - \frac{6.969}{6} T^3 - 54468.131 T$$

$$(5.14)$$

Hence, Gibbs free energy of formation at the whole temperature range

$$-15300 - 1.678\text{Tln}\left(\frac{T}{K}\right) + 3.1435T^2 - 0.0077T^3 + 152.318T$$

$$(298.15 - 543K)$$

$$\Delta_r G_m^\theta(T) = \begin{cases} & (5.15) \end{cases}$$

$$-3.7052033 \times 10^8 + 4.232\text{Tln}\left(\frac{T}{K}\right) - 0.395T^2 - 1.1615T^3$$

$$+1024572.6T \quad (543 - 1385K)$$

Differentiating Gibbs free energy of formation, we have

$$d\Delta_r G_m^\theta / dT = -\Delta a(1 + \ln(T)) - \Delta bT - \frac{\Delta c}{2}T^2 - IR \tag{5.16}$$

Hence,

$$4.232(1 + \ln(T)) - 0.79T - 3.4845T^2 + 1024572.6$$

$$(543 - 1385K)$$

$$d\Delta_r G_m^\theta / dT = \begin{cases} & (5.17) \end{cases}$$

$$-1.678(1 + \ln(T)) + 6.287T - 0.023T^2 + 152.318$$

$$(298.15 - 543K)$$

According to Eq. [5.7], [5.15], [5.17], Table 5.5 lists the enthalpy of formation, Gibbs free energy of formation, differentiating Gibbs free energy of formation under different temperature can be calculated. We have Table A.4.

As shown in Table A.4, at intersection point T = 543 K, the thermochemical parameters are quite close within 5% error which is acceptable. Moreover, Gibbs free energy of formation at room temperature is greater than zero, which means the reaction $SiO_2(s) + 2Sr(g) \rightarrow Si(s) + 2SrO(g)$ can not occur at this temperature.

Table A.4 Enthalpy of formation, Gibbs free energy of formation, differentiating Gibbs free energy of formation under different temperature

$\Delta_r H_m^\theta(T)$ J/mol	T(K)	$\Delta_r G_m^\theta(T)$ J/mol	$d\Delta_r G_m^\theta / dT$
1.12E+05	2.98E+02	1.03E+05	-1.50E+01
1.12E+05	2.98E+02	1.03E+05	-2.79E+01
1.16E+05	3.00E+02	1.02E+05	-4.28E+01
4.64E+05	4.00E+02	5.17E+04	-1.02E+03
1.12E+06	5.00E+02	-1.21E+05	-2.47E+03
2.17E+06	6.00E+02	-4.62E+05	-4.37E+03
1.51E+06	*5.43E+02*	*-2.44E+05*	*-3.23E+03*
1.51E+06	*5.43E+02*	*-2.39E+05*	*-3.23E+03*
1.31E+08	6.00E+02	-6.79E+06	-2.30E+05
4.26E+08	7.00E+02	-5.19E+07	-6.83E+05
8.19E+08	8.00E+02	-1.46E+08	-1.21E+06
1.32E+09	9.00E+02	-2.95E+08	-1.80E+06
1.95E+09	1.00E+03	-5.08E+08	-2.46E+06

On side of enthalpy of formation, this reaction is an endothermic reaction due to the positive value of enthalpy of formation. For endothermic reaction with Gibbs free energy of formation larger than zero at room temperature, with the increasing of temperature, Gibbs free energy of formation may be less than zero and lead to the possibility of this reaction from the view of thermodynamics. From the table A.4, we

find that this reaction will be more sensitive to temperature due to the fact that the values of enthalpy of formation increase with the temperature. According to Eq.[5.15], Gibbs free energy of formation will be zero at 470 K. Below 470 K, the Gibbs free energy of formation will be negative leading to the occurrence of reaction.

Based on the mechanism of chemical equilibrium, increasing the temperature will speed up this reaction. 470 K only means the starting point of this reaction. In terms of the reaction rate, too slow reaction rate will lead to the situation that the formation of SiO_2 is greater than the decomposition, which will make it impossible to obtain a clean Si surface without an interfacial amorphous Si oxide layer. In our experiment, 650 °C is finally determined to be the temperature at which SiO_2 can be completely removed. Further increasing the temperature will result in the opposite situation. Above 650 °C, The evaporation pressure of Si will larger than SiO_2 under ultrahigh vacuum. From the view of thermodynamics, this reaction will shift to converse direction, inducing the formation of SiO_2.

Reference

1)   A. F. Devonshire, Adv. Phys. 3, 85 (1954).

2)   A. Handi, and R. Thomas, Ferroelectrics 59, 221 (1984).

3)   A. K. Tagantsev, N. A. Pertsev, and A. G. Zembilgotov, Phys. Rev. Lett. 80,1988 (1995).

4)   A. P. Levanyuk, and A. S. Sigov, Defects and structural phase transitions, Gordon and Breach Science Publishers New York, (1988).

5)   B. D. Silverman, Phys. Rev. 125, 1921 (1962).

6)   B. H. Park, Y. Gim, Y. Fan, Q. X. Jia, and P. Lu, Appl. Phys. Lett. 77, 2587 (2000).

7)   B. K. Moon, H. Ishiwara, Jpn. J. Appl. Phys. 30, 5911 (1991).

8)   B. K. Moon, H. Ishiwara, Jpn. J. Appl. Phys. 33 (Pt. 1), 1472 (1994).

9)   B. Riehl, G. Subramanyam, R. Biggers et al, Integer. Ferro. 55, 825 (2003).

10)   B. Rong, J. N. Burghartz, L. K. Nanver, B. Rejaei, and M. van Zwan, IEEE Elec. Device L. 25, 176 (2004).

11)   B. T. Lee and C. S. Hwang, Appl. Phys. Lett. 77, 124 (2000).

12)   C. A. Randall, N. Kim, J. P. Kusera, W. Cao, and T. R. Shrout, J. Am. ceram.

Soc. 81, 677 (1998).

13) C. Buchal, L. Beckers, A. Eckau, J. Schubert, and W. Zander, Materials Science and Engineering B 56, 234 (1998).

14) C. H. Ahn, K. M. Rabe, and J. M. Triscone, Science 303, 488 (2004).

15) C. H. Mueller and F. A. Miranda, Ferroelectric and Acoustic Devices, Eds D. Taylor, and M. Francombe, Academic Press, (2000).

16) C. M. Carlson. P. A. Parilla, T. V. Rivkin, J. D. Perkins, and D. S. Ginley, Appl. Phys. Lett. 76, 3249 (2000).

17) C. T. Black and J. J. Welser, IEEE Trans. Electron Devices 46, 776 (1999).

18) C. Y. Hu, D. Kencke, S. Banerjee, B. Bandyopadhyay, E. Ibok, and S. Garg, Appl. Phys. Lett. 66, 1638 (1995).

19) C. Zhou, and D. M. Newns, J. Appl. Phys. 82, 3081 (1997).

20) C.Y. Hu, D. Kencke, S. Banerjee, B. Bandyopadhyay, E. Ibok, and S. Garg, Appl. Phys. Lett. 66, 1638 (1995).

21) D. D. Fong, G. B. Stephenson and S. K. Streiffer, Science 304, 1650 (2004).

22) D. R. Tilley and B. Zeks, Solid State Commun. 49, 823 (1984).

23) D. Roy and S. B. Krupanidhi, Appl. Phys. Lett. 62, 1056 (1993).

24) D. Y. Wang, Y. Wang, X. Y. Zhou, H. L. W. Chan, and C. L. Choy, Appl.

Phys. Lett. 86, 2904 (2005).

25) E. D. Specht, H. M. Christen, D. P. Norton, and L. A. Boatner, Phys. Rev. Lett. 80, 4317 (1998).

26) F. De Flaviis, D. Chang, N. G. Alexopoulos, and O. M. Stafsudd, 1996 IEEE MTT-S International Microwave Symposium Digest 1, 99 (1996).

27) F. Jona, G. Shirane, Ferrolectric crystals. Pergamon Press. Oxford, (1962).

28) F. S. Yen, H. I. Hsiang, and Y. H. Chang, Jpn. J. Appl. Phys. 34, 6149 (1995).

29) F. Sanchez, M. Varela, X. Queralt, R. Aguiar, and J. L. Morenza, Appl. Phys. Lett. 61, 2228 (1992).

30) F. Sanchez, R. Aguiar, V. Trtik, C. Guerrero, C. Ferrater, and M. Varela, J. Mater. Res. 13, 1422 (1998).

31) G. A. Rossetti Jr., L. E. Cross, and K. Kushida, Appl. Phys. Lett. 59, 2524 (1991).

32) G. M. Barrow, Tables of Chemical Thermodynamic properties published in Journal of Physical and Chemical Reference Data, 11, Suppl. 2, Physical Chemistry, 5th ed., McGraw-Hill, New York, (1988).

33) G. Subramanyam, F. Ahamed, R. Biggers, and R. Neidhard, Frequenz Journal of RF-Engineering and Telecommunications 59, 37 (2005).

34) G. Y. Yang, J. M. Finder, J. Wang, J. Mater. Res. 17, 204 (2002).

35) H. J. Gao, C. L. Chen, B. Rafferty, S. J. Pennycook, G. P. Luo, and C. W. Chu, Appl. Phys. Lett. 75, 2542 (1999).

36) H. Landolt and R. Bornstein, Numerical data and functional relationships in science and technology. New series, Group III, Crystal and solid state physics 16, Revised, updated and extended edition of volumes III/3 and III/9, Ferroelectrics and related substances: A, Oxides. Springer-Verlag, New York (1981).

37) H. Landolt, Landolt-Börnstein, Ferroelectrics and Related Substances, New Series, Group III, 36, Springer-Verlag, Berlin, (2002).

38) H. Mori, H. Ishiwara, Jpn. J. Appl. Phys. 30, L1415 (1991).

39) H. S. Kim, I. D. Kim, K. B. Kim, et al. J. Electro. Ceramic. 17, 421 (2006)

40) H. Yoon, J. K. Abraham, and V. K. Varadan, Microw. Opt Techn. Let. 40, 20 (2004).

41) P. Batra, P. Wupfel, and B. D. Silverman, Phys. Rev. B 8, 3257 (1973).

42) Barskii, O. G. Vendik, A. D. Smirnov, and G. S. Khizha, Sov. Phys. Tech. Phys. 34, 1065 (1990).

43) J. A. Thornton, D. W. Hoffman. Phys. Rev. B 171, 5 (1989).

44) J. C. Slater, Phys. Rev. 78, 784 (1950).

45) J. F. Nye, Physical properties of crystals: their representation by tensors and matrices, Oxford University Press London (1957).

46) J. H. Chen, C. L. Lia, K. Urban and C. L. Chen, Appl. Phys. Lett. 81, 1291 (2002).

47) J. H. Haeni, P. Irvin, W. Chang et al, Nature 430, 758 (2004).

48) J. H. Haeni, P. Irvin, W. Chang, R. Uecker, P. Reiche, Y. L. Li, S. Choudhury, W. Tian, M. E. Hawley, B. Craigo, A. K. Tagantsev, X. Q. Pan, S. K. Streiffer, L. Q. Chen, S. W. Kirchoefer, J. Levy, and D. G. Schlom, Nature 430, 758 (2005).

49) J. Im, O. Auciello, P. K. Baumann, S. K. Streiffer, D. Y. Kaufman, and A. R. Krauss, Appl. Phys. Lett. 76, 625 (2000).

50) J. Lettieri, J. H. Haeni, and D. G. Schlom, J. Vac. Sci. Technol. A 20, 1332 (2002).

51) J. Lettieri, J. H. Haeni, D. G. Schlom, J. Vac. Sci. Technol., A, Vac. Surf. Films A 20, 1332 (2002).

52) J. Robertson, J. Vacuum Sci. Tech. B 18, 1785 (2000).

53) J. X. Liao, C. R. Yang, J. H. Zhang, et al. Appl. Surf. Sci. 252, 7407 (2006).

54) J. Zhang, H. Tanaka and T. Kawai, Appl. Phys. Lett. 80, 4370 (2002).

55) K. B. Kim, T. S. Yun, J. C. Lee, et al. Micro. Opt. Techni. Let. 49, 2144

(2007).

56)   K. Binder, Ferroelectrics 73, 145 (1987).

57)   K. Eisenbeiser, J. M. Finder, Z. Yu, Appl. Phys. Lett. 76, 1324 (2000).

58)   K. Ishikawa, K. Yoshikawa, and N. Okada, Phys. Rev. B 37, 5852 (1988).

59)   K. J. Choi, M. Biegalski, Y. L. Li et al, Science 306, 1005 (2004).

60)   K. J. Choi, M. Biegalski, Y. L. Li, A. Sharan, J. Schubert, R. Uecker, P. Reiche, Y. B. Chen, X. Q. Pan, V. Gopalan, L. Q. Chen, D. G. Schlom, and C. B. Eom, Science 306, 1005 (2004).

61)   K. M. Johnson, J. Appl. Phys. 33, 2826 (1962).

62)   K. Natori, D. Otani, and N. Sano, Appl. Phys. Lett. 73, 632 (1998).

63)   Kim, J. Pak, Nam K, et al. J. Electro. Ceramic. 16, 495 (2006).

64)   M. Terman, Solid-State Electron. 5, 285 (1962).

65)   Sengupta and S. Sengupta, Material Research Innovations 2, 278 (1999).

66)   L. Vegard, Z. Physik. 5, 17 (1921).

67)   L. Zhang, W. L.Zhong, Y. G. Wang, and P. L. Zhang Appl. Phys. Lett.104, 263 (1997).

68)   E. Lines and A. M. Glass, Principles and applications of ferroelectrics and

related materials, Oxford University Press. Oxford, (1977).

69) M. E. Lines, and A. M. Glass, Principles and applications of ferroelectrics and related materials. Oxford University Press. Oxford, (1977).

70) M. F. Hsu, L. J. Wu, J. M. Wu, Y. H. Shiu and K. F. Lin, Electrochem. Solid-State Lett. 9, A193 (2006).

71) M. J. Huan, E. Furman, S. J. Jang, H. A. Mckinstry and L. E. Cross. J. Appl. Phys. 62.3331 (1987).

72) M. N. K. Bhuiyan, A. Matsuda, T. Yasumura, Appl. Phys. Lett. 87, 262905 (2005).

73) M. N. K. Bhuiyan, H. Kimura, T. Tambo, and C. Tatsuyama, Appl. Surf. Sci. 249, 419 (2005).

74) M. N. K. Bhuiyan, H. Kimura, T. Tambo, Jpn. J. Appl. Phys. Part I 44, 677 (2005).

75) M. Suzuki, and T. Ami, Mater. Sci. Eng. B41, 166 (1996).

76) M.W. Chu, I. Szafraniak, R. Scholz et al, Nat. Mater. 3, 87 (2004).

77) A. Pertsev, A. G. Zembilgotov, and A. K. Tagantsev, Phys. Rev. Lett. 80, 1988 (1998).

78) N. A. Pertsev, A. G. Zembilgotov, and A. K. Tagantsev, Phys. Rev. Lett. 80, 1988 (1998).

79) N. Navi, H. Kim, J. S. Horwitz, H. D. Wu, and S. B. Qadri, Appl. Phys. A: Mater. Sci. Process. 76, 841 (2003).

80) N. Sai, B. Meyer, and D. Vanderbilt, Phys. Rev. Lett. 84, 5636 (2000).

81) N. W. Schubring, J. V. Mantese, A. L. Micheli, A. B. Catalan, and R. Z. Lopez, Phys. Rev. Lett. 68, 1778 (1992).

82) N. Yanase, K. Abe, N. Fukushima, and T. Kawakubo, Jpn. J. Appl. Phys. 38, 5305 (1999).

83) G. Vendik, and L. T. Ter-Martirosyan, J. Appl. Phys. 87. 1435 (2000).

84) G. Vendik, and S. P. Zubko, J. Appl. Phys. 82, 4475 (1997).

85) G. Vendik, S. P. Zubko and T. T. Ter-Martirosayn, Appl. Phys. Lett. 73, 37 (1998).

86) G. Vendik, Sov. Phys. Solid State 14, 849 (1972).

87) Nakagawara, M. Kobayashi, Y. Yoshino, Y. Katayama, H. Tabata, and T. Kawai, J. Appl. Phys. 78, 7226 (1995).

88) W. Forsbergh, Phys. Rev. 93, 686 (1954).

89) A. McKee, F. J. Walker, and M. F. Chisholm, Phys. Rev. Lett. 81, 3014 (1998).

90) A. McKee, F. J. Walker, and M. F. Chisholm, Science 293, 468 (2001).

91) A. McKee, F. J. Walker, J. R. Conner, E. D. Specht, D. E. Zelmon, Appl. Phys. Lett. 59 782. (1991).

92) R. A. McKee, F. J. Walker, J.R. Conner, R. Raj, Appl. Phys. Lett. 63, 2818 (1993).

93) R. A. McKee, F. J. Walker, M. F. Chisholm, Phys. Rev. Lett. 81, 3014 (1998).

94) R. Backmann, and K. Barner, Solid State Commum. 68, 865 (1988).

95) R. Blinc and Z. Zeks, Soft Modes in Ferroelectrics and Antiferroelectrics Amsterdam, North-Holland Pub. Co. New York, American Elsevier, (1974).

96) R. C. Cammarata, K. Sieradzki, and F. Spaepen, J. Appl. Phys. 87.1227 (2000).

97) R. E. Cohen, and H. Krakauer, Phys. Rev. B 42, 6416 (1990).

98) R. E. Cohen, Nature 358, 136 (1992).

99) R. Igreji, C. J. Dias, Sensors and Actuators A 112, 291 (2004).

100) R. Kretschmer, K. Binder, Phys. Rev. B 20, 1065 (1979).

101) R. Ramesh, A. Inam, W. K. Chan, B. Wilkens, K. Myers, K. Remschnig, D. L. Hart, and J. M. Tarascon, Science 252, 955 (1991).

102) R. Ramesh, W. K. Chan, B. Wilkens, H. Gilchrist, T. Sands, J. M. Tarascon, V. G. Keramidas, D. K. Fork, J. Lee and A. Safari, Appl. Phys. Lett. 61,

1537 (1992).

103) R. Robert, J. T. Bernhard, W. Frederick, F. A. Miranda, IEEE Transaction on Microwave Theory and Techniques 48, (2000).

104) B. Desu, J. Electrochem. Soc. 140, 2981 (1993).

105) S. B. Desu, V.P. Dudkevich, P. V. Dudkevich, I. N. Zakharchenko and G. L. Kushlyan, Mater. Res. Soc. Symp. Proc. 401, 195 (1996).

106) S. Chattopadhyay, P. Ayyub, V. R. Palkar, and M. Multani, Phys. Rev. B 52, 177 (1995).

107) S. Gevorgian, Int. Journal of RF and Microwave Computer Aided Design 8, 433 (1998).

108) S. K. Streiffer, C. Basceri, C. B. Parker, S. E. Lash, and A. I. Kingon, J. Appl. Phys. 86, 4565 (1999).

109) S. L. Delprat, Durand C, Oh J, et al. Appl. Phys. Lett. 91, 063513 (2007).

110) S. Matsubara, S. Miura, Y. Miyasaka, and N. Shohata, J. Appl. Phys. 66, 5826 (1989).

111) S. S. Gevorgian, E. F. Carlsson, S. Rudner, U. Helmersson, E. L. Kollberg, E. Wikborg and O. G. Vendik, IEEE Trans. Appl. Superconduct. 7, 2458 (1997).

112) S. S. Gevorgian, T. Martinsson, P. L. J. Linner, E. L. Kollberg IEEE Trans.

Microwave Theory Tech. 44, 896 (1996).

113) S. S. Gevorian, T. Martinsson, P. L. J. Linner et al, IEEE Trans. on Micro. Theo. and Tech., 44, 896 (1996)

114) S. T. Lee, N. Fujimura, and T. Ito, Jpn. J. Appl. Phys. 34, 5168(1995).

115) S. W. Liu, J. Weaver, Z. Yuan, W. Donner, C. L. Chen, J. C. Jiang, E. I. Meletis, W. Chang, S. W. Kirchoefer, J. Horwitz, and A. Bhalla, Appl. Phys. Lett. 87, 142905 (2005).

116) J. Zhang, J. Wang, J. Jiang, et al. Thin Solid Films 515, 7721 (2007)

117) T. M. Shaw, Z. Suo, M. Huang, E. Liniger, R. B. Laibowitz, and J. D. Baniecki, Appl. Phys. Lett. 75, 2179 (1999).

118) T. Schimizu, Solid State Commun. 102, 523 (1997).

119) T. Tambo, K. Maeda, A. Shimizu, C. Tatsuyama, J. Appl. Phys. 86, 3213 (1999).

120) T. Tambo, T. Nakamura, K. Maeda, H. Ubba, C. Tatsuyama, Jpn. J. Appl. Phys. 37 (Pt. 1) 4454. (1998).

121) T. Y. Tseng, Ferroelectrics 232, 1 (1999).

122) Nagarajan, S. P. Alpay, C. S. Ganpule, et al, Appl. Phys. Lett. 77, 438 (2000).

123) Chang, C. M. Gilmore, W. -J. Kim, J. M. Pond, S. W. Kirchoefer, S. B.

Qadri, D. B. Chrisey, and J. S. Horwitz, J. Appl. Phys. 87, 3044 (2000).

124) Chang, J. S. Horwitz, A.C. Carter, J. M. Pond, S. W. Kirchoefer, C. M. Gilmore, and D. B. Chrisey, Appl. Phys. Lett. 74, 1033 (1999).

125) W. Chang, J. S. Horwitz, W. J. Kim, J. M. Pond, S. W. Kirchoefer, C. M. Gilmore, S. B. Qadri, and D. B. Chrisey, Integr. Ferroelectr. 24, 257 (1999).

126) W. J. Kim, W. Chang, S. B. Qadri, J. M. Pond, S. W. Kirchoefer, D. B. Chrisey, and J. S. Horwitz, Appl. Phys. Lett. 76, 1185 (2000).

127) W. J. Merz, Phys. Rev. 77. 52 (1950).

128) W. L. Zhong, L. Zhang, Y. G. Wang, and P. L. Zhang Appl. Phys. Lett.104, 263 (1997).

129) W. Y. Park, K. H. Ahn and C. S. Hwang, Appl. Phys. Lett., 83, 4387 (2003).

130) Woo Young Park, Kun Ho Ahn and Cheol Seong Hwang, Appl. Phys. Lett. 83, 4387 (2003).

131) I. Yuzyuk, I. N. Zakharchenko, V. A. Alyoshin, et al. Phys. Solid. State 49, 1759 (2007).

132) J. Li, and K. Tanabe, J. Appl. Phys. 83, 7744 (1998).

133) Y. L. Cheng, Y. Wang, H. L. W. Chan et al, Micro. Eng. 66, 872 (2003).

134) Y. Lin, X. Chen, S. W. Liu, C. L. Chen, J. S. Lee, Y. Li, Q. X. Jia, and A. Bhalla, Appl. Phys. Lett. 86, 142902 (2005).

135) Y. Takagi, E. Sawaguchi, and T. Akioka, J. Phys. Soc. Japan 3, 270 (1948).

136) Y. Wang, C. Ganpule, B. T. Liu, H. Li, K. Mori, B. Hill, M. Wuttig, R. Ramesh, J. Finder, Z. Yu, R. Droopad and K. Eisenbeiser, Appl. Phys. Lett. 80, 97 (2002).

137) Y. Watanabe, Appl. Phys. Lett. 66, 1770 (1995).

138) Yu, J. Ramdani, J.A. Curless, J.M. Finder, C.D. Overgaard, R. Droopad, K.W. Eisenbeiser, J.A. Hallmark, W.J. Ooms, J. Vac. Sci. Technol. B 18,1653 (2000).

139) Z. Yu, R. Droopad, J. Ramdani, J.A. Curless, C.D. Overgaard, J.M. Finder, K.W. Eisenbeiser, J. Wang, J.A. Hallmark, W.J. Ooms, in:H.R. Huff, C.A. Richter, M.L. Martin, G. Lucovsky, T. Hattori, MRS Symp. Proc. 567, Mat. Res. Soc, Pittsburgh PA, 427 (1999).

140) Z. Yu, Y. Liang, C. Overgaard, X.Hu, J. Curless, H. Li, Y. Wei, B. Craigo, D. Jordan, R. Droopad, J. Finder, K. Eisenbeiser, D. Marshall, K. Moore, J. Kulik, and P. Fejes, Thin Solid Films 462, 51 (2004).